Computational Fluid Dynamic Modelling and Optimisation of Internal Twist-Drill Coolant Channel Flow

Adam Stephen Johns

Submitted in accordance with the requirements

for the degree of Doctor of Philosophy

The School of Mechanical Engineering

The University of Leeds

February, 2015

Work Formed from Jointly Authored Publications

The candidate confirms that the work submitted is his own, except where work which has formed part of jointly authored publications has been included. The contribution of the candidate and the other authors to this work has been explicitly indicated below. The candidate confirms that appropriate credit has been given within this thesis where reference has been made to the work of others.

Chapter 4 is an extension of a conference paper which was presented at the ECCOMAS 2014 [Johns et al., 2014]. The candidate conducted all of the computational analysis presented in this paper. The co-authors provided assistance in the preparation of the paper.

This copy has been supplied on the understanding that it is copyright material and that no quotation from the thesis may be published without proper acknowledgement.

Acknowledgements

I would like to use this opportunity to express my sincere gratitude to my supervisors Prof Harvey Thompson, Dr Jon Summers, Dr Eleanor Merson and Dr Rob Hewson for their invaluable encouragement, guidance and support throughout this project. I am very thankful to have been able to work with Professor Harvey Thompson over the last few years and would like to express my deepest appreciation for his insight and enthusiasm.

In addition, a thank you to Dr Gregory de Boer for his assistance and the many fruitful discussions. I would also like to thank Joanne Williams for her patience, kindness and motivation which has helped me succeed. My thanks also goes to Prof Hrvoje Jasak, Dr Dominik Christ and the OpenFOAM community for their continuous support.

Furthermore, I would like to acknowledge Sandvik Coromant for their support throughout this study.

Finally, I would like to thank my friends and colleagues at the University of Leeds, School of Mechanical Engineering who have made the previous three years of work a delight and a privilege to complete.

Abstract

Due to the increasingly challenging thermal loads during drilling applications, coolant application is prevalent in twist-drill machining of metals [Haan et al., 1997]. However, because the cutting zone is not directly observable, there is limited knowledge encompassing the distribution of coolant during the cutting process. This work looks to expand current knowledge of coolant delivery during the cutting process and inform future tool design through the application of numerical methods. This is implemented in the form of two numerical models: a through-tool model, which examines internal coolant flow and the second model which calculates coolant exit flow behaviour.

The through-tool model employs a single phase model and is used to perform a parametric study which identifies the influence of each design parameter on the delivery of coolant. In addition to this metamodelling techniques are adopted to give a global overview of tool parameter effects on coolant delivery and to identify optimal channel configurations.

The coolant exit flow model employs the Volume of Fluid method to simulate the multiphase exit flow of coolant and is validated against experimental data for a simplified case. This model was used to evaluate coolant exit flow for four different coolant channel configurations and study the influence of channel configuration parameters on domain flooding, surface wetting and flow field features.

Contents

List of Figures

Nomenclature

α Volume fraction

$\bar{\nu}$ Kinematic eddy viscosity

$\bar{\phi}$ Average of a general scalar property

$\bar{U}$ Average Velocity

σ Stress tensor

$\mathbf{f}$ Vector of design of experiments response

$\mathbf{g}$ Body force

$\mathbf{q}$ Heat flux

$\mathbf{r}$ Position vector of the rotating frame

$\mathbf{S}$ Outward-pointing face area vector

$\mathbf{U}$ Velocity vector

$\mathbf{x}$ Spatial position vector

δ Curvature ratio

ϵ Dissipation rate of turbulent kinetic energy

η Kolmogorov scale

γ Taylor scale

κ Dimensionless Curvature, mean interface curvature

λ Heat conductivity, weights vector

μ Dynamic viscosity

ν Kinematic viscosity

Ω Angular velocity, mean vorticity

ω Frequency of turbulence

ϕ' Fluctuations of a general scalar property about the mean

ϕ General scalar property

ρ Density

σ Surface tension coefficient

τ Kolmogorov time scale, dimensionless curvature

θ Pitch, closeness of fit parameter

A Channel cross-sectional area

D Helix diameter

d Channel diameter

Dn Dean number

e Total specific energy

e_M Kinetic energy

f_i Response of sample point i

f_{sv} Surface tension forces

f_s Friction factor for curved pipes

Fr Froude number

g Acceleration due to gravity

k Turbulent kinetic energy

L Characteristic length

l Turbulent length scale

L_{int} Integral scale

m Mass flow rate

N,n Number of experiments performed

P Pressure

p Kinematic pressure

R Radius of curvature, helix radius

Re Reynolds number

Re_{crit} Critical Reynolds number

Ro Rossby number

T Characteristic time

T Temperature

U Characteristic velocity

u Specific internal energy

U' Root mean square velocity fluctuations

U_R Velocity relative to the rotating frame of reference

V_M Material volume

W Gram matrix

x Fixed spatial location

Chapter 1

Introduction

1.1 Background

Since the first report of cutting fluids in 1894 by F. Taylor [Avila and Abrao, 2001], the use of coolant during the twist-drill machining of metals has become increasingly used. Internal helical coolant channels are a common method of applying coolant directly to the main source of heat from the drilling process, the cutting edge, without having the delivery of coolant obstructed by chips exiting the cutting zone. The use of this coolant technology increases tool life and performance by lowering the operating temperature of cutting tools, improving average surface finish [Haan et al., 1997] and has also been observed to aid chip evacuation which prevents tool breakage [Braga et al., 2002]. The most common approach of increasing the performance of coolant is to increase the flow rate. However this is problematic considering the increase use of coolant can lead to increased costs and to adverse effects on both the environment and worker health [Braga et al., 2002].

Currently, there is little understanding of the behaviour of coolant within the cutting zone due to experimental limitations arising from the confined geometry between the cutting hole and the rotating tool geometry. Therefore, this thesis focuses on ex-

panding the knowledge encompassing the nature of coolant within twist-drill machining for the purpose of using coolant more efficiently [Abele and Fujara, 2010, Vaz Jr et al., 2007]. By doing so, rather than using the limited approach of replacing coolant supply machinery to achieve greater flow rates, which can be extremely expensive, tool and coolant performance can be improved by directing the coolant to necessary parts of the tool geometry.

1.2   Twist-Drill Machining

Twist-drill machining is a process used to create cylindrical holes through materials and is central to many industries, such as the manufacture of aircraft, cars, railways and ships. A twist drill machine is typically comprised of two core components, the drill and the cutting tool (referred to as a drill bit). The drill is the mechanism responsible for rotating and providing the cutting forces to the drill bit to facilitate the cutting process. The drill bit is responsible for applying the cutting forces to cut the workpiece. The drill bit geometry of interest for this thesis is the fluted drill bit, which is cylindrical in shape and has helical grooves spiralling up the tool. An example of a fluted drill bit is illustrated in Figure 1.1(a). The drill bit in this figure, like all other fluted drills, comprises of three main components, the point, shank and body [Zhang et al., 2008].

The purpose of the drill shank is to connect the drill bit to the drill. The point of the tool, which is located at the opposite end of the tool to the shank, is responsible for the cutting of the material and comprises of the cutting components, such as the cutting edge and chisel edge. Finally, the body of the tool is the part of the tool located between the shank and the point of the tool and consists of several components: the margin, body clearance and flute. The flute gives the fluted drill bit its name and is formed from two or more spiral grooves that traverse the length

(a) Twist-drill

(b) Twist-Drill process Diagram
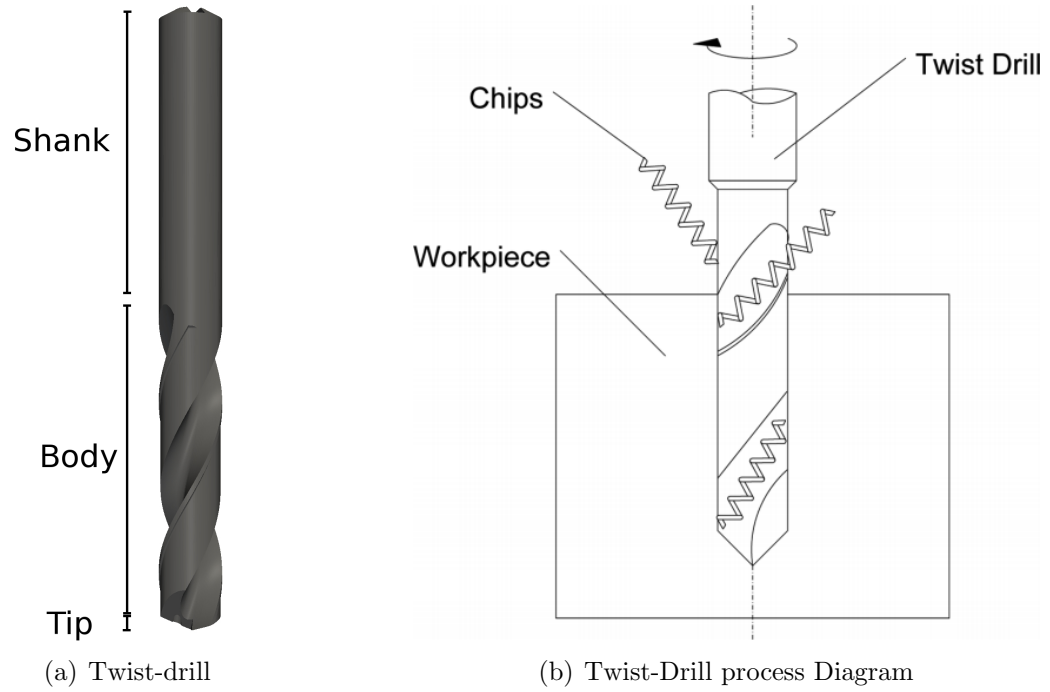
Figure 1.1: Conventional twist drill [Zhang et al., 2008].
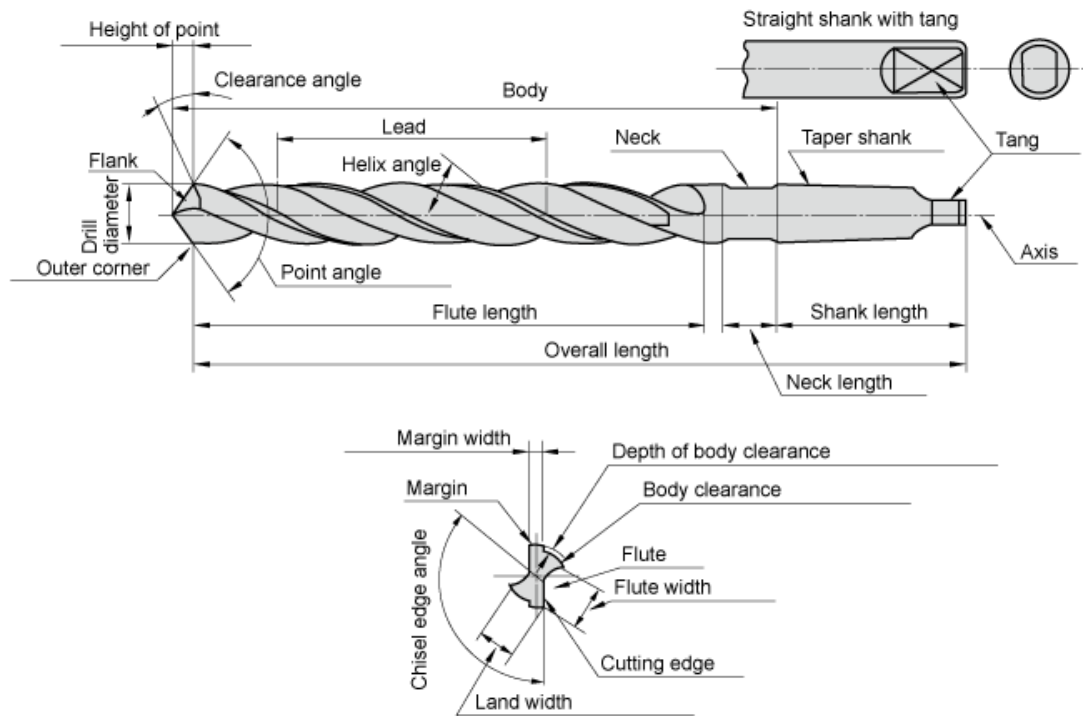
Figure 1.2: Twist drill Nomenclature [Mitsubishi, 2013].

of the tool body. They are responsible for transporting cuttings away from the cutting zone, located at the tip of the tool. Fluted twist drills can be designed very differently depending on the cutting operation; throughout this thesis, twist drills between 40mm and 120mm in total length are considered with tool diameters up to 15mm. For a comprehensive overview of fluted drill components a more detailed diagram is provided in Figure 1.2.

1.3 Use of Coolant in Twist-Drill Machining

The competitive nature of the machining industry creates a constant demand for greater efficiency, increased product quality, greater worker productivity and reduced costs. In twist-drill machining, one of the key issues with achieving greater productivity is the increase in thermal and mechanical loads at the interface between the tool and the chip [Dhar et al., 2006, Jen et al., 2002, Li and Shih, 2007, Shaw, 2005]. A common method of overcoming this increased tool load is through the application of coolant during the machining process. The application of coolant has been found to decrease tool operating temperatures, improve average surface finish [Haan et al., 1997] and aid the evacuation of chips, which prevents tool breakage [Braga et al., 2002, Kalhori, 2001]. The use of coolant is not a recent development within the field and was first reported in 1894 by F. Taylor [Avila and Abrao, 2001]. Since then, the use of coolant in twist-drill machining has increased and three common methods of applying coolant have been developed: conventional cooling (flooding), internal coolant channels and Minimum Quantity Lubrication (MQL).

1.3.1 Flooding

Flooding is the most common method of applying coolant to both the tool and workpiece during the cutting process. This method is illustrated in Figure 1.3 and shows that large quantities of coolant are applied to the cutting area. An advantage

of this approach is that it extends tool life in comparison to dry drilling by removing thermal energy from the cutting zone [Haan et al., 1997]. Furthermore, it does not require expensive specialist implementation, such as tool design which includes through-tool coolant channels or a coolant supply system. Flooding can be applied to most drilling machinery, however it encounters difficulties once the tool is fully engaged with the workpiece inside a cutting hole where there is no direct path to the hottest tool component, the primary cutting edge. Another negative aspect of this method is that it is wasteful in terms of coolant and it has become evident that abundant use of coolant can lead to adverse effects on the immediate environment and the health of machine operators [Braga et al., 2002]. These concerns have led to the development of alternative cooling methods such as internal coolant channels and MQL [Costa et al., 2009].

Figure 1.3: Conventional coolant application [Costa et al., 2009, Coromant, 2013].

1.3.2 Through-Tool Coolant Channels

Internal coolant channels are channels manufactured into the spindle of the tool and are used to supply a high pressure coolant directly from the rear end of the tool to the cutting zone. As these channels are bounded by the geometry of the flute the

channels are helical in shape. This is illustrated in Figure 1.4 where the coolant channels are marked in blue. This delivery system is a response to the problem of delivering coolant directly to the cutting zone without obstruction. The main advantage of using this method is that coolant is supplied directly to the cutting zone and does not have to compete against evacuating chips to reach the hottest parts of the tool located at the tip of the tool. Internal coolant channels are found to further increase tool life by reducing tool temperatures and aiding chip evacuation [Avila and Abrao, 2001] while reducing the amount of abundant coolant. However, this approach does require specialised equipment to provide through-spindle supply of coolant at the rear end of the tool.
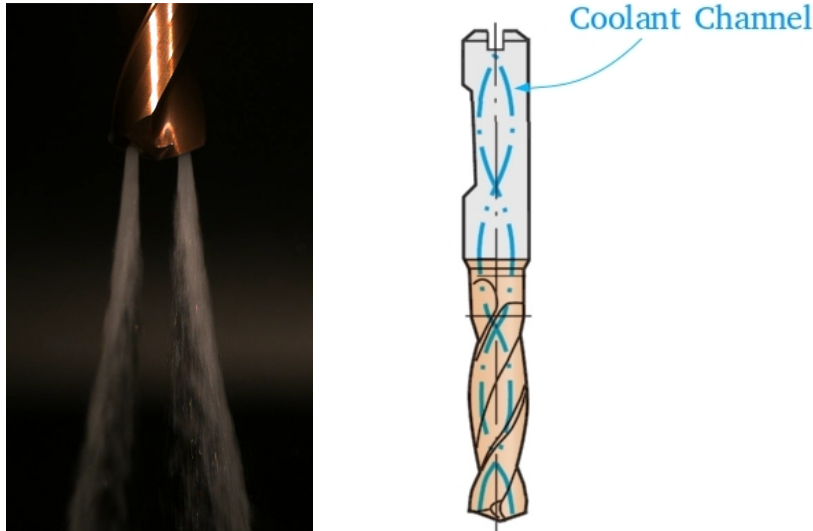
Figure 1.4: Drill design including internal coolant channels [Coromant, 2013].

1.3.3 Minimum Quantity Lubrication

Minimum Quantity Lubrication (MQL) is defined as the spray of a minimum amount of lubricant in a flow of compressed air and is the product of industrial awareness of the negative impact of coolant on the environment and worker health [Braga et al., 2002]. MQL also makes use of through-spindle channels to deliver coolant directly to the cutting area. However, the significant difference between MQL and

through-tool flooding methods, is that MQL provides a typical flow rate of coolant between 50 and 500ml per hour, which is up to 4 orders of magnitude less [Ali et al., 2011, Treurnicht et al., 2010]. MQL was first used approximately 10 years ago, but as a result of design and implementation costs is uncommon in twist-drill machining. These implementation costs emerge from the difficulty in designing an effective system, which can be attributed to the absence of a cutting fluid. The lack of a medium to transport cuttings can lead to catastrophic failures which require enormous effort in designing and implementing an effective system [Dörr and Sahm, 2000, Machado and Diniz, 2000].

1.4   Related Research

Numerous researchers have contributed to the knowledge of tool temperature distribution in twist-drill machining. The majority of these works focus on the generation of heat when cutting metal either with regard to temperature distribution inside the workpiece or inside the tool. Publications which explore thermal effects on the tool can be divided into three categories: Theoretical analyses, numerical approaches using FEM software, and measuring methods.

Theoretical models predict the steady state distribution of heat across the tool cutting edge based on the works of Loewen & Shaw (1954) [Stephenson et al., 1997, Fallenstein and Aurich, 2014]. This research assumes the highest temperatures for the primary cutting edge are located just above the cutting edge corner [Loewen and Shaw, 1954, Wu and Di Han, 2009, Fallenstein and Aurich, 2014].

However, further scientific investigations report opposing heat distributions along the major cutting edge. Depending on the application the highest temperatures can occur at the chisel edge [Bono and Ni, 2006, Bono and Ni, 2002], close to the cutting

edge corner [Bono and Ni, 2001, Wu and Di Han, 2009] or uniform along the major cutting edge [DeVries et al., 1968, Watanabe et al., 1977].

Common experimental methods for measuring the distribution of heat inside the tool tip have been developed by Bono and Ni, who found that the location of maximum temperature occurs near the outer corner of the tool [Bono and Ni, 2006]. Other works, such as the works of Fuh et al. record experimental readings by positioning thermocouples in the workpiece. This work also made use of numerical methods to calculate tool operating temperatures. In this work the numerical model employed three-dimensional FEM methods to predict the temperature distribution within a conventional twist drill based upon the parameters of the machining task [Fuh et al., 1994].

Further work by Wu investigated the predictions of three different finite element codes in respect to heat distribution in dry twist-drill machining. This work calculated the maximum tool temperature and found that the error did not exceed 15% when compared against experimental data captured from a thermocouple positioned in the workpiece [Wu and Di Han, 2009].

Although the use of coolant is common in metal machining, the modelling and simulation of its flow alongside the machining process is a particularly challenging task. The problem is particularly complex due to the diversity of physical phenomena involved, including large elasto-plastic deformation, complicated contact/friction conditions, thermo-hydro-mechanical coupling and chip separation mechanisms. This is made more difficult by the cutting zone not being directly observable which, coupled with the increase in availability of computational resources has led to an increase in investigations using Computational Fluid Dynamics (CFD). Before outlining studies of coolant which employ CFD, this chapter will first give an overview of CFD.

1.4.1 Computational Fluid Dynamics

CFD is described as "the analysis of systems involving fluid flow, heat transfer and associated phenomena such as chemical reactions by a means of computer-based simulation" [Versteeg and Malalasekera, 2007]. CFD is a method which creates discretised forms of partial differential equations for fluid flow problems to solve the governing equations of fluid motion algebraically at a predetermined set of points defined within a computational domain [Versteeg and Malalasekera, 2007]. The use of CFD has become increasingly popular across a wide variety of industrial applications since the 1960s such as:

- Aerospace industry - Aerodynamics of aircraft.

- Power plants - Combustion in combustion engines.

- Turbo-machinery - Fluid behaviour in rotating passages.

- Meteorology - Weather prediction.

The main advantages of using CFD over experimental methods are that it can save time and resources in engineering design and is well suited to problems such as coolant flow in twist-drill machining where regions are inaccessible to experimental measurements. All available CFD codes are structured around the numerical algorithms that can solve fluid flow problems. In order to provide easy access to the solver and to increase user productivity all commercial CFD packages include user interfaces to assist the user in specifying problem parameters and extracting data from results. CFD codes typically contain three main components:

- Pre-processor.

- Solver.

- Post-processor.

Pre-processor

The pre-processor consists of a selection of functions that aid users in the specification of flow parameters and subsequently converting these parameters into a form suitable for the solver [Versteeg and Malalasekera, 2007]. Operations at the pre-processing stage involve:

- Definition of the problem domain geometry

- Grid generation - the sub-division of the domain into a set of smaller, non-overlapping sub-domains.

- Selection of the physical and chemical phenomena to be modelled

- Description of fluid properties and the specification of appropriate boundary conditions at cells which coincide with or touch the boundary of the domain.

The accuracy of a CFD solution is dependent on the number of cells within the grid, which is constructed at the pre-processor stage. In general, the greater number of cells modelling a fluid flow the greater the solution accuracy. Both accuracy and computational cost (in terms of hardware resources and processor time) are dependent on the number of cells which make up the grid. Therefore, the overall accuracy of the model is determined at the pre-processor stage; 50% of the time spent on a CFD project is usually spent defining the problem domain and grid generation in order to gain the best balance of accuracy and performance [Versteeg and Malalasekera, 2007].

Solver

There are three dominant streams of numerical solution techniques: finite difference, finite element and spectral methods. Each of these techniques will be discussed later

in Section 3.3. However, typically the numerical algorithm that makes up the solver consists of the following operations:

- Approximation of unknown flow variables by means of simple functions

- Discretisation by substitution of the approximations into the governing flow equations and subsequent mathematical manipulations.

- Solution of the algebraic equations

Post-processor

The objective of the post-processor is to present the results provided by the solver in a meaningful way to the user. Most modern general purpose CFD packages come equipped with a wide selection of analytical tools for engineers to aid this process, such as:

- Visualisation of geometry, 2D and 3D surface plots, particle tracking, contour plots, animation and vector and stream-line plots.

- Results manipulation

- Exportation functionality (to use in third-party software)

1.4.2   Previous CFD Modelling of Coolant Flow

The use of CFD in evaluating the application of coolant for conventional through-tool coolant has only recently been applied to this area and as a result there are a limited number of publications focused on this field. This section will outline the current work performed in the area.

CFD has been used in the optimisation of the flow conditions inside coolant channels located in the axial slot for MQL applications [Weinert and Loichinger, 2001, Hänle

and Schwenck, 2005]. Other studies have used CFD to numerically predict the erosion in drilling tools caused by cutting fluids [Arefi et al., 2005]. This model dynamically modified the computational geometry model depending on flow conditions and was used to select tool designs which reduce tool erosion.

A recent study has been published which examines the feasibility and accuracy of CFD in the prediction of cutting tool temperature when applying coolant [Chowdhury et al., 2014] This study modelled the temperature at tool tip for a simplified case of a non-rotating cutting tool and found that even though the CFD model employed over predicted the temperature located at the tool interface, it was an effective method of determining the best cutting parameters.

Another recent study by Fallenstein & Aurich employed a single-phase formulation to investigate the thermal conditions in cemented carbide twist drills for 6 different coolant channel exit positions at 4 different volumetric flow rates. This research examined the influence of channel position and flow rate on the removal of heat from the tool and draws from the work of Loewen and Shaw to define the steady state temperature distribution across the tool cutting edge. This study demonstrated that both flow rate and exit positioning of the coolant channel significantly influences the amount of heat removed and that the circumferential positioning of the channel exit position is more influential than the channels radial positioning component [Fallenstein and Aurich, 2014].

Currently the systematic study of the coolant flow field, through-tool flow of coolant, coolant channel exit position and cutting geometry has not been undertaken. However, as explained in Section 1.3.2, the coolant channels are bounded by the spiralled flute of the tool and therefore form a helix. Helical channels are used across a range of different engineering applications and there is a significant amount of relevant

research available which surround the through-tool flow of coolant, this will be discussed next.

1.4.3 The Nature of Helical Channel Flow

The motion of fluid through helical geometries is relevant to a wide range of industrial applications, such as heat exchangers within mechanical or chemical engineering processes as well as through-tool coolant channels. When fluid flows through a helical channel, the generic secondary flow structure adopts the form of two recirculating cell structures, illustrated in Figure 1.5, which is of significant scientific interest because the increased mixing greatly increases the transfer of heat across the fluid-channel interface [Ishigaki, 1996].
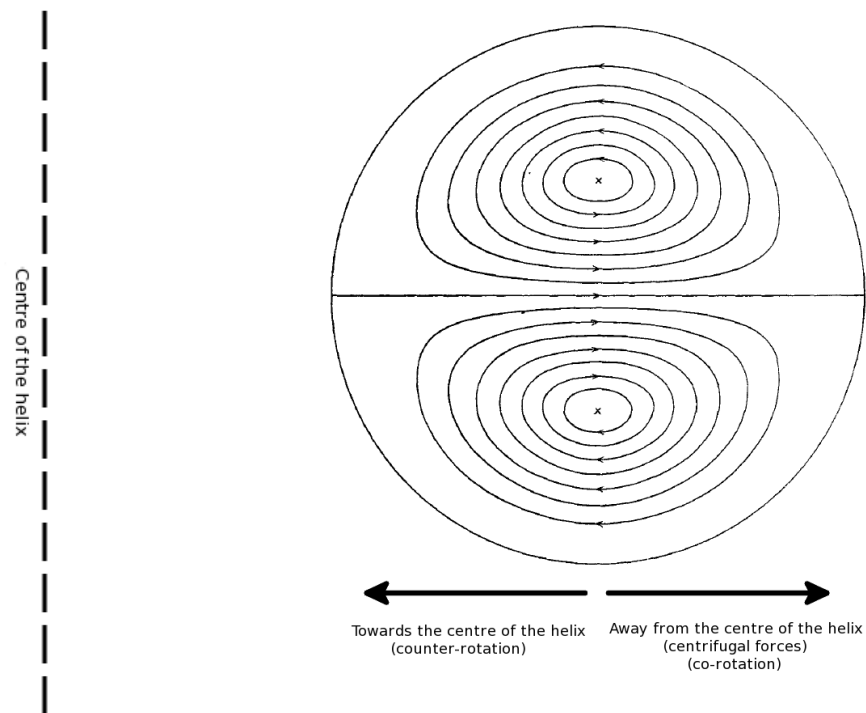
Figure 1.5: Generic secondary flow structure of a curved pipe [Dean, 1927].

Secondary flows are flow structures created by differences in axial motion between fluid particles located in the central and boundary regions of the fluid domain.

When fluid flows through a helical channel which is rotating about the coil axis at a constant angular velocity, two secondary flow forces operate perpendicular to the primary axial flow. The first being centrifugal forces generated by the curvature of the helical geometry and the second being Coriolis forces induced by the rotation of the pipe [Ishigaki, 1996].

The centrifugal forces are generated by the curvature of the geometry and the inertia of the fluid as the fluid's trajectory is continually redirected [Chen and Zhang, 2003]. These forces act perpendicularly to the direction of axial flow, away from the helix central axis. Coriolis forces are the forces generated by the angular motion of the geometry. These forces also operate perpendicular to the direction of axial flow, but their direction is determined by the direction of rotation. When rotating about the central helix axis in the same direction as the axial flow (co-rotation), the direction of the Coriolis forces act away from the central axis of the helix. In the case of co-rotation the secondary flow profile can be seen to remain qualitatively the same as that observed in a stationary helix. This is because Coriolis and centrifugal forces operate in the same direction and behave in an additive sense with each-other [Yamamoto et al., 2000]. However, when the channel is rotating against the axial flow (counter-rotation), Coriolis forces operate against centrifugal forces, pushing the fluid body towards the centre of the coil. Depending on the relative size of these secondary flow forces, complex flow behaviour can be observed as these secondary flow forces compete against each-other [Ishigaki, 1996].

1.4.4   Previous Studies on Helical Channel Flow

The secondary flow pattern described in Figure 1.5 was first observed in experiments conducted by Eustice and Taylor [Eustice, 1911, Eustice, 1910, Taylor, 1929]. These early experiments observed this flow structure by injecting ink into water flowing

through curved channels. At the time, these experiments and analytical methods were used because resources allowing integration of the full Navier Stokes equations numerically were not available.

Empirical research conducted by Ito analysed the frictional pressure drop in curved pipes for both turbulent and laminar flow [Ito, 1959, Ito, 1969]. Ito's earlier paper, obtained the friction factor coefficient correlation for turbulent curved pipe flow:

$$f_c = 1.216Re^{-0.25} + 0.116(\frac{d}{D})^{0.5} \tag{1.1}$$

Where D is the diameter of the helical channel and d is the diameter of the channel. This coefficient was also later shown to be in good agreement with the experimental findings of Srinivasan [Srinivasan et al., 1968] who also studied pressure drop and heat transfer within stationary helical pipe flow and proposed the following friction factor coefficient:

$$f_c = 1.334Re^{-0.2}(\frac{d}{D})^{0.1} \tag{1.2}$$

With the advance of computational resources numerical approaches then became feasible, which allowed the investigation of confined channel flow patterns, such as works by Patankar et. al.. In Patankar's earlier work a finite-difference method was used to accurately predict fluid velocity and heat transfer for developing and fully developed laminar flow in coiled pipes [Patankar et al., 1974, Patankar and Spalding, 1972]. This method was later applied to examine turbulent flow in coiled pipes and employed a k-ϵ turbulence model to examine secondary flow and velocity profiles. The friction factor coefficients calculated showed reasonable agreement with the experimental findings of [Ito, 1959] and [Schlichting and Gersten, 2000].

Bolinder and Sunden visually documented the laminar flow pattern using Laser-Doppler Velocity measurements in a static helical square duct of finite pitch. These

experiments were originally used to verify the two-cell flow structure observed within the numerical results [Jonas Bolinder and Sunden, 1995]. Ujhidy et al. also used Laser-Doppler Velocity measurements to visualise the laminar flow of water through convoluted channels. The secondary flow had good agreement between experimental and numerical results [Ujhidy et al., 2003, Naphon and Wongwises, 2006].
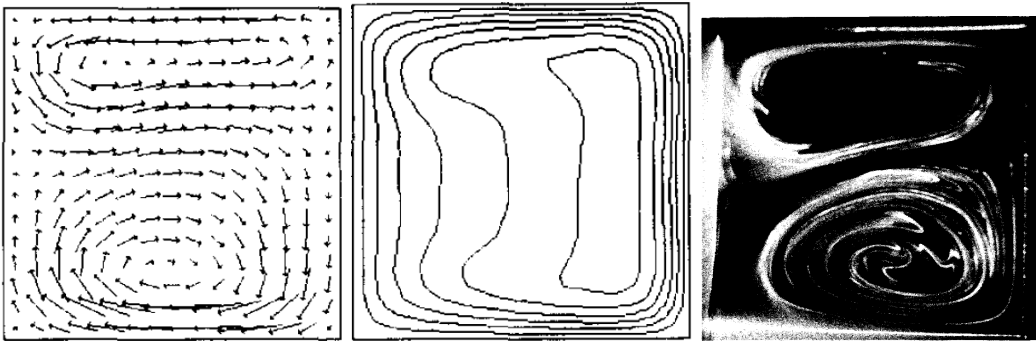
Figure 1.6: Numerical results illustrating the secondary flow structure (Left), (Centre) axial velocity contours and experimental data (Right). In each case the outer wall is located to the right [Jonas Bolinder and Sunden, 1995].

The effects of torsion and curvature on the flow characteristics in curved tubes have also been of interest to numerous researchers. Wang proposed a non-orthogonal helical co-ordinate system which was used to numerically investigate the effects of curvature and torsion on laminar flow through helical pipes. These findings showed that when the Reynolds number was less than 40, non-negligible effects were induced by curvature and torsion. However, when the Reynolds number was 1, a secondary flow consisting of a single recirculating cell was induced by the torsion and the curvature caused an increase in flow rate. This behaviour is significantly different to the standard two recirculating cell structure and decreased flow rate that typically occurs at high Reynolds numbers. Furthermore, it was in disagreement with Germano's (1982) findings. This work proposed an orthogonal coordinate system along a spatial curve to study the effects of torsion in helical channels. This coordinate system was also adopted by a number of later studies focusing on helical

flows [Zhang and Zhang, 2003, Yamamoto et al., 1994, Yamamoto et al., 1994, Yamamoto et al., 1998, Yamamoto et al., 2002, Gammack and Hydon, 2001, Alam et al., 2007, Naphon and Wongwises, 2006, Wang, 1981, Germano, 1982].

Yamamoto et. al. furthered the study of the effects of torsion and curvature on helical channel flow. This work carried out experiments for three different dimensionless curvatures and seven values of torsion and demonstrated that torsion had a destabilising effect on the flow. The results obtained from the experiments were used to validate those obtained from their numerical models [Yamamoto et al., 1998, Yamamoto et al., 1994]. In their later paper, the combined effects of rotation, torsion and curvature were numerically studied for steady-state incompressible flow through helical pipes using Germano's orthogonal coordinate system [Yamamoto et al., 2000, Germano, 1982]. This paper showed that flow through rotating helices is governed by three modified parameters: the Taylor number, Dean number and the torsion parameter. The results showed that counter-rotation greatly affected the total mass flow rate due to Coriolis forces being able to neutralise, or in some cases dominate the centrifugal forces and reverse the secondary flow. For co-rotating cases the Coriolis forces were seen to strengthen the secondary flow as well as reduce the overall mass flow rate. In 2002 Yamamoto et. al. investigated the secondary flow structure and stability of flow in helical pipes with large torsion by using numerical calculations of fluid particle trajectories. The results obtained from the model were in good agreement with the authors' earlier experiments [Yamamoto et al., 2002].

Huttl and Friendrich (2000, 2001) numerically studied the effects of torsion and curvature within coiled channel flows. This work showed that the flow rate through a helical duct was not affected by the torsion of the duct and that curvature had the dominant effect over the flow rate. Although torsion had little effect on the flow rate, it was found to primarily affect the fluctuating kinetic energy and the profile of

the secondary flow. In addition to this, these numerical studies also saw high values of curvature significantly inhibiting turbulence, which was originally documented by both Taylor and White in 1929 [Hüttl and Friedrich, 2000, Hüttl and Friedrich, 2001].

Gammack and Hydon (2001) studied steady and unsteady flows through helices of non-uniform curvature and torsion. This research also used an orthogonal helical coordinate system to obtain analytical and numerical solutions for flows driven by a steady pressure gradient. This work also found that the torsion parameter affects the strength of the secondary flow in steady flows, however for unsteady flows torsion increases the wall shear stress in some regions of the pipe [Gammack and Hydon, 2001, Germano, 1982].

Guo et. al. experimentally studied the frictional pressure drop for single-phase water and steam-water two-phase flow through stationary helical channels. This work found that the single-phase frictional pressure drop for smaller helices was higher than that of a large one. Four different helical inclinations were tested. The inclination of the helical geometry was found to affect the single phase frictional pressure drop by less than 12%. All measured data were also fitted to obtain the friction factor correlation [Guo et al., 2001]:

$$f_c = 2.552 Re^{-0.15} \frac{d}{D}^{0.51} \tag{1.3}$$

1.5   Research Aims and Objectives

Despite being in use for several decades, there is surprisingly little scientific literature detailing precisely how coolant increases the productivity of twist-drills for internal coolant channels. As outlined earlier, this is due to experimental limitations which

prevent direct observation of coolant application during the cutting process. Any invasive measurement will likely obstruct the cuttings and influence the flow as well as risk tool failure. In order to further increase tool performance through the application of coolant a full understanding of the behaviour of coolant delivery is required. In light of experimental challenges, this thesis will apply CFD methods to fill in several gaps in the existing literature and gain a more detailed understanding of the application of coolant during the cutting process to inform future design process. Therefore the following objectives are specified below:

- To understand the fundamental principles of fluid flow and CFD (Computational Fluid Dynamics) so that numerical methods can be applied to numerically investigate coolant distribution during the machining process.

- Experimentally measure coolant flow to identify operating conditions and to inform the numerical model.

- To systematically study the effects of the governing design parameters on the delivery of coolant and construct a metamodel of the numerical model response. This can be used by tool designers to examine numerical model responses without experimental work or time consuming numerical evaluations.

- Build an understanding of available multiphase modelling techniques for the application of coolant exit flow modelling and apply this knowledge in constructing a numerical model to predict coolant exit flow behaviour.

- Numerically evaluate the distribution of coolant exiting the tool geometry to gain insight into how coolant spreads about the cutting zone after exiting the tool. This model will then be used to analyse the exit flow of coolant for a range of different geometry configurations.

This work has been conducted through the use of both experimental and numerical techniques to influence the engineering design and operational conditions of twist-

drills, with the overall aim of increasing coolant performance during the machining process.

1.6   Thesis Outline

This thesis addresses a number of key issues relating to coolant application in twist-drill machining. The governing flow equations are discussed in Chapter 2 and the modelling methodology for through-tool flow is discussed in Chapter 3. Chapter 4 employs the model described in chapters 2 and 3 to analyse the through-tool flow of coolant in a rotating twist-drill. The thesis will then move on to give an overview of the theoretical background of multiphase modelling techniques in Chapter 5 and the numerical approach used to model coolant exit flow. Chapter 6 presents the numerical analysis of coolant exit behaviour. Finally Chapter 7 discusses the implications of the work throughout this thesis and concludes with suggestions for further work.

Chapter 2

Governing Flow Equations

2.1 Introduction

In this chapter the governing equations of continuum mechanics and the appropriate constitutive relations for Newtonian cutting fluids are summarised. This chapter will also include analysis of non-dimensionalised Navier Stokes equations, operating parameters of importance in rotating flows and close with an overview of turbulence modelling methods.

2.2 Governing Equations of Continuum Mechanics

The coolant used in this research is treated as a continuum because the analysis of fluid flow at macroscopic scales ($1\mu m$ and larger), the molecular structure of the matter and molecular motions are much smaller than the length scales of interest. The behaviour of the fluid is described in terms of macroscopic properties, such as velocity, pressure, density and temperature and their space and time derivatives. These can be thought of as averages over a large number of molecules and are represented as continuous functions of space and time. This is achieved by first

introducing the concept of the material derivative, which describes the rate of change of a physical property, ϕ, in time and space [Jasak, 1996]:

$$\frac{d}{dt} \int_{V_M(t)} \rho\phi(\mathbf{x}, t)dV = \frac{\partial}{\partial t} \int_{V_M(t)} \rho\phi dV + \oint_{\partial V_M(t)} d\mathbf{S} \cdot (\rho\phi\mathbf{U}), \tag{2.1}$$

where $\mathbf{U}$ is fluid velocity, ρ is density, x is the position vector and $d\mathbf{S}$ is the outward pointing unit vector normal to $\partial V_M(t)$. The rate of change of ϕ in volume V_M is equal to its unit volume sources, Q_V, and surface sources, Q_S:

$$\frac{\partial}{\partial t} \int_{V_M(t)} \rho\phi dV + \oint_{\partial V_M(t)} d\mathbf{S} \cdot (\rho\phi\mathbf{U}) = \int_{V_M(t)} Q_V(\phi)dV + \oint_{\partial V_M(t)} d\mathbf{S} \cdot Q_S(\phi) \tag{2.2}$$

This is expressed in differential form as:

$$\frac{\partial(\rho\phi)}{\partial t} + \boldsymbol{\nabla} \cdot (\rho\phi\mathbf{U}) = Q_V(\phi) + \boldsymbol{\nabla} \cdot Q_S(\phi) \tag{2.3}$$

We express the governing equations of continuum mechanics in the same form [Aris, 1990]:

Conservation of Mass

$$\frac{\partial\rho}{\partial t} + \boldsymbol{\nabla} \cdot (\rho\mathbf{U}) = 0, \tag{2.4}$$

This equation states that the matter entering the system per unit of time is equal to the mass leaving the system with the result that mass is always conserved. This means that mass cannot be created or destroyed.

Conservation of linear momentum

$$\frac{\partial\rho\mathbf{U}}{\partial t} + \boldsymbol{\nabla} \cdot (\rho\mathbf{U}\mathbf{U}) = \rho\mathbf{g} + \boldsymbol{\nabla} \cdot \sigma, \tag{2.5}$$

Where **g** is a body force (e.g. gravity.) and σ is the stress tensor. The conservation of linear momentum equation states for a closed system where no external forces act upon the continuum ($\mathbf{g} = 0$), the rate of change of total momentum is zero.

Conservation of angular momentum

$$\frac{\partial \rho(\mathbf{x} \times \mathbf{U})}{\partial t} + \boldsymbol{\nabla} \cdot [\rho(\mathbf{x} \times \mathbf{U})\mathbf{U}] = \rho(\mathbf{x} \times \mathbf{g}) + \mathbf{x} \times (\boldsymbol{\nabla} \cdot \sigma). \qquad (2.6)$$

This equation states that when no external torque acts on a closed system of objects, no change in angular momentum can occur. Therefore, the angular momentum before an event involving only internal torque or zero torque is equal to the angular momentum after the event [Landau and Lifshits, 1975].

Conservation of energy

$$\frac{\partial \rho e}{\partial t} + \boldsymbol{\nabla} \cdot (\rho e \mathbf{U}) = \rho \mathbf{g} \cdot \mathbf{U} + \boldsymbol{\nabla} \cdot (\sigma \cdot \mathbf{U}) - \boldsymbol{\nabla} \cdot \mathbf{q} + \rho Q, \qquad (2.7)$$

where **q** is the heat flux and e is the total specific energy. The conservation of energy equation represents the first law of thermodynamics, which states the energy for a closed system can change form, but energy cannot be created of destroyed.

This set of governing equations is valid for any continuum. However, as the number of unknowns is greater than the number of equations, the system is indeterminate. In order to close the system additional constitutive relations are introduced, which vary depending on the properties of the continuous mass being modelled. The coolant considered within this research is approximately $92 - 96\%$ water and the remaining portion consists of an oil with similar properties to water. Consequently, this research treats the continuum as water and therefore as a Newtonian fluid.

2.3 Newtonian Fluids

A Newtonian fluid is a fluid for which the viscous stresses in the flow are linearly proportional to the local strain rate. These are named after Isaac Newton, who first proposed the relation between the rate of shear strain rate and shear stress for such fluids. The strain rate is the rate of change of its deformation over time. In other words viscous forces are linearly related to the rates of local change of fluid velocity.

A fluid is Newtonian if the tensors which describe the viscous stresses and the strain rate are related by a constant viscosity tensor that does not depend on the stress state and velocity of the flow. If the fluid is also isotropic the viscosity tensor reduces to two real coefficients, describing the fluids resistance to continuous shear deformation and continuous compression or expansion respectively.

2.4 Constitutive Relations for Cutting Fluids

The following set of constitutive relations for Newtonian fluids are used to finally close the system of equations.

- The internal energy equation, which defines the internal energy, u, as a function of pressure P and temperature T:

$$u = u(P, T). \tag{2.8}$$

The total energy is calculated as the sum of the kinetic e_M and internal energy

$$e = e_M + u(P, T) = \frac{1}{2}\mathbf{U} \cdot \mathbf{U} + u(P, T). \tag{2.9}$$

- The equation of state, which defines density, ρ as a function of pressure P and

temperature T:

$$\rho = \rho(P, T), \tag{2.10}$$

- Fourier's law of heat conduction:

$$\mathbf{q} = -\lambda \boldsymbol{\nabla} T, \tag{2.11}$$

where λ is the material's conductivity. Fourier's law of heat conduction states that the time rate of heat transfer through a material is proportional to the negative gradient in the temperature and to the area.

- Stress tensor, σ, is described using the generalised form of Newton's law of viscosity:

$$\sigma = -\left(P + \frac{2}{3}\mu\boldsymbol{\nabla} \cdot \mathbf{U}\right)\mathbf{I} + \mu[\boldsymbol{\nabla}\mathbf{U} + (\boldsymbol{\nabla}\mathbf{U})^T], \tag{2.12}$$

where μ is viscosity. These relations, combined with the previously stated governing equations for a continuum, create a closed system of partial differential equations for Newtonian cutting fluids:

- Continuity equation

$$\frac{\partial \rho}{\partial t} + \boldsymbol{\nabla} \cdot (\rho\mathbf{U}) = 0. \tag{2.13}$$

- Navier-Stokes equations, constructed from the conservation of linear momentum and Newton's law of viscosity:

$$\frac{\partial \rho\mathbf{U}}{\partial t} + \boldsymbol{\nabla} \cdot (\rho\mathbf{U}\mathbf{U}) = \rho\mathbf{g} - \boldsymbol{\nabla}\left(P + \frac{2}{3}\mu\boldsymbol{\nabla} \cdot \mathbf{U}\right) + \boldsymbol{\nabla} \cdot [\mu(\boldsymbol{\nabla}\mathbf{U} + (\boldsymbol{\nabla}\mathbf{U})^T)]. \tag{2.14}$$

- Energy equation, defined by the conservation of energy equation, Newton's

law of viscosity and Fourier's law of heat conduction:

$$\frac{\partial \rho e}{\partial t} + \boldsymbol{\nabla} \cdot (\rho e \mathbf{U}) = \rho \mathbf{g} \cdot \mathbf{U} - \boldsymbol{\nabla} \cdot P\mathbf{U} - \boldsymbol{\nabla} \cdot \left(\frac{2}{3} \mu (\boldsymbol{\nabla} \cdot \mathbf{U})\mathbf{U} \right)$$
$$+ \boldsymbol{\nabla} \cdot [\mu(\boldsymbol{\nabla}\mathbf{U} + (\boldsymbol{\nabla}\mathbf{U})^T) \cdot \mathbf{U}] + \boldsymbol{\nabla} \cdot (\lambda \boldsymbol{\nabla} T) + \rho Q.$$

The coefficients for heat conductivity, λ, and viscosity, μ, are also functions of pressure, P, and temperature, T:

$$\lambda = \lambda(P, T), \tag{2.15}$$

$$\mu = \mu(P, T). \tag{2.16}$$

This system of equations can be simplified to model isothermal flow. By assuming $\lambda = \infty$, the system is reduced to the following equations:

$$\frac{\partial \rho}{\partial t} + \boldsymbol{\nabla} \cdot (\rho \mathbf{U}) = 0, \tag{2.17}$$

$$\frac{\partial \rho \mathbf{U}}{\partial t} + \boldsymbol{\nabla} \cdot (\rho \mathbf{U}\mathbf{U}) = \rho \mathbf{g} - \boldsymbol{\nabla} P + \boldsymbol{\nabla} \cdot (\mu \boldsymbol{\nabla} \mathbf{U}), \tag{2.18}$$

We can make additional simplifications to model isothermal and incompressible Newtonian fluids, by assuming $\rho = constant$, and $\lambda = \infty$:

$$\boldsymbol{\nabla} \cdot \mathbf{U} = 0. \tag{2.19}$$

$$\frac{\partial \mathbf{U}}{\partial t} + \boldsymbol{\nabla} \cdot (\mathbf{U}\mathbf{U}) = \mathbf{g} - \boldsymbol{\nabla} p + \boldsymbol{\nabla} \cdot (\nu \boldsymbol{\nabla} \mathbf{U}), \tag{2.20}$$

where p is kinematic pressure and ν is the kinematic viscosity defined as $\nu = \frac{\mu}{\rho}$.

2.5 Dimensional Analysis

Non-dimensionalising the Navier Stokes equations to suggest the relative sizes of various terms and their influence on the flow. To do this any dimensions in the Navier Stokes Equation (2.18) need to be removed [Cimbala and Çengel, 2008].

$$\frac{\partial(\rho\mathbf{U})}{\partial t} + \boldsymbol{\nabla} \cdot (\rho\mathbf{U}\mathbf{U}) = \rho\mathbf{g} - \boldsymbol{\nabla}p + \boldsymbol{\nabla} \cdot (\mu\boldsymbol{\nabla}\mathbf{U})$$

The Navier-Stokes equations above are scaled by introducing a range of characteristic quantities. These are; L, the characteristic length, U, the characteristic velocity, T, the characteristic time $(T = \frac{L}{U})$ and P, the characteristic pressure (ρU^2). The non-dimensional variables are defined using the characteristic quantities as:

$$t^* = \frac{U}{L}t \qquad\qquad\qquad t = Tt^*$$

$$p^* = \frac{p}{\rho U^2} \qquad\qquad\qquad p = \rho U^2 p^*$$

$$\mathbf{U}^* = \frac{\mathbf{U}}{U} \qquad\qquad\qquad \mathbf{U} = U\mathbf{U}^*$$

$$\boldsymbol{\nabla}^* = L\boldsymbol{\nabla} \qquad\qquad\qquad \boldsymbol{\nabla} = \frac{1}{L}\boldsymbol{\nabla}^*$$

$$\mathbf{F}^* = \frac{\mathbf{g}}{g} \qquad\qquad\qquad \mathbf{g} = \mathbf{F}^*g$$

The appropriate terms above are then substituted into the Navier Stokes equations to obtain:

$$\frac{\rho U^2}{L}\frac{\partial\mathbf{U}^*}{\partial t^*} + \frac{\rho U^2}{L}\boldsymbol{\nabla}^*(\mathbf{U}^*\mathbf{U}^*) = -\frac{\rho U^2}{L}\boldsymbol{\nabla}^*p^* + \frac{\mu U}{L^2}\boldsymbol{\nabla}^{*2}\mathbf{U}^* + \rho g\mathbf{F}^* \qquad (2.21)$$

Each term in this equation has primary dimensions $\{m^{-1}L^{-2}t^{-2}\}$. To non-dimensionalise the equation we finally multiply each term by $\frac{L}{(\rho U^2)}$, which has primary dimensions $\{m^{-1}L^{-2}t^{-2}\}$. The dimensions now cancel to obtain:

$$\frac{\partial \mathbf{U}^*}{\partial t^*} + \boldsymbol{\nabla}^* \cdot (\mathbf{U}^* \mathbf{U}^*) = -\boldsymbol{\nabla}^* p^* + \underbrace{\frac{1}{Re}}_{\text{Inverse Reynolds number}} \boldsymbol{\nabla}^{*2} \mathbf{U}^* + \underbrace{\frac{1}{Fr} \mathbf{F}^*}_{\text{Inverse Froude number}} \qquad (2.22)$$

where Re and Fr are the Reynolds and Froude numbers respectively.

Reynolds Number

The Reynolds number is the ratio of inertial forces to viscous forces and is defined as:

$$Re = \frac{\rho U L}{\mu} \qquad (2.23)$$

This dimensionless quantity is typically used to indicate whether the flow is laminar or turbulent. Below a certain critical Reynolds number, the flow is classified as laminar. Laminar flow is characterised by smooth adjacent layers of fluid moving in a parallel and organised fashion. The critical Reynolds number, however, can vary depending on the geometry of interest. For regular straight pipe flow $Re_{crit} \approx 2000$ [Versteeg and Malalasekera, 2007]. Above the critical Reynolds number the flow regime changes greatly as inertia forces begin to dominate viscous forces.
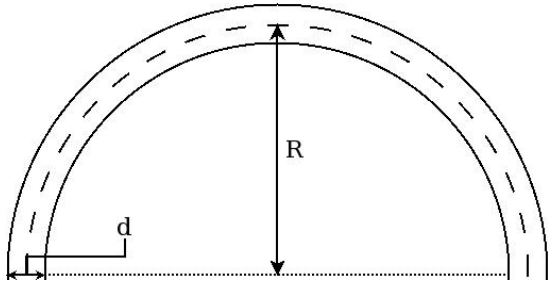
Figure 2.1: Parameters for the ratio of curvature.

As a result, the uniform parallel flow profile of laminar flow is disrupted by seemingly random three-dimensional vorticity and the flow becomes chaotic and unsteady [Tennekes and Lumley, 1972]. This flow regime is known as turbulent flow and will be described in greater detail in Section 2.6. For internal helical coolant channels used within twist-drills, the critical Reynolds number is related to the cur-

vature ratio of the channel. The curvature ratio of the channel is defined as the diameter of the channel divided by the radius of curvature ($\delta = \frac{d}{R}$). This is illustrated in Figure 2.1.

The effect of curvature on turbulence has been experimentally studied by Ito ([Ito, 1959]) who proposed the following critical Reynolds number correlation for curvature ratios in the range of $5 \times 10^{-4} \leq \delta \leq 0.2$ [Ito, 1959]:

$$Re_{crit} = 2000(1 + 13.2\delta^{0.6}) \tag{2.24}$$

The coolant channels of interest for this research have curvature within the range of $0.018 \leq \delta \leq 0.025$. Using this correlation the critical Reynolds number for through-tool coolant flow is within the region of $4448 \leq Re_{crit} \leq 4886$. The Reynolds number of the coolant delivery falls within the range of $40,000 \leq Re \leq 80,000$ depending on the cutting operation, therefore the flow regime is characterised as fully turbulent.

2.5.1 Froude Number

The Froude number is a measure of the ratio of inertia to gravity forces and is defined as:

$$Fr = \frac{U^2}{gL} \tag{2.25}$$

For twist-drills with coolant channels of 1mm in channel diameter the average velocity of coolant exiting the tool ranges between 40 and 80m/s. Therefore the Froude number will be between 400 and 800. This suggests that gravity forces will be dominated by the inertial forces and will not be very significant.

2.5.2 Dimensionless Parameters for Rotating Helical Flow

There are additional dimensionless numbers which are of interest for rotating coiled channel flow. These are the Dean and Rossby numbers.

The Dean Number, Dn

The Dean number is a modified Reynolds number, which accounts for centrifugal forces generated by the continual redirection of the fluid [Dean, 1927]. This dimensionless quantity is defined as:

$$Dn = Re \left(\frac{d}{2R} \right)^{\frac{1}{2}} \tag{2.26}$$

Where d is channel diameter and R the radius of channel curvature. A Dean number of 0 corresponds to Poiseuille flow as there are no centrifugal forces acting on the motion of fluid. As the Dean number increases, symmetry observed in Poiseuille flow breaks down and the position of maximum velocity migrates towards the boundary along the outside of the curve. This migration is illustrated in Figure 2.2. The Dean
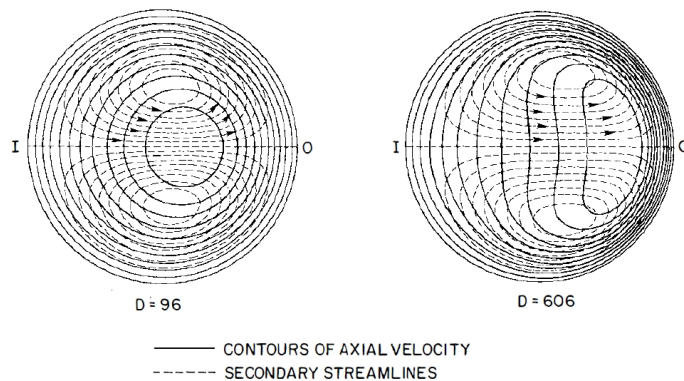
Figure 2.2: Secondary flow streamlines and axial velocity contours for low and intermediate Dean numbers [McConalogue and Srivastava, 1968]. I denotes the inner bend and O the outer bend.

number only accounts for the effects of geometry curvature, not the torsion. This is because the Dean number was originally derived from experiments using toroidally curved pipes of zero pitch [Dean, 1927]. Truesdell & Adler [Truesdell and Adler,

1970] suggested that the resistance formula for toroidally curved pipes is also applicable to helically coiled pipes which was later concluded by Murata et al. [Murata and Miyake, 1981]. Therefore the Dean number will be of significance to the study of internal coolant channels.

If a general tool geometry is considered, where tool lengths are between 40mm and 80mm, hole spacing (helix radius) up to 3.3mm, pitch of up to 50°, channel diameter of 1mm, the average exit velocity is between 40m/s and 80m/s. These tools can rotate up to 10,000 times per minute. The Reynolds number was previously calculated in section 2.5 and falls in the region of 40,000 and 80,000 depending on tool geometry. Here $d = 0.001$, $R = 0.0033$ and the resulting Dean number $Dn = 15570$ when $Re = 40,000$ and $Dn = 31140$ when $Re = 80000$. From the very large Dean number it can be seen that centrifugal forces will have a very large effect on motion of coolant through the coiled internal channels.

The Rossby Number, Ro

The Rossby number is the ratio of inertial forces to Coriolis forces, defined as:

$$Ro = \frac{U}{\Omega R} \tag{2.27}$$

where Ω is the angular velocity, U the average velocity and R the helix radius. This dimensionless quantity is generally used when analysing rotating fluid processes and indicates the importance of Coriolis forces generated by the angular momentum of the system. Cases with $Ro \leq 1$ suggest that rotation has a significant effect on the behaviour of the fluid

For the tool geometries interest, where tool lengths are between 40mm and 80mm, helix radius of up to 3.3mm and pitch of up to 50°, the average exit velocity is

between 40m/s and 80m/s depending on the tool geometry. These tools rotate at up to 10,000 times per minute. The angular velocity is calculated by:

$$\frac{rpm \times (2\pi)}{60} \tag{2.28}$$

The Rossby number therefore resides between 23 and 463. This suggests that
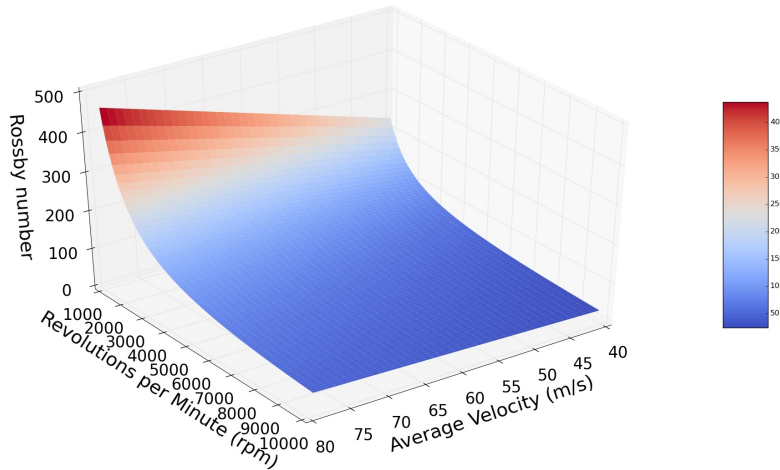
Figure 2.3: Rossby number as a function of average velocity and angular velocity with a constant helix diameter of 0.003m.

rotation will not have a significant influence on the delivery of coolant, which may seem surprising considering the large number of revolutions per minute.

2.5.3 Summary

The calculation and analysis of the Froude and Reynolds numbers strongly suggests the supply of coolant during the drilling process is not significantly influenced by gravity forces and is highly turbulent. From examining both the Rossby and Dean numbers in conjunction it is suggested that centrifugal forces generated by the curvature of the geometry will have the dominant effect on the delivery of coolant to the cutting edge of the tool. The large Rossby number indicates that the effects of rotation will be far less influential on the flow of coolant.

2.6 Turbulent Flow

Having established that coolant flow is turbulent it is important to understand the characteristics of turbulent flow. Although there is no formal definition of turbulence, it can be identified by seemingly irregular and chaotic three-dimensional vorticity composed of a large spectrum of eddy sizes. The presence of turbulence usually dominates all other flow features and results in increased energy dissipation, mixing, heat transfer and drag [Tennekes and Lumley, 1972].
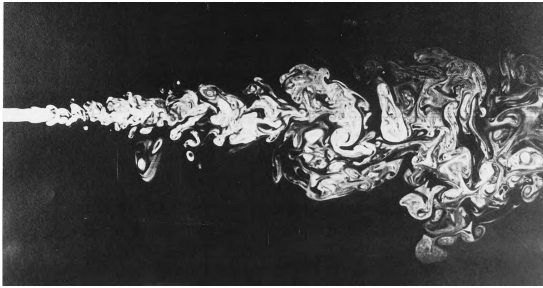
Figure 2.4: Visualisation of jet flow [Van Dyke, 1982].

These characteristics are illustrated in the visualisation of jet flow in Figure 2.4, which displays turbulent flow incorporating a wide spectrum of length scales, with large eddies of size comparable to the diameter of the flow, occurring alongside eddies of much smaller size [Hirsch, 2007]. Turbulent flow causes fluctuations in all variables of the flow: velocity, pressure, density, temperature, etc. which are statistical in nature and cannot be described in a deterministic way [Hirsch, 2007]. Figure 2.5 shows an example profile of a set of velocity measurements recorded at a fixed location over time. It can clearly be seen that the velocity is unsteady as it continually fluctuates over time. The velocity measurement is characterised by two components, the average velocity, $\bar{U}$, and its fluctuation about the mean, also referred to as the root mean square (RMS) turbulence velocity, U'. The RMS turbulence velocity is defined as:

$$U' = \sqrt{\overline{U - \bar{U}}^2}. \tag{2.29}$$

2.7 Turbulent Length Scales

Turbulent flow structures, such as the eddies observed in Figure 2.4 are characterised by three turbulent length and time scales:

- Integral scale, L_{int}

- Taylor scale, γ

- Kolmogorov scale, η
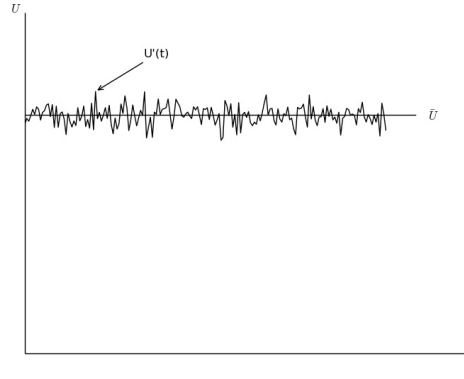
Figure 2.5: Generic point velocity measurement of turbulent flow.

The Integral Scale, L_{int}

This represents the largest turbulent scale where turbulent energy is stored. This scale is defined using the correlation between velocity measurements recorded at different locations within the flow field [Hirsch, 2007]. To achieve this velocity is typically measured at two different locations using an anemometer, one at a fixed location, x_o, and another at a moving point $x_o + \Delta x$. The covariance of the velocities at these two points is defined as:

$$U(x_o)U(x_o + \Delta x), \tag{2.30}$$

and the average covariance is given by:

$$\overline{U(x_i)U(x_i + \Delta x)}. \tag{2.31}$$

As the size of Δx decreases, $U(x_i + \Delta x)$ therefore approaches the value of $U(x_i)$ and results in equation 2.31 becoming U'^2. The correlation coefficient, R_x, of the

fluctuating velocity at two points, with respect to Δx, is given by:

$$R_x = \frac{1}{N_s - 1} \sum_{n=1}^{N_s} \frac{U(x_o)U(x_o + \Delta x)}{U'(x_o)U'(x_o + \Delta x)}. \tag{2.32}$$

R_x is at its maximum value when distance between the correlated points is minimised and tends towards zero as distance increases. The integral length scale is formally defined as the integral of R_x with respect to the distance x [Tennekes and Lumley, 1972]:

$$L_{int} = \int_0^\infty R_x dx. \tag{2.33}$$

Because this approach requires a significantly large number of repeated measurements there are other methods of calculating the integral scale, such as using Taylor's hypothesis and a single anemometer. This approach uses the time required for an eddy to pass the point measurement to calculate the integral scale.

2.7.1 Taylor's Scale

The Taylor micro-scale, γ, characterises the eddy scale in-between the largest integral scale and the smallest Kolmogorov length scales. This is defined by relating the RMS fluctuating strain rate to the RMS turbulence velocity [Pope, 2000]:

$$\frac{\partial U'}{\partial x} = \frac{\overline{U'^2}}{\gamma^2}. \tag{2.34}$$

Here the left hand side represents the mean strain rate.

2.7.2 Kolmogorov Scale

The Kolmogorov length scale, η, is the smallest length scale at which eddies exist before dissipating due to the action of viscosity. At this length scale the flow is

smooth. The Kolmogorov length scale and the time scale τ_η are expressed as:

$$\eta = \left(\frac{\nu^3}{\epsilon}\right)^{\frac{1}{4}}, \tag{2.35}$$

$$\tau_\eta = \left(\frac{\nu}{\epsilon}\right)^{\frac{1}{2}}. \tag{2.36}$$

Where ν is viscosity and ϵ is the energy dissipation rate per unit mass [Tennekes and Lumley, 1972, Landahl and Mollo-Christensen, 1992].

2.7.3   Relationship Between Length Scales

Most of the energy within turbulent flow is stored within the largest scale and is dissipated via the Kolmogorov length scale eddies within a time scale approximately equal to a single eddy life time ($\frac{U'}{L_{int}}$). The amount of energy stored is proportional to U'^2. In a state of equilibrium, the rate of turbulent energy supplied to the large scale eddies is equal to the rate of dissipation of the smallest eddies. This is defined as:

$$\epsilon = \frac{U'^3}{L_{int}} \tag{2.37}$$

By equating the rate of energy dissipation to the supply of energy with the Kolmogorov scale (in equation 2.35), the relationship between the integral and Kolmogorov scales are expressed as a function of the turbulent Reynolds number:

$$Re_{TL} = \frac{U'L_{int}}{\nu} \tag{2.38}$$

The relationship between the Kolmogorov and integral scale is defined as [Versteeg and Malalasekera, 2007]:

$$\frac{\eta}{L_{int}} = (Re_T)^{-\frac{3}{4}}. \tag{2.39}$$

The integral and Taylor scales are also related in a similar form:

$$\frac{\gamma}{L_{int}} = (Re_T)^{-\frac{1}{2}}. \tag{2.40}$$

2.8 Turbulence Modelling

Accurately modelling the complex behaviour of turbulent flow systems is an ongoing field of research. It is of significant interest because most fluid flows observed in nature are turbulent. As there are a large number of different modelling techniques available for turbulent flow, this section will not exhaustively detail every approach available. Instead, an overview of the most common methods applied will be given. These are:

- Direct Numerical Simulation (DNS)

- Large Eddy Simulation (LES)

- Reynolds-Averaged Navier Stokes (RANS)

For a more in-depth discussion on turbulence modelling the reader is directed to [Spalart, 2000].

2.8.1 Direct Numerical Simulation

DNS is usually applied to fundamental research applications at low Reynolds number and for simple geometries. This method has been used for a number of related studies encompassing the secondary flow features for helical channel flow [Hüttl and Friedrich, 2000, Hüttl and Friedrich, 2001, Yamamoto et al., 2000]. The DNS method directly solves the Navier Stokes equations on the discretised grid which is fine enough to resolve all turbulent length scales, including the smallest length scales; the Kolmogorov length scale.

As the smallest length scale is related to the turbulent Reynolds number, the grid spacing is also closely related to the turbulent Reynolds number. Therefore, by increasing the Reynolds number the Kolmogorov scale shrinks, consequently increasing the number of grid points required to resolve the smallest length scale. This is the major draw-back of DNS because enormous computational resources are required to solve the Navier Stokes equations for all of the scales. Therefore DNS will not be considered in this research.

2.8.2   Large Eddy Simulation

The central idea behind large eddy simulations is that small scale turbulence is more homogeneous and isotropic (non-directional) and can therefore be modelled more easily. This method consists of a number of key steps [Versteeg and Malalasekera, 2007]:

- Firstly, a selection of spatial filter function and a choice of length scale cut-off is made. The LES approach resolves all of the length scales within the length scale cut-off on the discretised grid in an unsteady flow computation.

- Next the spatial filtering is applied on the time-dependent flow-equations and the information relating to the scales outside of the cut-off limits are lost.

- The interactions between the larger resolved eddies and the smaller unresolved (cut-off) scales gives rise to Sub-Grid Scale stresses (SGS stresses). Their effect on the resolved flow is modelled by the means of a sub-grid-scale model.

It is important to note for the LES approach, that as grid density increases, the number of SGS modelled decreases until all length scales are resolved on the grid, therefore reaching the DNS approach. However, modelling challenges can arise when confronted with complicated geometrical formations which result in uneven

grid resolution. This uneven grid resolution introduces additional sub-grid stresses to be modelled only in select areas of the fluid domain [Ferziger and Perić, 2002]. LES remains very computationally demanding and will not therefore be used in this research

2.8.3 Reynolds-Averaged Navier-Stokes (RANS) Equations

Alternative approaches use empirical knowledge of the turbulent flow to remove computational complexity in resolving small scale structures. These methods typically use Reynolds averaging to decompose variables into two distinct components, the mean and the fluctuation about the mean. Hinze [Hinze, 1959] describes three averaging methods which can be applied depending on the characteristics of the turbulent flow.

- Stationary turbulence - Time averaging of a fixed point in space

- Homogeneous turbulence - Spatial averaging at a fixed time

- Ensemble averaging - Average calculated over a series of identical tests.

Each of the above averaging methods appears in two forms, unweighted (Reynolds) and weighted (e.g. density-weighted Favre averaging [Favre, 1965]). We can formally define a Reynolds averaged flow property, ϕ as:

$$\phi(x,t) = \bar{\phi}(x,t) + \phi'(x,t), \tag{2.41}$$

where $\phi'(x,t)$ denotes the fluctuation about the mean value. The mean value is calculated using ensemble averaging, defined as:

$$\bar{\phi}(x,t) = \lim_{N \to \infty} \frac{1}{N} \sum_{i=1}^{N} \phi_i(x,t), \tag{2.42}$$

where N is the number of experiments performed. The above average is then applied to the Navier Stokes equations to obtain the following averaged equations:

$$\boldsymbol{\nabla} \cdot \bar{\mathbf{U}} = 0, \tag{2.43}$$

$$\frac{\partial \bar{\mathbf{U}}}{\partial t} + \boldsymbol{\nabla} \cdot (\bar{\mathbf{U}}\bar{\mathbf{U}}) = g - \boldsymbol{\nabla} \bar{p} + \boldsymbol{\nabla} \cdot (\nu \boldsymbol{\nabla} \bar{\mathbf{U}}) + \boldsymbol{\nabla} \cdot (\overline{\mathbf{U}'\mathbf{U}'}). \tag{2.44}$$

The term $\overline{\mathbf{U}'\mathbf{U}'}$ is known as the Reynolds stress tensor. The objective of Reynolds averaged turbulence modelling is to express the Reynolds stress tensor in terms of known quantities. There are two common approaches which accomplish this:

The first approach formulates the transport equation for the Reynolds stress tensor. However, it is necessary to model some of the terms because the number of unknowns increases faster than the number of equations. The second and most common approach prescribes a relationship between the Reynolds stress and the mean velocity gradient. This relationship is most commonly described using the Boussinesq approximation, which proposes that the Reynolds stresses are proportional to the mean rates of deformation in the form of:

$$\bar{\mathbf{U}}'\bar{\mathbf{U}}' = \nu_t(\boldsymbol{\nabla}\mathbf{U} + (\boldsymbol{\nabla}\mathbf{U})^T) + \frac{2}{3}kI, \tag{2.45}$$

where ν_t is the kinematic eddy viscosity and k is the turbulent kinetic energy per unit mass, defined as:

$$k = \frac{1}{2}\overline{\mathbf{U}'.\mathbf{U}'}. \tag{2.46}$$

The kinematic eddy viscosity can be evaluated in a number of ways, the most popular approach expresses it as a function of the turbulent kinetic energy, k, and its dissipation rate ϵ:

$$\nu_t = C_\mu \frac{k^2}{\epsilon}, \tag{2.47}$$

$$\epsilon = \nu \overline{\mathbf{U}'\mathbf{U}'} : \overline{\nabla \mathbf{U}'}, \tag{2.48}$$

C_μ is a dimensionless constant. A transport equation is required for both, k and ϵ, resulting in a "two-equation" turbulence model. There are a variety of different $k - \epsilon$ turbulence models, such as Re-Normalisation Group (RNG) $k - \epsilon$ model [Yakhot et al., 1992], and realisable $k - \epsilon$ model [Wilcox, 1988], the most commonly used being the standard $k - \epsilon$ by Launder and Spalding [Launder and Spalding, 1974]. Currently there exists no turbulence model which can accurately represent all turbulent flows, which has led to the development of many different turbulence models to account for the extra terms which arise in the RANS.

2.8.4   The Standard $k - \epsilon$ Model

The standard $k-\epsilon$ turbulence model is currently the most popular turbulence model because it is widely established and has excellent performance against a range of flow situations. The $k - \epsilon$ turbulence model is highly applicable to helical flows as previous research encompassing helical flows using the $k - \epsilon$ model has found to accurately reproduce helical flow phenomena observed in experimental studies [Patankar et al., 1974, Versteeg and Malalasekera, 2007, Patankar and Spalding, 1972, Ito, 1959, Schlichting and Gersten, 2000].

In the description of the $k - \epsilon$ and latter turbulence models the rate of deformation and the turbulence stresses are used through-out. To aid the proceeding equations of turbulence modelling the components of the rate of deformation s_{ij} and the stresses τ_{ij} are expressed in tensor form:

$$s_{ij} = \begin{bmatrix} s_{xx} & s_{xy} & s_{xz} \\ s_{yx} & s_{yy} & s_{yz} \\ s_{zx} & s_{zy} & s_{zz} \end{bmatrix}, \tau_{ij} = \begin{bmatrix} \tau_{xx} & \tau_{xy} & \tau_{xz} \\ \tau_{yx} & \tau_{yy} & \tau_{yz} \\ \tau_{zx} & \tau_{zy} & \tau_{zz} \end{bmatrix}$$

where s_{ij} is decomposition into two components consisting of the mean and its fluctuation about the mean $s_{ij} = S_{ij} + s'_{ij}$.

The standard $k - \epsilon$ turbulence model consists of two equations, one for k, the turbulent kinematic energy and another for ϵ, the dissipation rate [Launder and Spalding, 1974]. The turbulence model focuses on the mechanisms which affect the turbulent kinetic energy. The instantaneous kinetic energy, $k(t)$, of a turbulent flow is expressed as the sum of the mean kinetic energy, K, and turbulent kinetic energy, k, where k is defined in Equation 2.46 and K is given by

$$K = \frac{1}{2}\mathbf{U} \cdot \mathbf{U}, \tag{2.49}$$

and

$$k(t) = K + k = \frac{1}{2}(\mathbf{U} \cdot \mathbf{U}) + \frac{1}{2}(\bar{\mathbf{U}}' \cdot \bar{\mathbf{U}}') \tag{2.50}$$

The characteristic length scale L_{int} can be determined algebraically using k and ϵ:

$$L_{int} = \frac{k^{\frac{3}{2}}}{\epsilon} \tag{2.51}$$

and the velocity scale as

$$\vartheta = k^{\frac{1}{2}} \tag{2.52}$$

Using ϵ to determine the large eddy scale L_{int} is permitted because at high Reynolds numbers, the rate at which large eddies extract energy across the mean flow is equal to that consumed by the small, dissipating, eddies. By applying dimensional analysis the eddy viscosity equation can be specified for the k ϵ turbulence model:

$$\nu_t = C_\mu \frac{k^2}{\epsilon}, \tag{2.53}$$

where C_μ is a dimensionless constant. For the standard $k - \epsilon$ turbulence model, the following transport equations for k and ϵ are solved:

$$\frac{\partial(\rho k)}{\partial t} + \boldsymbol{\nabla} \cdot (\rho k \mathbf{U}) = \boldsymbol{\nabla} \cdot \left[\frac{\mu_t}{\sigma_k} \boldsymbol{\nabla}(k) \right] + 2\mu_t S_{ij} \cdot S_{ij} - \rho \epsilon \qquad (2.54)$$

$$\frac{\partial \rho \epsilon}{\partial t} + \boldsymbol{\nabla} \cdot (\rho \epsilon \mathbf{U}) = \boldsymbol{\nabla} \cdot \left[\frac{\mu_t}{\sigma_\epsilon} \boldsymbol{\nabla}(\epsilon) \right] + C_{1\epsilon} \frac{\epsilon}{k} 2\mu_t S_{ij} \cdot S_{ij} - C_{2\epsilon} \rho \frac{\epsilon^2}{k} \qquad (2.55)$$

These equations are described in words as:

Rate of change of k or ϵ	+	Transport of k or ϵ by convection	=	Transport of k or ϵ by turbulent diffusion	+	Rate of production of k or ϵ	-	Rate of destruction of k or ϵ

It can be seen that these equations have five constants; $C_\mu, C_{1\epsilon}, C_{2\epsilon}, \sigma_k$ and σ_ϵ. The values for these constants are calculated from comprehensive data fitting for a wide range of turbulent flows:

$$C_{mu} = 0.09 \quad C_{1\epsilon} = 1.44 \quad C_{2\epsilon} = 1.92 \quad \sigma_k = 1 \quad \sigma_\epsilon = 1.3$$

2.8.5 Realisable $k - \epsilon$

Realisable $k - \epsilon$ is a recent development of the traditional $k - \epsilon$ turbulence model which contains a new formulation for the turbulent viscosity and a new transport equation for the dissipation rate [Shih et al., 1995]. The term realisable means that the turbulence quantities, such as k and ϵ, satisfy mathematical constraints on the normal stresses and are consistent with the physics of turbulent flows. The transport equations for the realisable $k - \epsilon$ are defined as follows:

$$\frac{\partial(\rho k)}{\partial t} + \boldsymbol{\nabla} \cdot (\rho k \mathbf{U}) = \boldsymbol{\nabla} \cdot \left[\mu_{eff} + \frac{\mu_t}{\sigma_k} \boldsymbol{\nabla}(k) \right] + P_k + P_b - \rho \epsilon - Y_M \qquad (2.56)$$

$$\frac{\partial \rho \epsilon}{\partial t} + \boldsymbol{\nabla} \cdot (\rho \epsilon \mathbf{U}) = \boldsymbol{\nabla} \cdot \left[\frac{\mu_t}{\sigma_\epsilon} \boldsymbol{\nabla}(\epsilon) \right] + \rho C_{1\epsilon} S \epsilon - \rho C_2 \frac{\epsilon^2}{k + \sqrt{\nu \epsilon}} + C_{1\epsilon} \frac{\epsilon}{k} C_{3\epsilon} P_b \quad (2.57)$$

Where P_k is the production term for kinetic energy due to mean velocity gradients and P_b is the production term due to buoyancy, which are each calculated using the same method as the standard $k - \epsilon$ model.

$$C_1 = max \left[0.43, \frac{\eta}{\eta + 5} \right], \eta = S\frac{k}{\epsilon}, S = \sqrt{2S_{ij}S_{ij}} \quad (2.58)$$

$$\mu_t = \rho C_\mu \frac{k^2}{\epsilon} \quad (2.59)$$

and Here $\overline{\Omega}_{ij}$ is the mean rate-of-rotation tensor viewed in a rotating reference frame

$$C_\mu = \frac{1}{A_0 + A_s \frac{kU^*}{\epsilon}}, \qquad U^* = \sqrt{S_{ij}S_{ij} + \hat{\Omega}_{ij}\hat{\Omega}_{ij}},$$

$$\hat{\Omega}_{ij} = \Omega_{ij} - 2\epsilon_{ijk}\omega k, \qquad \Omega_{ij} = \overline{\Omega}_{ij} - \epsilon_{ijk}\omega k,$$

with the angular velocity ω_k. A_0 and A_s are model constants:

$$A_0 = 4.04, \quad A_s = \sqrt{6} \cos \phi$$

$$\hat{S} = \sqrt{2S_{ij}S_{ij}} \quad (2.60)$$

$$C_{mu} = 1.44 \quad C_2 = 1.9 \quad \sigma_k = 1 \quad \sigma_\epsilon = 1.2$$

Since the proposal of the realisable $k - \epsilon$ model it is generally considered to be superior to the traditional $k - \epsilon$ and $k - \omega$ turbulence models because of its ability to deal with rotating flows. As a result of this it has and has been included in a number of CFD codes. However, this model has been noted in some particular cases to severely underestimate areas of high turbulent kinetic energy, although this is

true for all turbulence models of the $k - \epsilon$ family [Shih et al., 1995, Benhamadouche and Laurence, 2003].

2.8.6   RNG $k - \epsilon$

The renormalisation group (RNG) $k - \epsilon$ turbulence model is another variation of the $k - \epsilon$ turbulence model which was developed to account for the effects of smaller scales of motion through the use of a random forcing function. The RNG procedure systematically removes the small scales of motion from the governing equations by expressing their effects in terms of larger scale motions and a modified viscosity. The mathematics is highly complex and therefore only a quote of the RNG $k - \epsilon$ model equations for high Reynolds number flows given from Yakhot et al. [Yakhot and Smith, 1992, Versteeg and Malalasekera, 2007]:

$$\frac{\partial(\rho k)}{\partial t} + \boldsymbol{\nabla} \cdot (\rho k \mathbf{U}) = \boldsymbol{\nabla} \cdot [\alpha_k \mu_{eff} \boldsymbol{\nabla}(k)] + \tau_{ij} \cdot S_{ij} - \rho \epsilon \tag{2.61}$$

$$\frac{\partial \rho \epsilon}{\partial t} + \boldsymbol{\nabla} \cdot (\rho \epsilon \mathbf{U}) = \boldsymbol{\nabla} \cdot [\alpha_{eff} \mu_{eff} \boldsymbol{\nabla}(\epsilon)] + C_{1\epsilon}^* \frac{\epsilon}{k} \tau_{ij} \cdot S_{ij} - C_{2\epsilon} \rho \frac{\epsilon^2}{k} \tag{2.62}$$

Where:

$$\tau_{ij} = \rho \overline{U_i' U_j'} = 2\mu_t S_{ij} - \frac{2}{3} \rho k \delta_{ij} \tag{2.63}$$

$$\mu_{eff} = \mu + \mu_t, \mu_t = \rho C_\mu \frac{k^2}{\epsilon} \tag{2.64}$$

The model constants are defined below as:

$$C_{mu} = 0.0845 \qquad C_{1\epsilon} = 1.42 \qquad C_{2\epsilon} = 1.68 \quad \alpha_k = \alpha_\epsilon = 1.39$$

$$C_{1\epsilon}^* = C_{1\epsilon} - \frac{\eta(1 - \eta/\eta_0)}{1 + \beta\eta^3} \quad \eta = \frac{k}{\epsilon}\sqrt{2S_{ij} \cdot S_{ij}} \quad \eta_0 = 4.377 \qquad \beta = 0.012$$

For this model all model constants are calculated as part of the RNG process and only the constant β is tunable. The most attractive feature of this turbulence

model is that the ϵ-equation in the standard $k - \epsilon$ model has long been suspected as one of the primary sources of accuracy limitations, which this model attempts to improve. Yakhot et al. report very good predictions of the flow over a backward facing step and the improvements initially generated significant interest from the scientific community. This resulted in its inclusion into several commercial CFD codes [Yakhot and Smith, 1992]. However it has been noted by subsequent experiences challenges from the strain parameter, η, which sensitises the RNG model to the magnitude of strain. Therefore the effect of the dissipation rate is the same irrespective of the sign of the strain rate, which gives the same effect if a duct is contracting or expanding [Versteeg and Malalasekera, 2007].

2.8.7   The $k - \omega$ Model

The $k - \omega$ model proposed by Wilcox [Wilcox, 1988] is another commonly used turbulence model as it has been shown to accurately handle near-wall regions. This two-equation model uses the turbulence frequency, ω, as the second variable [Versteeg and Malalasekera, 2007]. The turbulent frequency is defined as:

$$\omega = \frac{\epsilon}{k} \tag{2.65}$$

The length scale and eddy viscosity is defined respectively as:

$$l = \sqrt{k}/\omega \tag{2.66}$$

$$\mu_t = \rho \frac{k}{\omega} \tag{2.67}$$

The $k - \omega$ model also expresses Reynolds stresses using the Boussinesq expression defined in Equation 2.45, which are written in tensor form as:

$$\tau_{ij} = -\rho \overline{u'_i u'_j} = 2\mu_t S_i j - \frac{2}{3}\rho k \delta_{ij} = \mu \left(\frac{\partial U_i}{\partial x_j} \frac{\partial U_j}{\partial x_i} \right) - \frac{2}{3}\rho k \delta_{ij}. \tag{2.68}$$

The transport equation for k is defined as:

$$\frac{\partial(\rho k)}{\partial t} + \boldsymbol{\nabla} \cdot (\rho k \mathbf{U}) = \boldsymbol{\nabla} \cdot \left[\left(\mu + \frac{\mu_t}{\sigma_k} \right) \boldsymbol{\nabla}(k) \right] + P_k - \beta^* \rho k \omega \qquad (2.69)$$

where the rate of production of turbulent energy, P_k, is defined as

$$P_k = \left(2\mu_t S_{ij} \cdot s_{ij} - \frac{2}{3} \rho k \frac{\partial U_i}{\partial x_j} \delta_{ij} \right). \qquad (2.70)$$

Finally the transport equation for ω is given by:

$$\frac{\partial \rho \omega}{\partial t} + \boldsymbol{\nabla} \cdot (\rho \omega \mathbf{U}) = \boldsymbol{\nabla} \cdot \left[\left(\mu + \frac{\mu_t}{\sigma_k} \right) \boldsymbol{\nabla}(k) \right] + \gamma_l \left(2\rho S_{ij} \cdot S_{ij} - \frac{2}{3} \rho \omega \frac{\partial U_i}{\partial x_j} \delta_{ij} \right) - \beta_l \rho \omega^2.$$
$$(2.71)$$

This is written in words as:

Rate of change of k or ω	+	Transport of k or ω by convection	=	Transport of k or ω by turbulent diffusion	+	Rate of production of k or ω	-	Rate of dissipation of k or ω

The default model constants are:

$$\sigma_k = 2.0, \quad \sigma_\omega = 2.0, \quad \gamma_l = 0.553, \quad \beta_l = 0.075, \quad \beta^* = 0.09.$$

The $k-\omega$ model initially attracted attention because integration to the wall does not require wall-damping functions at low Reynolds numbers. In the immediate proximity of the wall turbulent kinetic energy values are set to zero and the turbulence frequency ω tends to infinity. For this case large values for turbulence frequency can be specified at the wall or a hyperbolic variation ($\omega_p = 6\nu/(\beta_l y_p^2)$) at the near-wall grid point can be used [Wilcox, 1988]. Practical experience with the model has shown that the results do not depend too much on the precise details of this treatment [Versteeg and Malalasekera, 2007].

However, defining the boundary conditions of ω in a free stream can be difficult. This is caused by both turbulence kinetic energy k and ω tending towards zero. From inspecting Equation 2.67 it can be seen that eddy viscosity is indeterminate or infinite when ω tends towards zero [Menter, 1992]. The main draw-back of the $k-\omega$ model is that it is dependent on the assumed free stream value of ω, which is a serious problem in aerospace applications where free stream boundary conditions are frequently used.

2.8.8 The $k-\omega$ SST Model

It was noted by Menter that the results of the $k-\epsilon$ model are much less sensitive to the assumed values in the free stream, however its performance near solid boundaries is unsatisfactory for boundary layers with adverse pressure gradients [Menter, 1994]. This introduced the suggestion of a hybrid model which used the standard $k-\epsilon$ turbulence model in fully turbulent flow located far from the wall and a transformation from the $k-\epsilon$ model into a $k-\omega$ model at the near-wall region [Menter, 1994]. The Reynolds stress computation and the k-equation are the same as the $k-\omega$ model discussed above, however the $k-\epsilon$ equation is transformed into a ω-equation by substituting $\epsilon = k\omega$. This gives the following:

$$
\frac{\partial \rho\omega}{\partial t} + \boldsymbol{\nabla} \cdot (\rho\omega \mathbf{U}) = \boldsymbol{\nabla} \cdot \left[\left(\mu + \frac{\mu_t}{\sigma_{\omega,1}} \right) \boldsymbol{\nabla}(\omega) \right] + \gamma_2 \left(2\rho S_{ij} \cdot S_{ij} - \frac{2}{3}\rho\omega \frac{\partial U_i}{\partial x_j} \delta_{ij} \right)
$$
$$
- \beta_2 \rho\omega^2 + 2\frac{\rho}{\sigma_{\omega,2}\omega} \frac{\partial k}{\partial x_k} \frac{\partial \omega}{\partial x_k}
$$

$$(2.72)$$

It can be seen when comparing this equation to Eqn. (2.71) that there is an additional source term on the right hand side, this is known as the cross-diffusion term. The cross-diffusion term arises during the $\epsilon = k\omega$ transformation of the diffusion term in the ϵ-equation. Menter summarised a series of modifications to optimise the performance of the $k-\omega$ SST model based on experience with the model in

general-purpose computation which include blending functions to handle numerical instabilities which may be caused by differences in the calculated eddy viscosity between the $k - \epsilon$ and $k - \omega$ turbulence model. In addition to this limiters are introduced for eddy viscosity to improve model performance in flows with adverse pressure gradients as well as for turbulent kinetic energy to prevent the build-up of turbulence in stagnant areas [Versteeg and Malalasekera, 2007]. Finally the model constants are as follows:

$$\sigma_k = 1.0, \quad \sigma_{\omega,1} = 2.0, \quad \omega_{\omega,2} = 1.17, \quad \gamma_2 = 0.44, \quad \beta_2 = 0.083, \quad \beta^* = 0.09.$$

2.8.9 Reynolds Stress Model

The major draw-backs of the $k - \epsilon$ turbulence model appear when it is predicting flow with complex strain fields such as fully developed turbulent channel flow [Versteeg and Malalasekera, 2007]. This is a result of the linearity of eddy viscosity which causes significant errors in the calculation of Reynolds stresses. It has been proposed that Reynolds stresses should be modelled individually using the Reynolds stress model, which is also called the second order or second moment closure model [Launder et al., 1975]. In anisotropic turbulent flows, the eddy viscosity is treated as a tensor quantity. Therefore, each component of the Reynolds stress tensor is modelled using a separate equation.

The differential equations of the Reynolds stress model are obtained by adding the Navier-Stokes equation for U_i multiplied by U_j to the Navier Stokes equation for U_i' and applying the time averaging. The final differential equation of the Reynolds stress model after letting $R_{ij} = -\frac{\tau_{ij}}{\rho} = \overline{U_i' U_j'}$ is given by:

$$\frac{\partial R_{ij}}{\partial t} + \frac{\partial \bar{U}_k R_{ij}}{\partial x_k} = TD_{ij} + Gp_{ij} + G_{bij} + PS_{ij} - \rho \epsilon_{ij}, \tag{2.73}$$

this can be read in words as:

Rate of change of R_{ij}	+	Transport of R_{ij} by convection	=	Transport of R_{ij} by diffusion	+	Rate of production of R_{ij}	+	Rate of production of R_{ij} by body force
					+ Pressure strain correlation		-	Rate of destruction of R_{ij},

with

$$TD_{ij} = \frac{\partial}{\partial x_k} \left[\mu \frac{\partial R_{ij}}{\partial x_k} - \overline{p'U_j'}\delta_{ik} - \overline{p'U_i'}\delta_{jk} + \rho\overline{U_i'U_j'U_k'} \right]. \tag{2.74}$$

The first term on the right hand side represents diffusive transport due to molecular diffusion which is always neglected:

$$GP_{ij} = -\rho \left(R_{ik}\frac{\partial \bar{U}_i}{\partial x_k} + R_{ik}\frac{\partial \bar{U}_k}{\partial x_k} \right), \tag{2.75}$$

$$G_{bij} = \overline{U_j'F_i'} + \overline{U_i'F_j'}, \tag{2.76}$$

$$PS_{ij} = \overline{p' \left(\frac{\partial U_j'}{\partial x_i} + \frac{\partial U_i'}{\partial x_j} \right)}, \tag{2.77}$$

$$\epsilon_{ij} = \frac{2\mu}{\rho} \overline{\frac{U_j'}{x_k}\frac{\partial U_i'}{\partial x_k}}. \tag{2.78}$$

In three-dimensional flows there are strictly nine Reynolds stresses, but due to symmetry of the Reynolds stresses ($\tau_{ij} = \tau_{ji}$ or $\overline{U_j'U_i'} = \overline{U_i'U_j'}$) there are only six.

Despite having a greater potential resolving three-dimensional turbulent flows, it is a less commonly employed RANS approach than two-equation models. This is due to the additional computational cost required to solve the additional six equa-

tions for the Reynolds stresses. In addition to this, in some cases Reynolds stress models lead to poor convergence i.e. it is difficult to actually get a solution [Versteeg and Malalasekera, 2007].

2.8.10   Wall Functions

High Reynolds free-stream flow far from solid walls is very different to the low Reynolds behaviour of turbulent flow localised around walls; the differences are caused by differences in shear stresses. For most of the fluid domain shear stresses are small except for the layer of fluid immediately close to the solid surface. This is known as the boundary layer. Accurately modelling these regions can be crucial to the accuracy of a model, such as for heat transfer models where temperature change occurs across the fluid-wall interface. The most reliable method of resolving the turbulent boundary layer is to use a fine grid combined with a low-Re turbulence model [Jasak, 1996].

Increasing mesh resolution around solid no-slip surfaces to accurately resolve the near-wall region may not be feasible for many high Reynolds number engineering applications due to the increased computational costs. Experimental observation has confirmed that flows of all scales tend to demonstrate very similar patterns within the proximity of a wall. Wall-functions are simplified turbulence models based on empirical data which allow for wall compensation without fully resolving the near-wall region. This is achieved by treating the near-wall region like a fully developed turbulent boundary layer. Although these methods do reduce spatial discretisation costs, wall functions are found to be a useful compromise approach for many engineering applications as this performed at the expense of the approximation used for the wall-function [Launder and Spalding, 1974, Gosman et al., 1983].
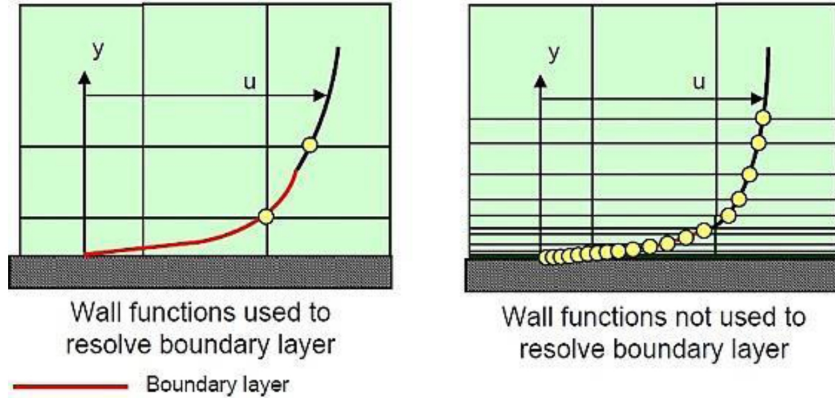
Figure 2.6: (Left) Illustration of the use of wall functions. (Right) Illustration of fully resolved boundary layer [Taherkhani, 2014].

Wall functions are characterised by two variables, the time-averaged velocity parallel to the wall, u^+, and the dimensionless normal distance from the wall, y^+. y^+ (illustrated in Figure 2.7) is a non-dimensional measurement of distance from the wall and describes the height of the first mesh element adjacent to the wall. y^+ is generally used to identify where in the boundary layer profile the first calculation point resides.

For y^+ values within the range of $y^+ \sim 1$ wall functions are not required as the grid is fine enough to resolve the boundary layer. For coarser meshes with $30 \leq y^+ \leq 500$, wall functions are required to calculate the near-wall velocity profile.

However, if the mesh is too coarse, the turbulence model may incorrectly calculate
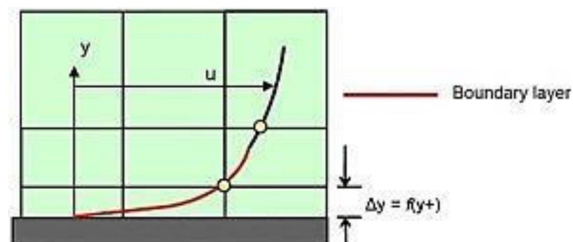
Figure 2.7: Definition of y^+ [Taherkhani, 2014].

flow properties in the near-wall region because the first calculation point will be located outside the boundary layer region. This can lead to errors in pressure drop

and velocity calculations.

On the other hand, errors can be introduced if the mesh is too fine. For very small y^+ values, the wall adjacent cell will be located in the viscous sub-layer which is outside the range of validity for the wall function. In the region of $y^+ < 5$ the
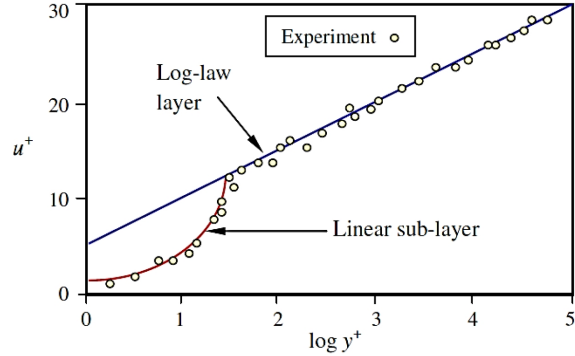
Figure 2.8: Dimensionless velocity distribution for the inner region of a boundary layer[Versteeg and Malalasekera, 2007].

following relation holds:

$$u^+ = y^+ \tag{2.79}$$

Further away from the wall the log-law layer exists for which $30 < y^+ < 500$ and the following relationship is true:

$$U^+ = \frac{1}{K}ln(E_C y^+) \tag{2.80}$$

The main advantage of using wall-functions comes from the significant reduction in mesh resolution requirements in the near-wall region and the associated reduction in computational costs. However, there are disadvantages if the boundary layer is not appropriately treated and the y^+ falls below 30 or increases above 500. This can result in unbounded errors in wall shear stress, wall heat transfer or flow features. Due to the decreased spatial discretisation costs wall-functions are widely used for three-dimensional turbulent flows. However, careful consideration is still required to

make this approach valid to ensure that near-wall turbulence is adequately treated.

2.9 Summary

In this chapter the governing equations for the through-tool flow of coolant and a short overview of turbulence modelling and wall functions has been given. From this chapter it has been deduced.

The analysis of operating parameters indicates the flow is fully turbulent and centrifugal forces generated by the curvature of the geometry have the dominant effect on the delivery of coolant.

Finally a short overview of turbulence modelling techniques and wall functions has been given. This overview indicates from previous research that the standard $k - \epsilon$ model will be a suitable turbulence model for simulating the highly turbulent through-tool coolant flow. This is investigated in greater detail below.

Chapter 3

Computational Fluid Dynamic Modelling of Internal Twist-Drill Coolant Channels

3.1   Introduction

This chapter outlines the methodology applied to model the flow of liquid coolant through rotating twist-drills. The steps taken include the decomposition of the problem domain, the construction of the computational mesh, rotation modelling and the choice of boundary conditions. This chapter will also give an overview of equation discretisation techniques and the solution procedure used to solve the discretised system of equations. This chapter will close with a model validation study which includes the analysis of mesh sensitivity, pressure drop calculations and axial velocity profiles.

3.2 Domain Decomposition

The use of coolant within twist-drill machining processes combines complex tool geometries with highly complex physical processes: the turbulent delivery of coolant, large speeds of rotation, cutting motion, heat generation, surface deformation, chip formation and chip evacuation. Modelling the entire process using a single model would not be feasible because a very complex mathematical model along with enormous computational resources would be required. Most of the complex physics are located at the cutting zone therefore processes such as the surface deformation, chip formation, chip evacuation, heat generation and transfer are isolated to this region. This is accomplished by implementing two coupled models:
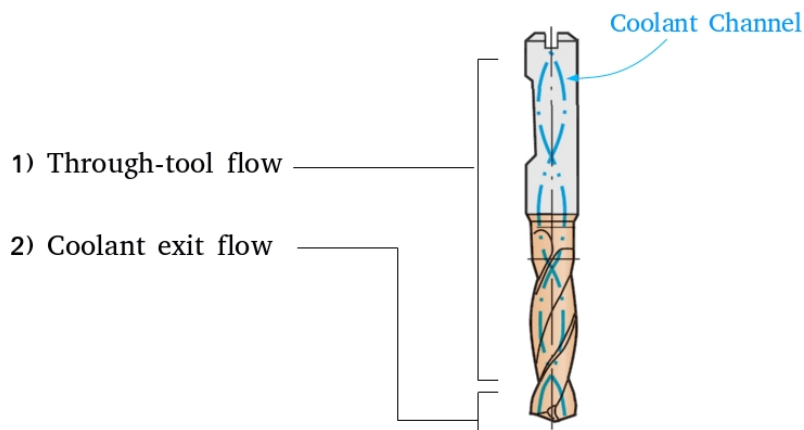
Figure 3.1: Problem domain decomposition

- Through-tool flow. A model for flow of liquid coolant in this region will focus on the simulation of coolant flow through the internal region of the tool, illustrated by figure 3.1. It will model steady state flow of isothermal, isoviscous and incompressible coolant through a helix rotating about its coiled axis. It is assumed isothermal because the heat generated during the cutting process is localised to the cutting zone.

- Coolant exit flow. The focus of this model will be on exit flow of coolant. As the coolant exits the drill the problem transforms from a single-phase problem

into a multi-phase problem. This model will have to consider solid phases for the tool and the material being machined, a single liquid phase for the coolant and finally a gas phase for the air located in the cutting zone. At this point a number of additional and highly complex physics may also need to be considered: surface tension, heat generation and transfer, compressibility, workpiece deformation and chip formation and chip evacuation.

3.3   Discretisation Method

This section outlines a number of steps for the numerical simulation of fluid flow problems. The first objective of the discretisation method is spatial discretisation of the problem domain, which involves describing the fluid domain in computational space as a set of points where the solution of the governing equations is sought. The second goal of the discretisation model is to approximate the governing equations of fluid flow as a system of algebraic equations which can then be solved on a computer. The most frequently used discretisation methods are the Finite-Difference, Finite-Element and Finite Volume methods. There are other methods available such as spectral-element methods, but because Finite-Difference, Finite-Element and the Finite Volume Methods are the most commonly used these will be outlines below [Cimbala and Çengel, 2008].

3.3.1   Finite Difference Method (FDM)

The Finite Difference Methods is the oldest discretisation method used and describes flow problem unknowns by means of point samples at node points of a grid. Finite difference approximations in terms of point samples at each grid point are generated by using Truncated Taylor series expansions. The derivatives which appear in the governing flow equations are replaced by the finite differences to yield an algebraic equation of flow quantity values at each grid point [Hirt and Kopp, 2009].

3.3.2 Finite Element Method (FEM)

The Finite Element Method (FEM) is most commonly used in structural engineering and fluid dynamics problems where fluid interacts with a solid medium. The spatial discretisation of the FEM employs shape functions to divide the geometry into a finite set of elements. The distinguishing feature of the finite element method is that the equations are multiplied by a weight function before being integrated across the entire domain. The properties of the complete structure are obtained by evaluating the properties of individual elements.

3.3.3 Finite Volume Method (FVM)

The Finite Volume Method (FVM) is a well-established and thoroughly validated CFD technique and is central to a number of commercial CFD software packages such as FLUENT, PHOENICS and OpenFOAM [Versteeg and Malalasekera, 2007]. The spatial discretisation of the FVM involves subdividing the fluid domain into a finite set of control volumes (also known as cells). The centre point of these finite control volumes are the locations where flow properties are calculated. The governing equations are then integrated over each control volume. This forms one of the main advantages FVM has over FEM which is the conservation of flow properties such as mass and momentum at a discrete level.

This conservation is expressed in words for flow property ϕ as:

Rate of change of ϕ in the control volume with respect to time	$=$	Net rate of increase of ϕ due to convection into control volume	$+$	Net rate of increase of ϕ due to diffusion into the control volume	$+$	Net rate of creation of ϕ inside the control volume

This conservation is useful for flows with sharp discontinuities and is satisfied at each cell volume and is therefore conserved for the entire computational domain for any number of control volumes. Next the integral equations are converted into a set of algebraic equations before being solved using an iterative method. Considering this key advantage, the FVM is used for this numerical analysis and is implemented using OpenFOAM [Weller et al., 1998]. The core steps of the Finite Volume Method will form the structure of the remainder of this chapter with a description of **spatial discretisation** methods used, an overview of **equation discretisation** techniques and finally the **solution procedure** used to solve the system of equations [Hirsch, 2007, Muzaferija, 1994].

3.4   Spatial Discretisation

Spatial discretisation of the solution domain concerns representing the fluid domain in computational space as a mesh consisting of a set of non-overlapping finite control volumes that completely fill the fluid domain. Each control volume is constructed out of a set of faces and a cell centre. This process determines the positions of the cell centres in space and time where flow variables such as $\mathbf{U}, p, k$ and ϵ are calculated and stored.
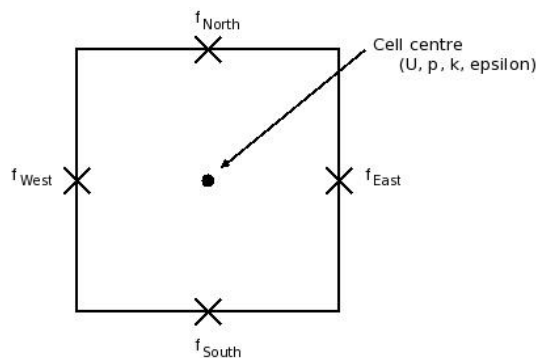
Figure 3.2: Control volume constructed out of a set of faces (north south east and west) with cell centre marked as ($\cdot$) and face centres marked as ($\times$).

Most CFD libraries are pre-packaged with pre-processing software which assists the process of computational mesh creation. The mesh of a helical coolant channel is constructed using a transformation approach. This approach creates the structured mesh of a simple straight pipe using the pre-processor blockMesh and then wraps the mesh around the centre-line of a helix. The mesh generated for the straight pipe is composed of 5 blocks and is illustrated in Figure 3.3. The centre-line of a helix
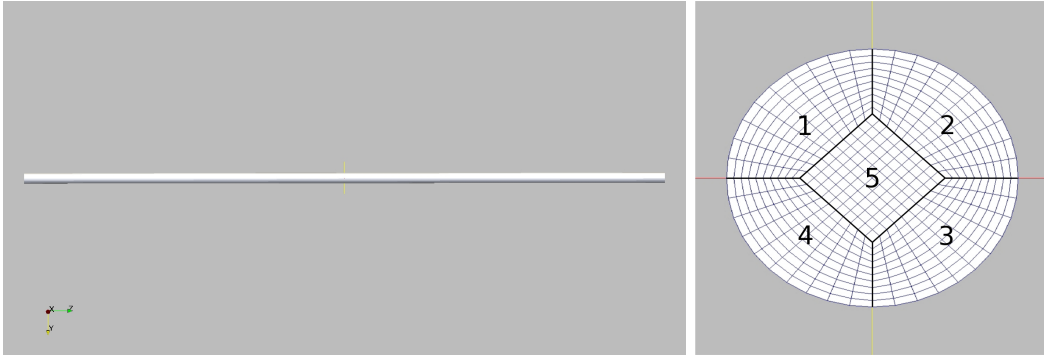
Figure 3.3: Illustration of the mesh of a straight pipe

with helix radius r and pitch θ is constructed using the equations:

$$x(t) = r\sin(t)$$

$$y(t) = r\cos(t) \tag{3.1}$$

$$z(t) = ct$$

Where r is the radius of the helix, c is a constant which defines the distance between coils. Tool pitch is defined as:

$$\theta = tan^{-1}(\frac{4r}{c}) \tag{3.2}$$

To facilitate the transformation, the position along the arc length of the straight pipe corresponds to the position along the helix arc length. The z coordinates of

points which make up the straight pipe identify the point's position along the arc length of the straight pipe. This information is used with the Frenet-Serret formulae (Eqn. 3.3) to map the arc length of the straight pipe, $\mathbf{P}(s)$, to the corresponding helical centre-point position at the corresponding arc length position, $\mathbf{R}(s)$. The Frenet-Serret Formulae define $\mathbf{T}(s)$, $\mathbf{N}(s)$ and $\mathbf{B}(s)$, which are the tangent, normal and bi-normal unit vectors at the helix arc length, s and are presented in Figure 3.4.
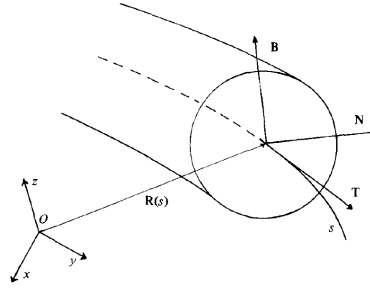
Figure 3.4: Illustration of the Frenet-Serret Formulae [Germano, 1982]

$$\mathbb{T} = \frac{d\mathbb{R}}{ds},$$

$$\mathbf{N} = \frac{1}{\kappa}\frac{d\mathbf{T}}{ds},$$

$$\mathbf{B} = \mathbf{T} \times \mathbf{N}, \tag{3.3}$$

$$\frac{d\mathbf{N}}{ds} = \tau\mathbf{B} - \kappa\mathbf{T},$$

$$\frac{d\mathbf{B}}{ds} = -\tau\mathbf{N},$$

where κ is the curvature and τ is torsion defined as:

$$\kappa = \|\frac{d\mathbf{T}}{ds}\| \qquad\qquad \tau = \|\frac{d\mathbf{B}}{ds}\|$$

The transformation is performed by translating points of the straight pipe mesh by the appropriate centre point of the helix before rotating by the $\mathbf{N}(s)$ and $\mathbf{B}(s)$

unit vectors to correct the inclination of the cross section. This transformation is expressed formally as

$$H(s) = R(s) + P_x(s)\mathbf{N}(s) + P_y(s)\mathbf{B}(s) \tag{3.4}$$

Here $H(s)$ is the transformed position of any point along the arc length s, $P_x(s)$ and $P_y(s)$ are the cross sectional x and y coordinates respectively of any point along the straight pipe at arc length s.
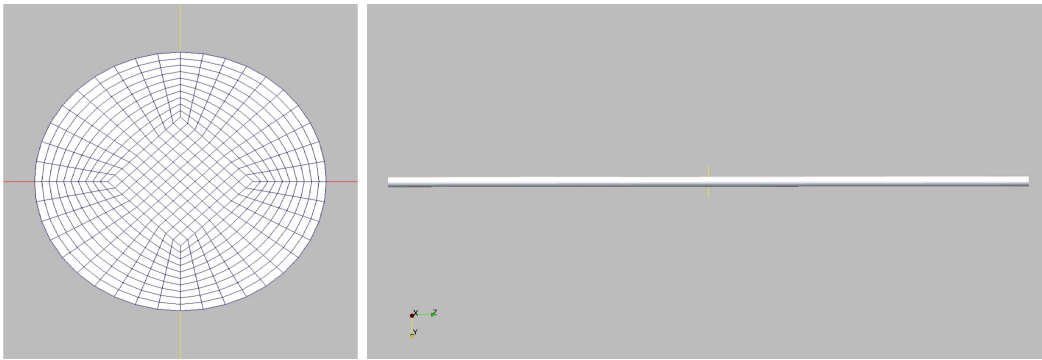
Figure 3.5: Geometry before transformation
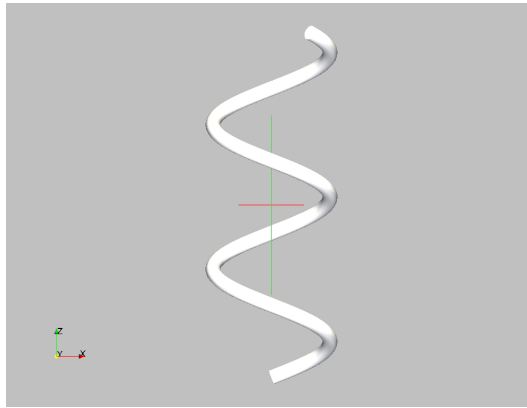
Figure 3.6: Geometry after the transformation

3.5 Rotating Geometry

Rotation is a central process of twist-drill machining and cannot be neglected from the model. Because the fluid domain and all of its boundaries are rotating about the

same axis in the same direction and at the same number of revolutions per minute only a single frame of reference is required.

Rotation is included by computing the Navier-Stokes equations in a rotating frame of reference, where velocity and mass flow are defined relative to the rotating frame of reference:

$$\mathbf{U}_R = \mathbf{U} - \boldsymbol{\Omega} \times \mathbf{r}, \tag{3.5}$$

where $\mathbf{U}_R$ is velocity relative to the rotating frame of reference, $\boldsymbol{\Omega}$ is the rotational direction vector and $\mathbf{r}$ is the position vector from the centre of rotation [Nilsson, 2014]. Coriolis and Centrifugal forces generated by the angular momentum are included in the model by introducing the effects as source terms in the steady-state incompressible Navier Stokes equations given by:

$$\boldsymbol{\nabla} \cdot \mathbf{U}_R = 0 \tag{3.6}$$

$$\boldsymbol{\nabla} \cdot (\mathbf{U}_R \otimes \mathbf{U_R}) + \underbrace{2\boldsymbol{\Omega} \times \mathbf{U}_R}_{\text{Coriolis}} + \underbrace{\boldsymbol{\Omega} \times (\boldsymbol{\Omega} \times \mathbf{r})}_{\text{Centrifugal}} = -\boldsymbol{\nabla}(\frac{p}{\rho}) + \nu \boldsymbol{\nabla} \cdot \boldsymbol{\nabla} \mathbf{U}_R \tag{3.7}$$

3.6 Boundary Conditions

The computational mesh generated in Section 3.4 is constructed from a finite set of non-overlapping control volumes and each of these volumes is made up of a set of faces. The conditions prescribed to the faces located at the boundary of the domain need to be specified to provide start and end points for the solution procedure. These conditions are specified through the use of boundary conditions and require careful consideration because inappropriate boundary conditions may produce unrealistic or inaccurate results.

There are two basic types of numerical boundary condition, Dirichlet (also known as

fixed value) and Von Neumann boundary conditions. Dirichlet boundary conditions prescribe the value of a variable on the boundary whereas Von Neumann boundary conditions prescribe the gradient of the variable normal to the boundary face [Jasak, 1996].

The physical boundary conditions of the internal coolant channel are the channel walls, inlet and outlet. The treatment of each of fluid variable needs to be specified at each physical boundary through the application of the basic numerical boundary conditions outlined above or by other more complex boundary conditions which employs a mixture of the basic numerical boundary conditions.

Inlet boundary. The distribution of the velocity field at the inlet is specified as the average velocity for mass flow rate using a fixed value boundary condition. The average velocity is calculated using the following equation:

$$U = \frac{m}{\rho A},$$
(3.8)

where m is mass flow rate, ρ is fluid density and A is the cross-sectional area of the channel. The boundary condition on pressure is zero gradient for consistency [Hirsch, 2007]. For turbulent variables, k and ϵ, are assigned fixed value boundary conditions.

Outlet boundary. Atmospheric pressure at the outlet is specified using a Dirichlet boundary condition. The velocity distribution is not required therefore a zero gradient boundary condition is selected for velocity. Because the mass flow through the system is specified at the inlet, this configuration calculates the pressure drop across the channel for the prescribed flow rate. Mass conservation is guaranteed by the pressure equation [Jasak, 1996]. For turbulence variables the boundaries are

prescribed the zero gradient boundary condition.

Impermeable no-slip walls. The velocity of the fluid on the wall is equivalent to the velocity of the wall itself, therefore a fixed value boundary condition is used. Because the mass flow through the impermeable wall is zero, the pressure gradient is therefore specified as zero gradient.

3.7 Discretisation Schemes

Following the integration of the governing equations over each control volume which make up the fluid domain, the integral equations are converted into a system of algebraic equations by approximating convection, diffusion and source terms which requires the use of differencing schemes to express variable values at cell faces. The role of differencing schemes is to determine the value of flow property ϕ on cell faces based on local cell centre values and there are many approaches available which seek to find an acceptable balance between accuracy and boundedness. Rather than give an exhaustive discussion of all differencing schemes available this section will give a short overview on the most basic techniques central, upwind and blended differencing. For a more in-depth discussion of differencing schemes the reader is directed towards [Jasak, 1996].

Central Differencing

Central Differencing (CD) assumes a linear variation of ϕ between neighbouring cell centres E and W. Face values are calculated according to [Versteeg and Malalasekera, 2007, Jasak, 1996]:

$$\phi_f = f_x \phi_W + (1 - f_x)\phi_E. \tag{3.9}$$

Here f_x is the interpolation factor which is defined as the ratio of $\overline{fE}$ to $\overline{WE}$. $\overline{fE}$ is the distance from the face to the cell centre of E and $\overline{WE}$ is the distance from the cell centre of cell W to the cell centre of E. This is given by:

$$f_x = \frac{\overline{fE}}{\overline{WE}} \tag{3.10}$$

Central differencing is illustrated through a 1D example in Figure 3.7, which shows the calculation of ϕ on face f which is shared between two neighbouring cells E and W. This differencing scheme has been shown to be second order accurate even in non-uniform meshes. The most significant issue with this differencing scheme is that unphysical oscillations can occur in the solution for convection-dominant problems [Patankar and Spalding, 1972, Hirsch, 2007, Ferziger and Perić, 2002]. Another draw-back of central differencing is its inability to recognise the direction of flow which makes it unsuitable for convection dominant flows. Therefore CD is less appropriate for discretising convection terms, but more useful for diffusion terms.
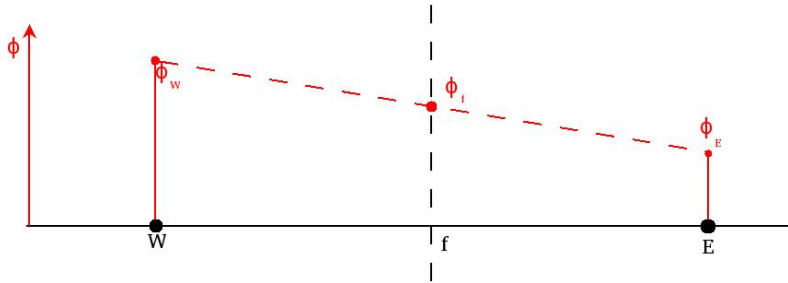
Figure 3.7: Interpolation Diagram: Central Differencing

Upwind Differencing

The key feature of Upwind Differencing (UD) is its use of direction of flow to determine the face value of ϕ. Face values are calculated according to [Versteeg and

Malalasekera, 2007, Jasak, 1996]:

$$
\phi_f =
\begin{cases}
\phi_f = \phi_W & \text{if } F \geq 0. \\
\phi_f = \phi_E & \text{if } F < 0.
\end{cases}
$$

Here F indicates the direction of mass flux. Positive F corresponds to flow in the positive direction. This scheme is illustrated in Figure 3.8, which demonstrates a single dimensional example of calculating face centre values of ϕ using upwind differencing between two neighbouring cells E and W. The face shared between these cells, f, is marked as the vertical black dashed line and the direction of flow is marked by the arrow labelled F. The vertical axis represents the value of ϕ and the solid red line indicates the value of ϕ at the cell centres W, E and face f when applying upwind differencing. As can be seen from the Figure, the flow is directed from cell W to cell E and therefore the value of ϕ at the intermediate face is assigned the value of W. It is the ability to recognise the direction of flow that makes this differencing scheme most useful in the discretisation of the convection term, but less appropriate for the treatment of the diffusion term of the governing equation.
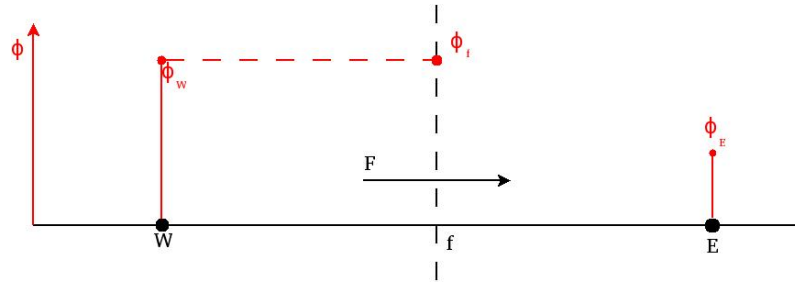

Figure 3.8: Interpolation Diagram: Upwind Differencing.

Blended Differencing

Blended Differencing (BD), is a combination of UD and CD which aims to preserve the boundedness and accuracy of the solution [Peric, 1985, Jasak, 1996]. This

method uses a blending factor, γ to determine the amount of numerical diffusion to be introduced. BD is given by:

$$\phi_f = (1 - \gamma)(\phi_f)_{UD} + \gamma(\phi_f)_{CD}. \tag{3.11}$$

where γ is in the range of $0 \leq \gamma \leq 1$. When $\gamma = 1$ reduces the scheme to CD and when $\gamma = 0$ the scheme is reduced to UD. Although the amount of blending required to preserve boundedness varies between faces, Peric proposes a constant γ for all faces of the mesh [Peric, 1985]. This approach potentially is more accurate, however it is not known how much blending should be used.

3.8   Solution procedure

Following the discretisation of the solution domain and the conversion of the governing equations into a set of algebraic equations it is now necessary to describe the solution procedure for the Navier-Stokes equations and the additional coupled transport equations to account for turbulence. This process gathers all of the components: the computational mesh, boundary conditions, and equation discretisation to solve the governing equations.

The underlying physical phenomena are highly complex and because the associated equations are non-linear an iterative solution procedure is required.

3.8.1   The SIMPLE Algorithm

The SIMPLE algorithm was developed by [Patankar and Spalding, 1972] and is frequently used within numerical procedures solving fluid flow and heat transfer problems. SIMPLE is an acronym for Semi-Implicit Method for Pressure Linked Equations. Instead of simultaneously solving the momentum and continuity equa-

tions to calculate the pressure and velocity fields, the equations are decoupled so that pressure and velocity fields are solved in a segregated manner. The following iterative procedure is repeated until the flow field satisfies convergence criteria:

1 Apply the boundary conditions.

2 Assemble and solve the momentum equation using the previous iteration or initial conditions.

3 Compute mass fluxes at each cell face.

4 Solve the pressure equation and apply under-relaxation.

5 Correct the mass fluxes at each cell face.

6 Correct the velocities on the basis of the new pressure field.

7 Solve the remaining equations (such as k and ϵ) in the system using available fluxes, pressure and velocity fields.

8 Check the convergence criteria for all equations. If the criteria are satisfied stop, otherwise begin a new iteration from step 2.

3.9   Model Validation

In order to validate the model it is necessary to compare the calculated phenomena against the flow observed within rotating twist-drills. However in practise it was not possible to accurately experimentally measure pressure drop through rotating twist drills, or observe the axial flow profile. In addition to these difficulties there is also a general lack of experimental data which can be related to the flow of coolant. This may perhaps be because the geometry of the twist-drills considered are so small, with very large speeds of rotation and Reynolds numbers. In light of the limited experimental data to compare the model against, this section uses

the available data to validate the model through three stages: mesh sensitivity analysis, turbulence model sensitivity analysis, friction factor analysis and finally flow structure analysis.

3.9.1 Mesh Sensitivity Analysis

The accuracy of the model is dependent on the number of cells used to represent the fluid domain. If too few cells are used small scale structures may not be resolved and if too many cells are used the computational cost will be unfeasibly large. A mesh sensitivity study was carried out to gain the best compromise between accuracy and performance (in terms of calculation time). This study examines the change in calculated pressure drop for a fixed flow rate as the number of cells in the mesh changes.

As a result of adopting the transformation approach described in Section 3.4 when creating the computational mesh, mesh resolution is not defined relative to global Cartesian coordinates. Mesh resolution is defined relative to the helix arc length and across the diameter of each channel cross section. Where arc length resolution represents the number of cross sections used to represent the channel. The effects of mesh resolution are studied by examining calculated pressure drop as a function of arc length resolution and cross section resolution for an extreme case of 60° pitch, drill length 40mm and radial spacing of 3.3mm. The results shown in Figure 3.9 (Left) examine the change in calculated pressure drop as the number of cells across the diameter of each cross section varies. Pressure drop calculations were found to fluctuate by less than 2% when increasing resolution. The resolutions circled in Figure 3.9 mark the selected refinement level. This resolution was deemed suitable because the increase in computational cost associated with the increase in mesh density does not have a significant effect on the solution. (Right) displays the total number of cells against the predicted pressure drop, where cross section resolution

Figure 3.9: Mesh sensitivity study, the change in predicted pressure drop when changing (Left) cross section resolution across the diameter and (Right) arc length resolution.

is constant and arc length resolution is iteratively increased. The circled point is the selected level of refinement for the model of through-tool flow because predicted pressure drop varies by less than 5% when further increasing the mesh density by a factor of 2 and is therefore suitably accurate whilst minimising the computational cost.

For this level of refinement a y^+ value of 50 was calculated. As explained in Section 2.8.10, y^+ is the non-dimensional measurement of distance from the wall and describes the height of the first cell adjacent to the solid wall boundary. Values within the range of $30 \leq y^+ \leq 200$ are suitably refined to enable wall functions to resolve the boundary layer, because the y^+ value falls within his range the mesh is not too coarse or overly refined to accurately calculate the near wall velocity.

3.9.2 Turbulence Model Sensitivity Analysis

A study of turbulence models was carried out in order to identify how sensitive model calculations are to the choice of turbulence model. This study was performed by simulating through-tool coolant flow for a range of Reynolds numbers using a number of different turbulence models. The turbulence models examined were the

standard $k - \epsilon$, RNG $k - \epsilon$, realisable $k - \epsilon$ the $k - \omega$ SST turbulence models. The basis for each of these turbulence models is given in Section 2.8. Figure 3.10
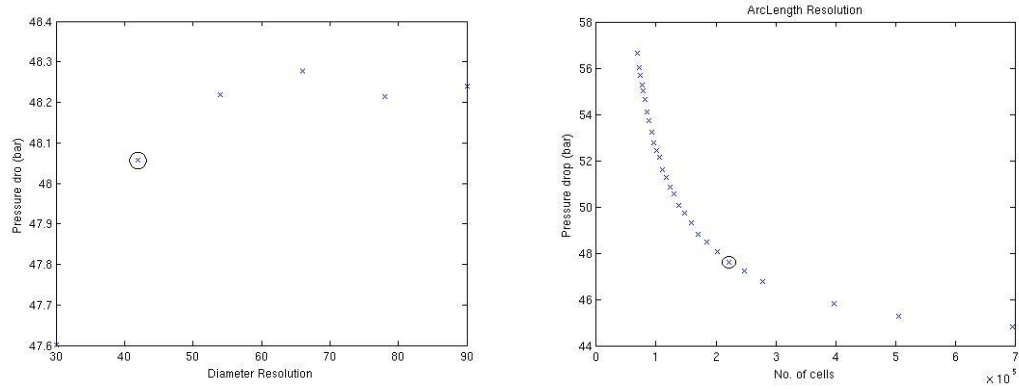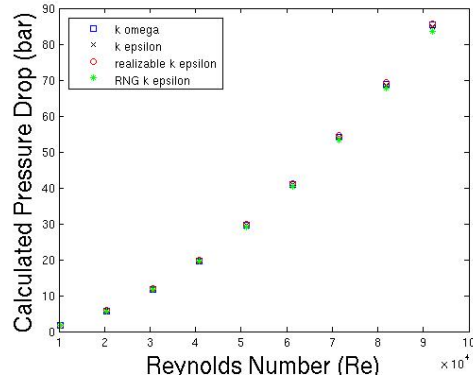

Figure 3.10: Mesh sensitivity study, the change in predicted pressure drop when changing (Left) cross section resolution across the diameter and (Right) arc length resolution.

shows the calculated pressure drop as a function of the Reynolds number for each turbulence model. It can be seen that the calculated pressure drop for through-tool coolant flow is not very sensitive to the choice of turbulence model. It was found that the variation between models increases with an increase in Reynolds number and the worst case varies between one and two percent which is at an extreme case of $Re = 92,000$. Therefore the standard $k - \epsilon$ model was selected as the turbulence model because it has been shown in previous research encompassing helical flows and to have good agreement with experimental data [Patankar et al., 1975].

3.9.3   Friction Factor Analysis

In order to validate the pressure drop calculations it is necessary to compare the CFD against experimental measurements. Because it was not possible to experimentally measure the pressure drop across the length of the tool this study uses experimental data from previous research. Friction factor correlations derived from stationary helical flows by [Guo et al., 2001] are used since experimental data encompassing rotating helical flows for similar Reynolds numbers could not be found.

Guo [Guo et al., 2001] experimentally investigated the pressure drop due to friction in stationary helical flows at Reynolds numbers of up to 150,000. [Ito, 1959] and [Srinivas et al., 1968] also experimentally measured the pressure drop through stationary helices, however for smaller Reynolds number below the range of interest for this study. Friction factors were calculated using the implemented model for stationary helical flow simulations using the same expression:

$$\boldsymbol{\nabla} p = \frac{f_c}{4} \frac{n\pi R}{r} \frac{\rho U^2}{2},$$ (3.12)

where f_c is the friction factor for curved pipes, n is the number of coil loops and U the average fluid velocity in m/s. Figure 3.11 shows friction factor predictions as a function of Reynolds number for the present model and experimental correlations of [Guo et al., 2001, Srinivas et al., 1968, Ito, 1959]. This figure shows that there is a lack of consistency between friction factor calculations. The work of Guo experimentally investigates helical flows at corresponding Reynolds numbers for this work $(40,000 \leq Re \leq 80,000)$. The present model calculates friction factor coefficients within 20% of Guo's friction factor correlation [Guo et al., 2001], which is reasonable considering the large disparity in geometries: the experimental research undertaken by Guo examines the frictional pressure drop in helices of which are ten times larger in channel diameter. In order to fully understand the frictional pressure loss occurring in through-tool coolant channel flow must be experimentally investigated, however that is currently difficult considering the small geometry and large number of revolutions per minute.

3.9.4   Flow Structure Analysis

The flow structures observed in helical channel flow have been extensively researched [Yamamoto et al., 2000, Yamamoto et al., 2002, Yamamoto et al., 1998, Yamamoto et al., 1994, Alam et al., 2007, Yamamoto et al., 1995, Zhang and Zhang, 2003].
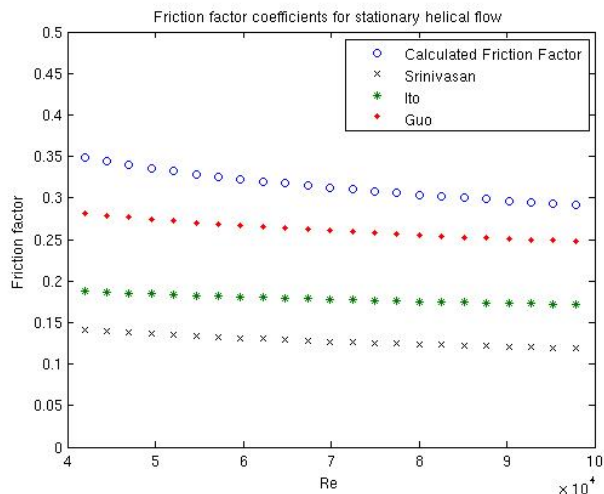
Figure 3.11: Comparison of friction factor coefficients, model ∘ (numerical), Guo ⋄ [Guo et al., 2001], Srinivas × [Srinivas et al., 1968], Ito * [Ito, 1959].

To validate the flow structures calculated, the flow field located at the outlet of the geometry is compared to the typical flow field of the above research. Figure 3.12 compares contours of the axial flow calculated by Yamamoto for co-rotating helices. Their research numerically studies helices of different curvature and torsion at much smaller Dean numbers, although the size, shape and number of cells will be different for this research a similar axial motion is to be expected. Figure 3.12 compares the axial velocity contours of the present model (Left) with the axial velocity contours predicted in [Yamamoto et al., 2000]. The axial velocity contours of Yamamoto [Yamamoto et al., 2000] illustrate generic helical channel flow where the location of maximum velocity has migrated to the outside edge of the helix. This behaviour is consistent with present results shown on the left.

3.10   Summary

This chapter has described the construction of a numerical model based on open source software which uses the finite volume method to discretise the solution domain using a transformation approach, discretise the equations and solve the gov-
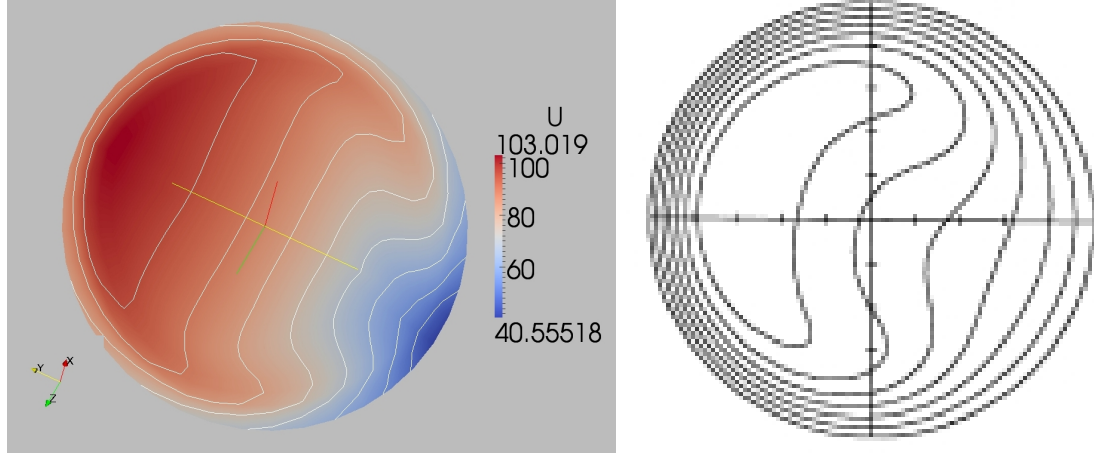
Figure 3.12: (Left) Axial helical velocity contour from our model. (Right) Axial velocity contour calculated by Yamamoto [Yamamoto et al., 2000]

erning equations using the SIMPLE algorithm.

Although there is only limited relevant data available, the accuracy of the model has been studied by the means of a mesh sensitivity study, turbulence model sensitivity study, friction factor and flow structure analysis. The mesh sensitivity study was performed to examine the effects of mesh resolution in order to gain the best balance of model accuracy and performance. Several different turbulence models have been used in a turbulence model sensitivity study which analysed pressure drop calculations for a range of Reynolds numbers across a range of different turbulence models. This study found that the pressure drop calculations were not very sensitive to the choice of turbulence model and varied by at most 1.5% for an extreme case. The pressure drop calculated has been compared against experimental data [Guo et al., 2001] and finds reasonable agreement with this experimental data. Flow structure analysis was finally performed to check that the calculated flow field is accurate. This was compared against generic pipe flow found in a number of studies and is found to be consistent.

Chapter 4

CFD Analysis of Through-Tool Coolant Flow

4.1 Introduction

In the Chapters 2 and 3 the governing equations of the numerical model and the modelling methodology are outlined respectively. This chapter uses the numerical model described in the previous two chapters to analyse the internal flow of coolant through rotating drills. A parametric study is carried out to examine the influence of each design parameter. This chapter also includes a brief overview of metamodelling techniques and closes with multi-dimensional analysis of tool parameters using metamodelling techniques.

4.2 Parametric Study

There are four design parameters which govern the size and shape of the coolant channel geometry. Each parameter is illustrated in Figure 4.1: channel pitch (in degrees), tool length, channel spacing and channel positioning. The parametric study presented in this section seeks to use the CFD model developed in the previous
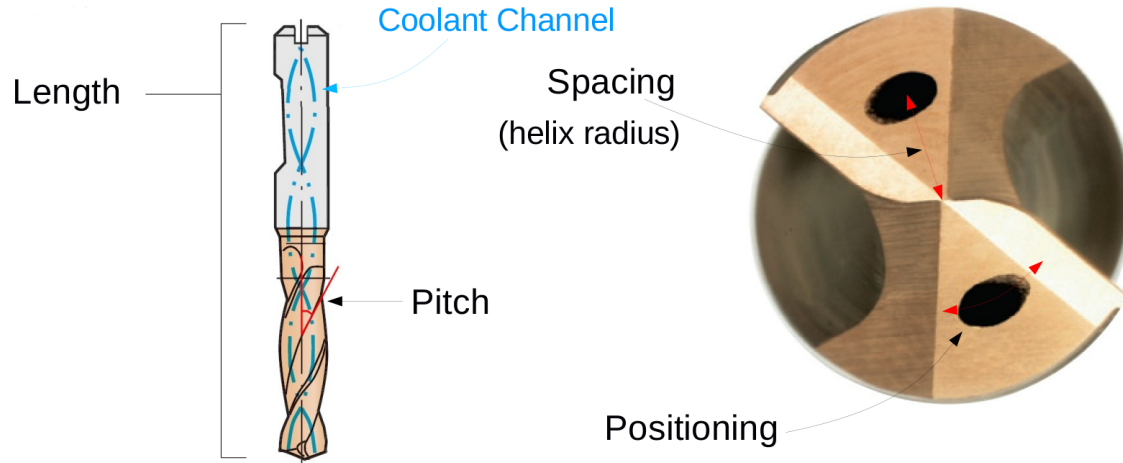
Figure 4.1: Overview of geometry parameters.

chapter to analyse the effect of each parameter on pressure drop.

4.2.1 Effect of Tool Length

The first parameter investigated was tool length. The aim of this study was to analyse the change in pressure drop along the internal coolant channel as the length of the tool changes. This was investigated by calculating the pressure drop for a fixed flow rate through a helical channel of pitch 30°, channel diameter 1mm and channel spacing of 3.3mm with an iteratively increasing tool length. Figure 4.2 shows the predicted pressure drop as a function of tool length and clearly shows that the pressure drop across the helical channel increases linearly with tool length.

4.2.2 Effect of Rotational Speed

The aim of this study was to analyse the effect of speed of rotation on the flow of coolant through rotating twist drills. The influence of rotation on coolant flow was analysed by calculating pressure drop for a fixed flow rate through a representative geometry of coolant channel of 1mm in diameter located 3.3mm from the centre of
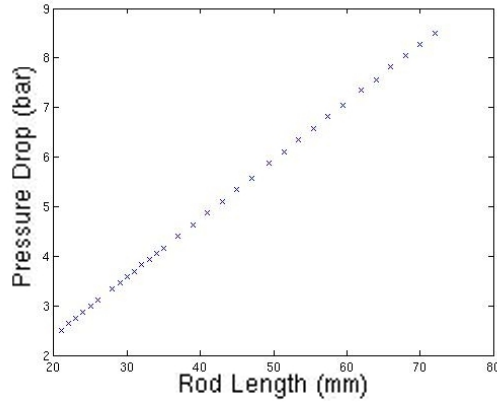
Figure 4.2: Pressure drop calculation in response to a change in tool length.

a 40mm tool with flute pitch of 30°. Pressure drop was calculated for the specified geometry at speeds of rotation between 0 and 10,000rpm. Figure 4.3 displays the results from this investigation and shows pressure drop as a function of speed of rotation in rpm. It can be seen that as the speed of rotation increases the calculated pressure drop increases at a very small and constant rate.

The co-rotating and counter rotating helical channel flow has been researched by Yamamoto [Yamamoto et al., 2000]. Yamamoto's numerical modelling of rotating helical channels concluded that for cases of co-rotating helices the centrifugal and Coriolis secondary flow forces act in the same direction and operate in an additive sense. As a result this strengthens the secondary flow and reduces the flow rate. However, for

Figure 4.3: Pressure drop calculation in response to a change in the speed of rotation.

counter-rotating flows, the Coriolis and centrifugal forces operate in opposite directions and are in competition with each other, which has a destabilising effect on the

secondary flow. For further information the reader is referred to Section 1.4.3 .

In the application of twist-drill machining, the problem is bound to co-rotation due to the geometry of the cutting tool. Therefore it is expected, based on the work of Yamamoto [Yamamoto et al., 2000], that an increase in speed of rotation will result in an increase in calculated pressure drop. This is consistent with the results demonstrated in Figure 4.3. However, for such a large difference in revolutions per minute there is very little variation in the calculated pressure drop.
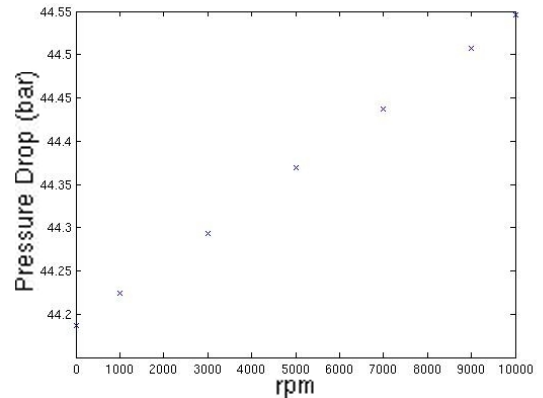
The small change in calculated pressure drop due to the motion of rotation is related to the Rossby number, as introduced in Section 2.5.2. The Rossby number suggests the relative importance of the effects of rotation on fluid flow systems. A Rossby number over the limit of 1 suggests that angular velocity is not very influential on the fluid flow. Section 2.5.2 found that the Rossby number for the problem in question is within the region of $12 \leq Ro \leq 250$ and therefore the speed of rotation is not expected to have a significant influence on the delivery of coolant. This is mirrored in the pressure drop calculations in Figure 4.3. Therefore it can be seen that the axial velocity of the flow dominates the Coriolis forces. This is due to coolant channels being located millimetres away from the centre of rotation, which despite the tool rotating at up to 10,000 rpm the angular velocity of the channel (up to 5m/s) is still an order of magnitude less than the axial velocity of the coolant. Moreover, when coolant traverses the geometry at up to 80m/s the coolant can enter and exit the tool before the tool has rotated a fraction of a degree. It is therefore concluded that in order for rotation to play a more significant role in the delivery of coolant, angular velocities will need to significantly increase by up to 20 times, or by locating coolant channels further from the centre of rotation.

4.2.3 Effect of Pitch

Helix pitch (also referred to as flute angle) is the angle of inclination of the internal coolant channel, defined as $\theta = tan^{-1}(\frac{4R}{c})$ where R is helix radius and c is the vertical spacing components such that $2\pi c$ is the distance between helical turns.

Pitch is analysed in the same fashion as tool length and rotation. For a fixed flow rate pressure drop is calculated through a coolant channel of 1mm in diameter spaced 3.3mm from the centre of the tool. The tool is 40mm in length with pitch varying between 20° and 40°. For this study the speed of rotation is fixed at 1,000rpm. Presented in Figure 4.5, the results show that as helix pitch increases the pressure required to drive the flow through the domain increases quadratically.

Figure 4.4: Definition of channel pitch.

The secondary y axis of Figure 4.5 is used to display the change in channel arc length as helix pitch changes. This shows that as pitch increases the arc length grows quadratically as a result of each helical turn becoming increasingly compact within the same length of tool. Further numerical calculations were carried out to examine the effect of pitch on the pressure drop by repeating the numerical calculations for a constrained channel arc length. This analysis is particularly interesting because tool length, speed of rotation, helix radius and arc length are also constrained and

Figure 4.5: Pressure drop calculation as a function of helical pitch in degrees.

only channel curvature and torsion are unconstrained. These results are presented in Figure 4.6 and 4.7.

The results in Figure 4.6 show pressure drop calculations in response to a change in pitch with constant arc length. The pressure drop is found to increase monotonically with pitch, but the gradient decreases with an increase of pitch. Figure 4.7 demonstrates the effect of a change in curvature and torsion with respect to helix pitch, and shows that increasing channel pitch increases channel curvature and reduces channel torsion. It is important to note that the profile of the curvature figure mirrors that of pressure drop. This strongly suggests that the increase in calculated pressure drop is a result of the increase in curvature. These results are consistent with previous work by Hüttl [Hüttl and Friedrich, 2000, Hüttl and Friedrich, 2001] which concluded that curvature has the greatest contribution to the pressure drop across helical flows. Torsion was found to influence the strength of the secondary flow and had a negligible effect on the mass flow of the system. It can be seen from the results in Figures 4.5, 4.6 and 4.7 that for a constant flow rate increasing channel helix pitch results in a quadratic increase in calculated pressure. This increase in pressure drop is the combined contribution of an increase in channel arc length and curvature.
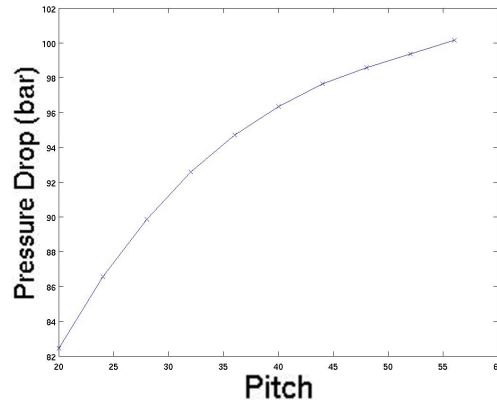
Figure 4.6: Pressure drop calculations as a function of helical pitch for a constant channel arc length

(a) Curvature
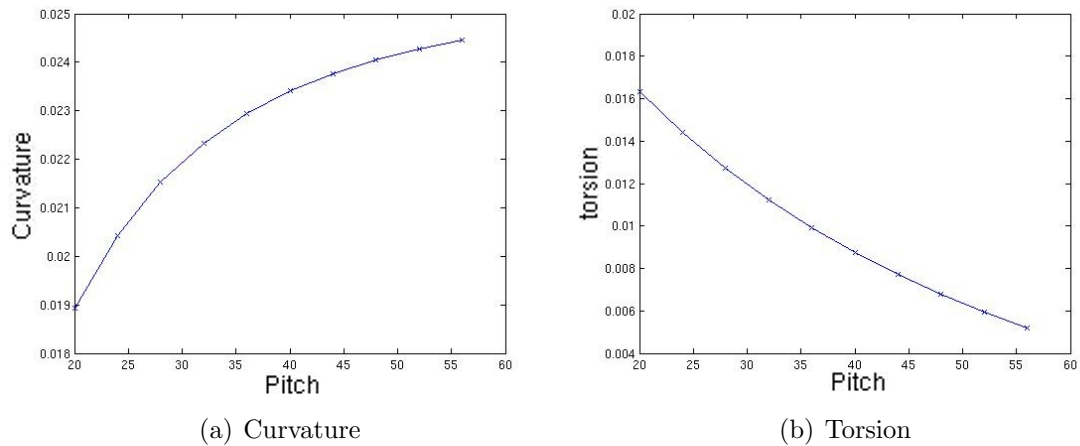
(b) Torsion

Figure 4.7: Curvature and torsion in response to the change in helix pitch.

4.2.4 Effect of Channel Spacing

Channel spacing is the distance between the centre of the coolant channel and the centre of the tool geometry, illustrated in Figure 4.8, and is the equivalent to the radius of the helix. Helix radius is used to define helix pitch angle $\theta = tan^{-1}(\frac{4r}{c})$ and the distance between helical turns is defined as $2\pi c$. There-
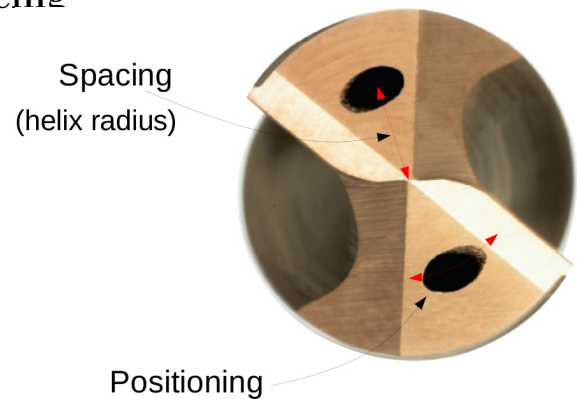
Figure 4.8: Definition of channel spacing, also referred to as helix radius.

fore constraining pitch angle and channel spacing will result in a change in distance between helical turns and the number of helical turns. In light of this, the study of channel spacing on the delivery of coolant consists of two major components:

- Channel spacing with constant helical turn spacing.

- Channel spacing with constant pitch angle.

Channel Spacing: Constant Helical Turn Spacing

In practise, for a coolant channel within a fixed tool geometry, the distance between helical turns and the number of helical turns remains constrained by the number of turns made by the tool geometry. For this reason the number of helical turns and the distance between coils is fixed for all geometries simulated in this section. The effects on the geometry are visualised in Figure 4.9 which display a set of helical centre lines each assuming different values of channel spacing.

Investigation results are presented in Figure 4.10 (Left) which shows calculated

(a)   (b)
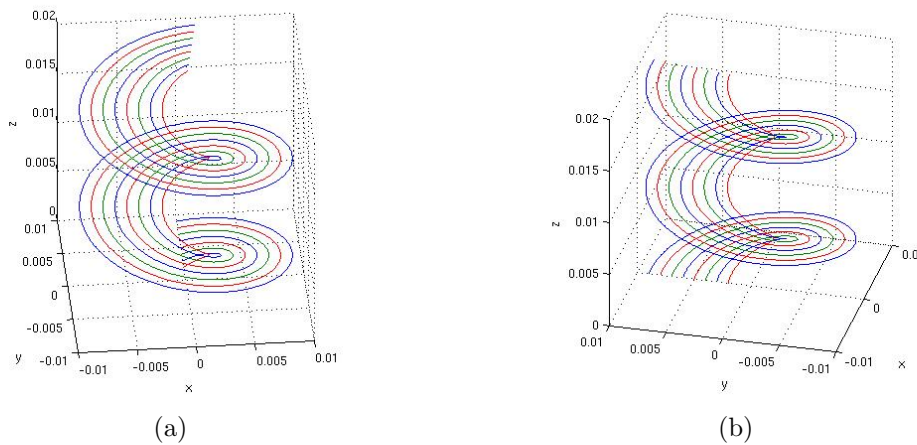
Figure 4.9: Helix centre line in response to a change in helix radius.

pressure drop as a function of helix radius, and shows a clear linear relationship between channel spacing and the calculated pressure drop. Figure 4.10 (Right) illustrates the change in channel arc length in response to a change in channel

(a) Calculated pressure drop
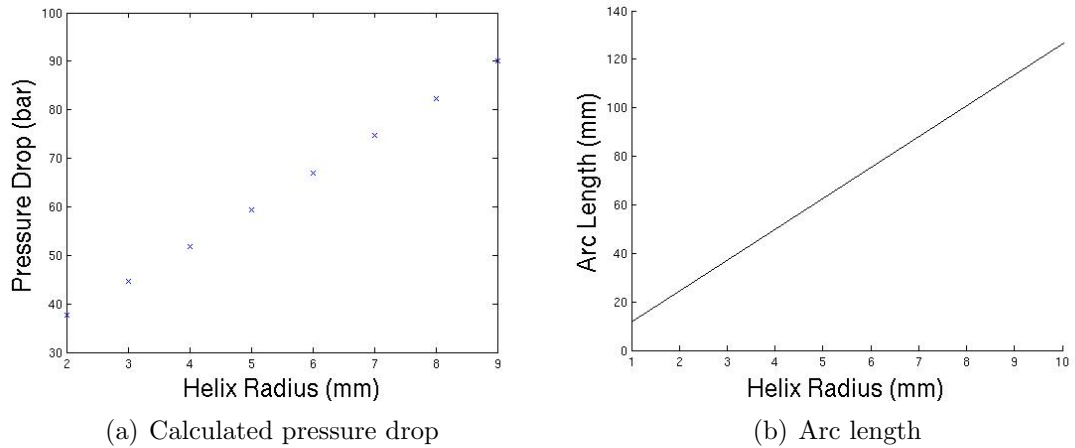
(b) Arc length

Figure 4.10: Calculated pressure drop and arc length as a function of helix radius.

spacing and it shows a linear relationship between arc length and channel spacing. Figure 4.11(Left) and (Right) show the change in channel torsion and curvature as the geometry changes with channel spacing. As the radius of the helix expands channel curvature increases and channel torsion decreases by a very small amount. Considering the change in curvature and torsion is very small it appears that the increase in pressure drop associated with an increase in channel spacing observed in Figure 4.9 (Left) is mostly caused by an increase in arc length.

(a) Torsion
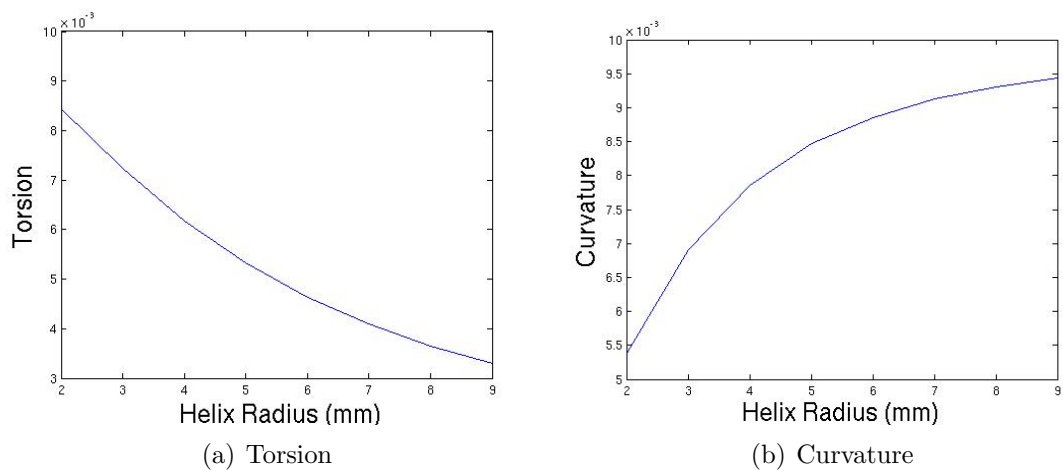
(b) Curvature

Figure 4.11: Change in torsion and curvature in response to the change in helix radius.

Channel Spacing: Constant Pitch Angle

This study sought to examine the effect of an increase in tool diameter on the calculated pressure drop for a specified tool flute angle. In this case as the tool's diameter expands, the number of turns the flute makes decreases. This is described using the expression for helical pitch, $\theta = tan^{-1}(\frac{4R}{c})$ where $2\pi c$ is the distance between helical turns. For this set of experiments helix pitch is constant and helix radius is varied and therefore a change in helix radius, R results in a change in c and the distance between helical turns in order. The diagram shown in Figure 4.12 illustrates this change using a side-on view of a helix where each tool has a fixed pitch and length. The diagram on the left displays a helix with a single turn, however if the diameter of tool increases the distance between helical turns increases and reduces the number of helical turns, this is shown in the central diagram. The diagram on the right overlays the other diagrams for comparison. When constraining
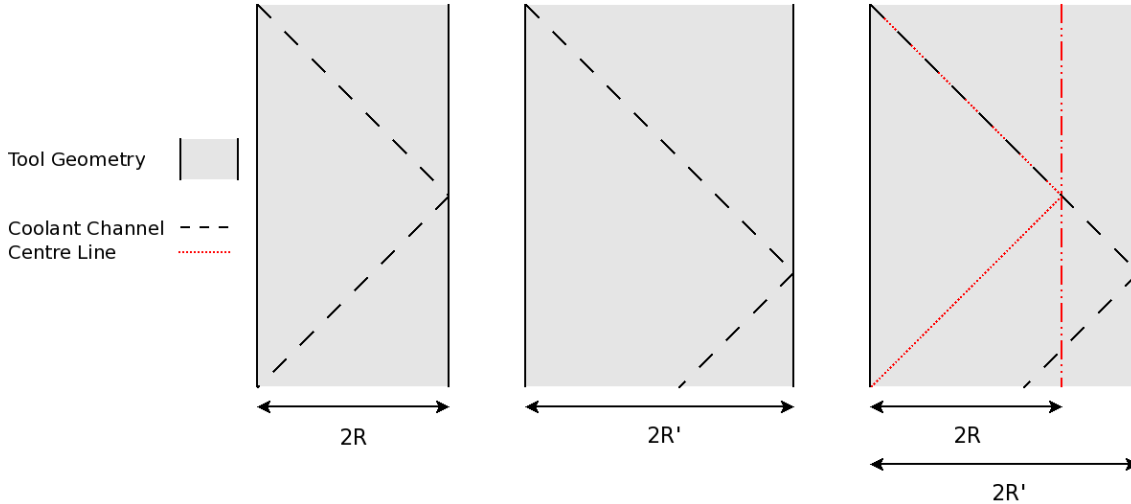
Figure 4.12: The effect of a change in radius for a constant pitch angle.

pitch, the curvature and torsion of the channel, κ, and τ, and arc length remains constant for all geometries. The geometry features which can assume other values are the distance between helical turns, the number of helical turns and the Dean number. The variation in the geometry is shown further in Figure 4.13 for a number

of helical centre lines each assuming different helix radius values. (Left) shows the helical centre lines from a top down perspective and (Right) in a 3D representation, these figures illustrate the large difference in number of helical turns between the helices of different size radii. Pressure drop calculations for this configuration are
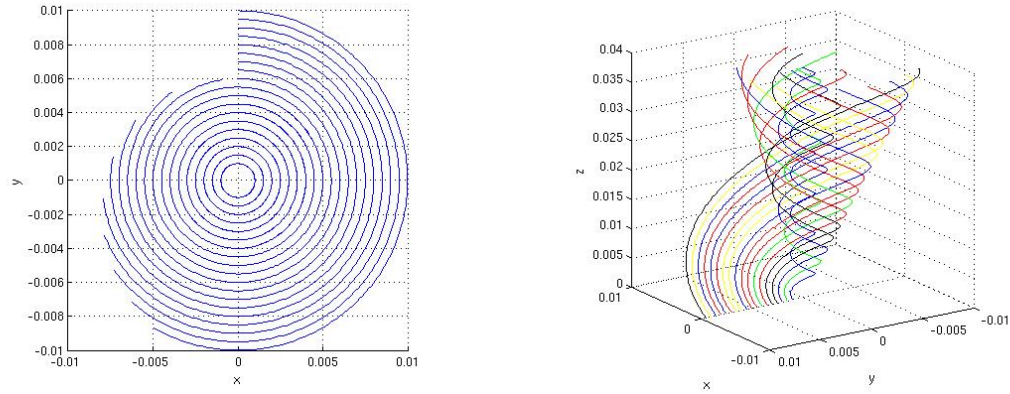
Figure 4.13: Change in helix centre line in response to a change in channel spacing with fixed helical pitch.

displayed in 4.14 (Left) for a fixed flow rate through coolant channels of 1mm in diameter for a tool of 40mm and 30° pitch. Channel spacings between 2mm and 9mm were simulated. These results show that for a constant channel pitch an increase in channel spacing (or helix radius) results in decrease in calculated pressure drop, however the rate of change of the calculated pressure decreases as channel spacing increases. (Right) shows the change in Dean number in response to the change in channel spacing, and it can be seen that for a fixed flow rate an increase in channel spacing results in a decrease in the Dean number with a profile that is similar to (Left). Figure 4.15 (Left) demonstrates the change in the distance between helical turns in response to modifications of channel spacing and shows a linear relationship between channel spacing and channel spacing. However, Figure 4.15 (Right) shows the change in number of helical turns as a function of channel spacing, which shows that the number of helical turns decreases and channel spacing increases and that the rate at which it decreases also decreases as channel spacing decreases. Helical

(a) Calculated pressure drop
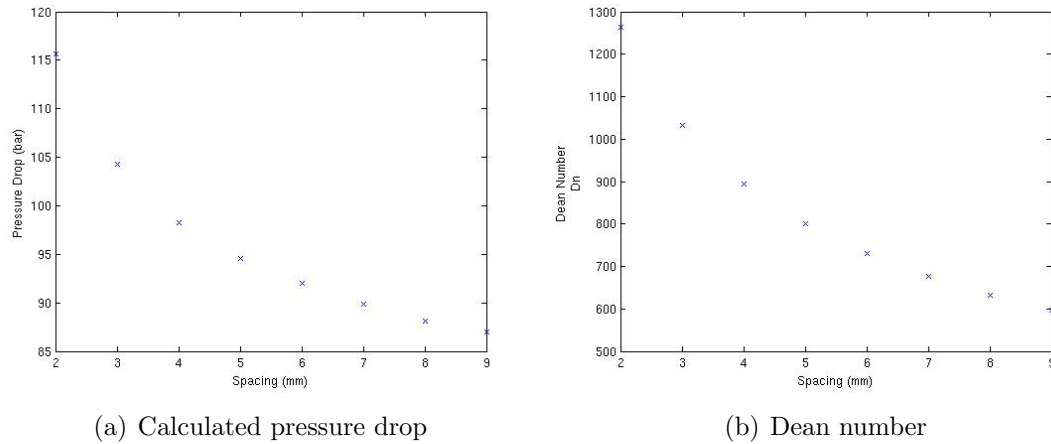
(b) Dean number

Figure 4.14: Calculated pressure and Dean number as a function of channel spacing

turns, Dean number in response to channel radius mirror the profile of pressure drop as a function of channel spacing. The decrease in Dean number suggests that as the channel spacing increases the bend of the helix expands which results in a reduction in centrifugal forces. It is not clear whether the decrease in calculated pressure drop is a result of the decrease in centrifugal forces, the number of helical turns or a combination of the two parameters.

4.3 Summary

The parametric study has highlighted the following relationships between each design parameter and the calculated pressure drop for constrained flow rates:

Length - Calculated pressure drop increases linearly with an increase in tool length.

Rotation - Calculated pressure drop increases linearly with speed of rotation.

Pitch - Pressure drop increases quadratically as pitch increases, this is caused mostly by an increase in arc length and secondly by an increase in channel curvature.

(a) Distance between helical turns (b) Number of helical turns
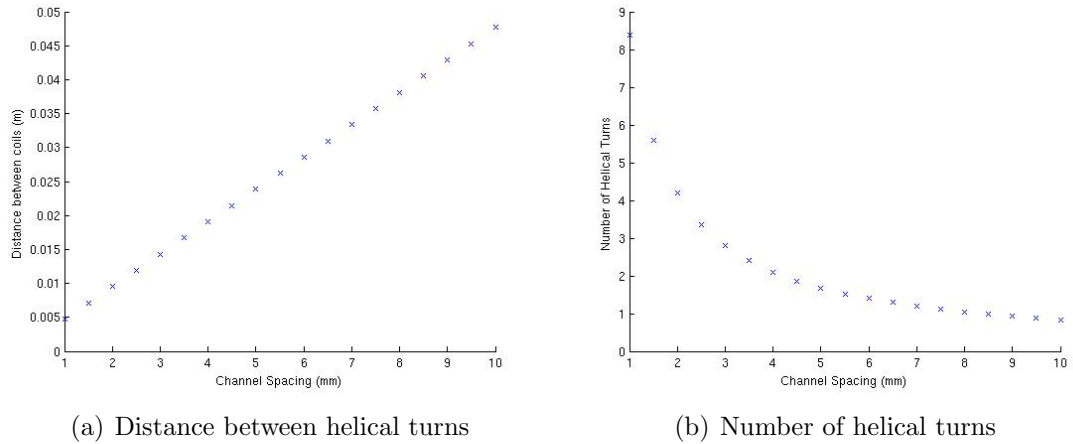
Figure 4.15: Change in the distance between helical turns and the number of helical turns in response to a change in channel spacing.

Spacing (Constant Helical Turn Spacing) - Calculated pressure drop increases linearly with channel spacing as a result of an increase in arc length and curvature.

Spacing (Constant Helical Pitch Angle) - Calculated pressure drop decreases with channel spacing, although it is unclear whether this is caused by the number of helical turns, the Dean number or a combination of the two.

4.4 Further Parametric study

The previous parameter study examines the effect when changing a single design parameter. The study of channel pitch and spacing found that a change in either design variable results in a change in curvature and torsion of the channel. The remainder of this chapter will outline Metamodelling techniques which are employed to examine the behaviour between multiple design parameters.

4.5   Metamodelling techniques

Metamodelling (also referred to as response surface modelling) was first introduced by Box and Wilson [Box and Wilson, 1951] and is most commonly used in optimisation problems. The purpose of a metamodel is to approximate system responses using function evaluations at selected points in the design space. Although not an optimisation technique itself, they are methods of increasing the speed of the optimisation process by reducing the number of experimental measurements, or in this case numerical evaluations. Design of Experiments is the name given to techniques used for guiding the choice of experiments to be performed in an efficient way to gain the maximum amount of information from minimal computational effort.

4.6   Design of Experiments

A key component of developing an accurate metamodel of a system's response to its input design variables is the use of an effective Design of Experiments (DoE). A DoE is a strategy for obtaining information from across the design space as efficiently as possible. Too much data leads to wasted processing time, however too few data points may lead to erroneous response predictions. An experiment is a series of tests in which the input variables are changed according to a given rule in order to investigate the reasons for changes in the output response [Cavazzuti, 2013].

In order to carry out a DoE it is necessary to select the design variables, which are often called factors or parameters. A design space, or region of interest, is defined as a range of variability which must be defined for each design variable. The term level is the number of values a variable can assume according to its discretisation. The objective function and the set of experiments to be performed are referred to as the response variables and sample space respectively.

The recent book by Cavazutti [Cavazzuti, 2013] gives a comprehensive overview of effective DOE techniques, however this introduction will examine the Full Factorial Design method and two space-filling techniques based on Latin Hypercube DOE methods.

4.6.1 Full Factorial Sampling

Full factorial sampling is one of the most common and intuitive strategies available for creating a DOE which specifies samples for every possible combination of factor values (i.e. design variables). In its simplest form, the two-level full factorial, if there are k-factors (i.e. design variables) and $L = 2$ for each factor the number samples is $N = 2^k$. The 2^k full factorial design can easily be extended to the general case where there are more than two factors and each of them have more than two levels. If there are k factors $x_1, ..., x_k$ each having $L_1, L_2, ..., L_k$ levels then the sample size of the full factorial design is:

$$N = \prod_{i=1}^{k} L_i \tag{4.1}$$

Full factorial designs make very efficient use of the data and enable the main and the interaction effects between factors to be identified clearly. An L_k full factorial design as L levels for each factor, k. A simple example of $2^2, 2^3$ and 3^3 full factorial designs is given in Figure 4.16. The family of L_k designs, where the number of levels is the same for each factor, is particularly suitable for interpolation by polynomial response surfaces, since a 2 dimensional design can be interpolated with a complete bi-linear form, a 3 dimensional design by a complete bi-quadratic form, and a 4 dimensional design with a complete bi-cubic form etc. This study will not outline all designs in depth, however there are other variants of the Full Factorial Design listed below, for a more in depth discussion the reader is directed towards [Montgomery, 2008].

- Fractional Factorial - As the number of factors increases, a full factorial design
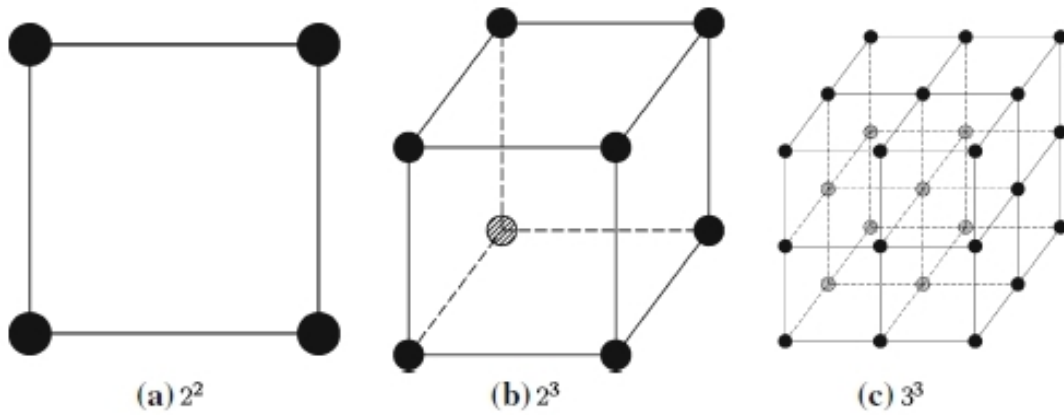
Figure 4.16: Simple $2^2.2^3$ and 3^3 full factorial designs [Cavazzuti, 2013].

becomes very expensive. The purpose of a fractional design is to perform only a subset of the full factorial experiments so that the main and interaction effects can still be determined.

- Central composite - A central composite design is a 2^k full factorial design to which the central point and star points are added. Examples of the central composite experimental designs Central Composite Circumscribed (CCC), Central Composite Inscribed (CCI) and Central Composite Face-centred design are given before
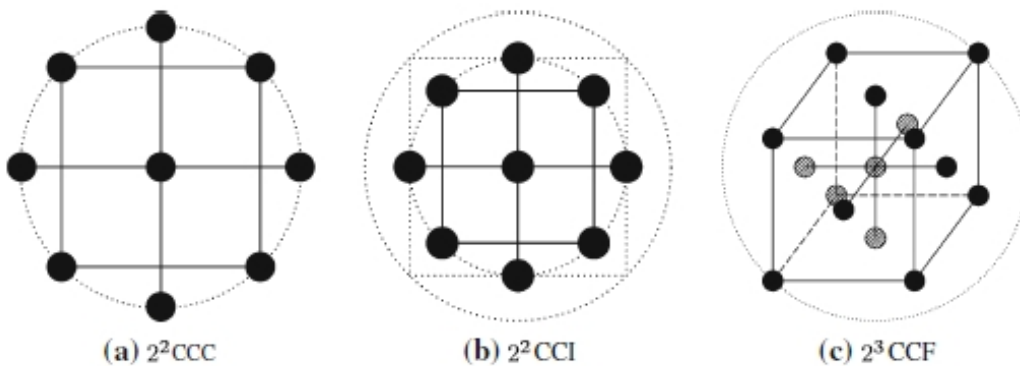
Figure 4.17: Examples of central composite designs [Cavazzuti, 2013].
.

4.6.2 Space-filling DOEs

Space-filling DOE techniques rely on different methods for uniformly filling the design space. Unlike the full factorial sampling method previously discussed, these methods are not based on the concept of levels, do not require discretised parameters and the sample size is chosen by the user independent of the number of parameters of the problem. Space-filling techniques are usually a good choice for metamodelling because for a given N, empty areas which are far from the sample and in which the interpolation may be inaccurate are unlikely to occur [Cavazzuti, 2013]. However, because space-filling techniques are not level-based it is not possible to evaluate the parameter's main effects and the interaction effects as easily as with factorial designs.

The most simplistic space filling approach is filling the design space with uniformly distributed, randomly created samples. However, this randomly generated DOE is not particularly efficient because the randomness of the method does not guarantee the sample distribution will not be clustered and therefore does not achieve the aim of a uniformly filled design space.

Latin Hypercube DOEs

Latin Hypercube DOEs are a type of space filling technique which subdivides the design space into an orthogonal grid with N elements per parameter, k. Within the multi-dimensional grid N sub-volumes are selected so that along each row and column only one sub-volume is chosen. This process is shown in Figure 4.18 where the chosen sub-volumes are black. Inside each sub-volume a sample is chosen at random. An example Latin Hypercube DOE is demonstrated in Figure 4.18 and displays two valid Latin Hyper designs, however the DOE on the left leaves most of the design space unexplored. The DOE on the right shows the resulting DOE after performing a correlation reduction of a Latin Hypercube. It is important to select

(a) $k = 2$, $N = 4$ (b) $k = 3$, $N = 3$
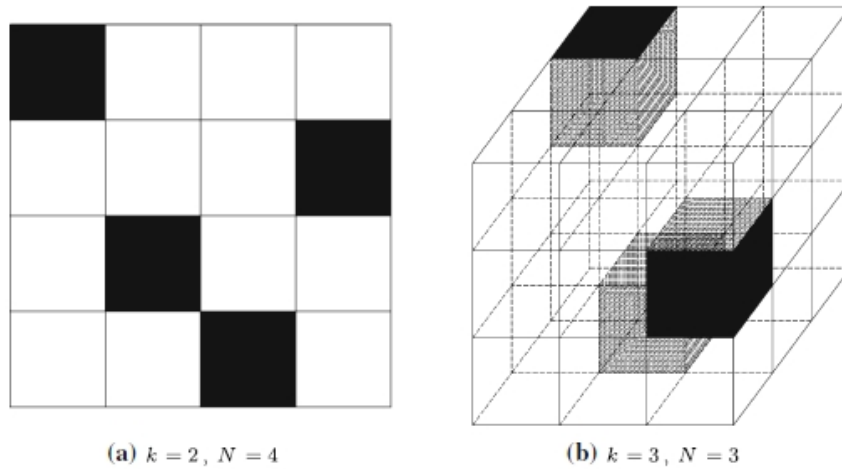
Figure 4.18: Latin hypercube sampling [Cavazzuti, 2013].

the sub-volumes which have no spurious correlations between dimensions and to distribute the samples all over the design space so that all response surface features are captured. For example, a set of samples along the diagonal of a design space
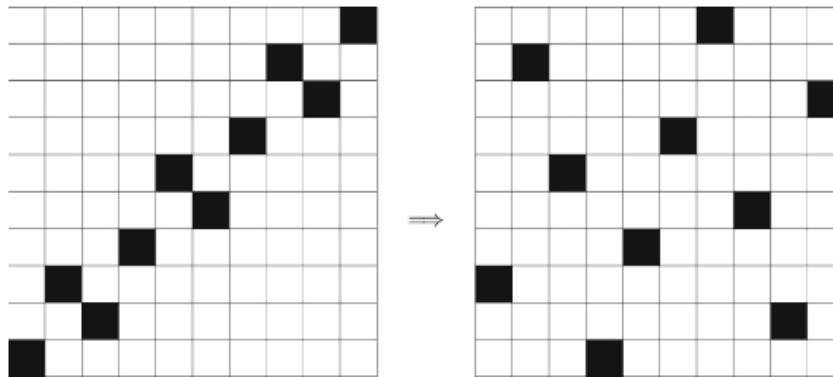
Figure 4.19: Latin hypercube sampling [Cavazzuti, 2013].

would satisfy the requirements of a Latin Hypercube DOE but would leave most of the design space unexplored. There are several techniques available to reduce the correlations in Latin Hypercube designs. An example is shown in Figure 4.19 which illustrates correlation reduction between variable values in a Latin Hypercube DOE with $k = 2$ factors and $N = 10$.

Optimal Latin Hypercube (OLHC) DOEs

Optimal Latin Hypercube (OLHC) designs are particularly useful when sample evaluation is time consuming because the fewest number of samples are used to populate the design space. Morris-Mitchell and the Audze-Eglais optimality criteria are two methods of producing an optimal Latin Hypercube. Morris Mitchell applied a series of randomly formed Latin Hypercubes to construct an Optimal Latin Hypercube based on a criterion which maximises the minimum distances between the points. The Morris-Mitchell optimality criterion is given formally by:

$$max(min(r_{p,q} : 1 \leq p \neq q \leq N))$$ (4.2)

The Audze-Eglais method is an alternative optimality criterion which distributes the points uniformly by minimising the reciprocal of the squared distances between all of the points. This is given by:

$$\sum_{p=1}^{N} \sum_{q=p+1}^{N} \frac{1}{r_{pq}^2}$$ (4.3)

The effects of the Morris-Mitchell and the Audze-Eglais correlation criterion are compared in Figures 4.20, 4.21 and 4.22 for a varying number of points. It can be seen from these results that the Morris-Mitchell correlation criterion creates sample distributions with some areas left with very few sample points in relation to other areas of the design space. The Audze-Eglais however creates a much more uniform distribution of sample points.

4.6.3   Model Construction

Metamodelling was first introduced by Box and Wilson [Box and Wilson, 1951], the purpose of a metamodel is to approximate the response of a system based on function values at select points throughout the domain. These techniques are ad-

(a) Morris-Mitchell

(b) Audze-Eglais

Figure 4.20: $k = 2$, $N = 20$

(a) Morris-Mitchell

(b) Audze-Eglais

Figure 4.21: $k = 2$, $N = 50$

(a) Morris-Mitchell

(b) Audze-Eglais
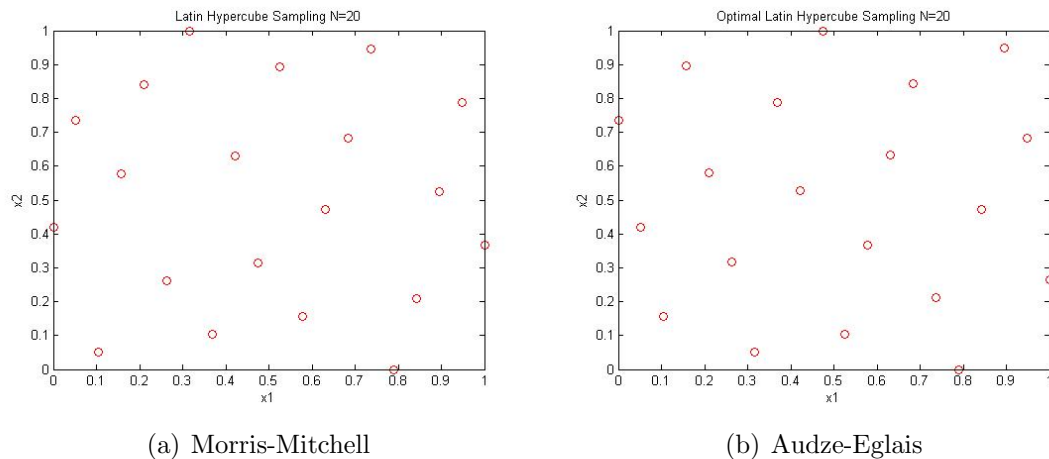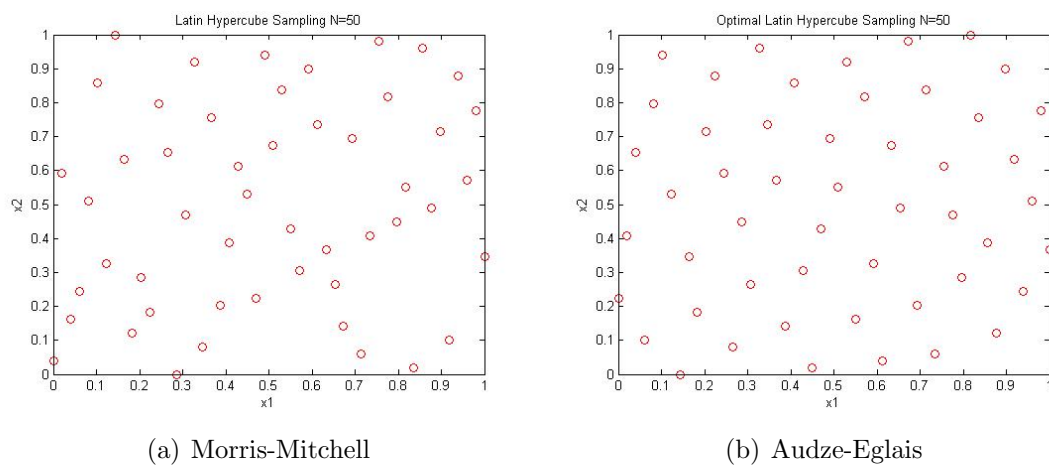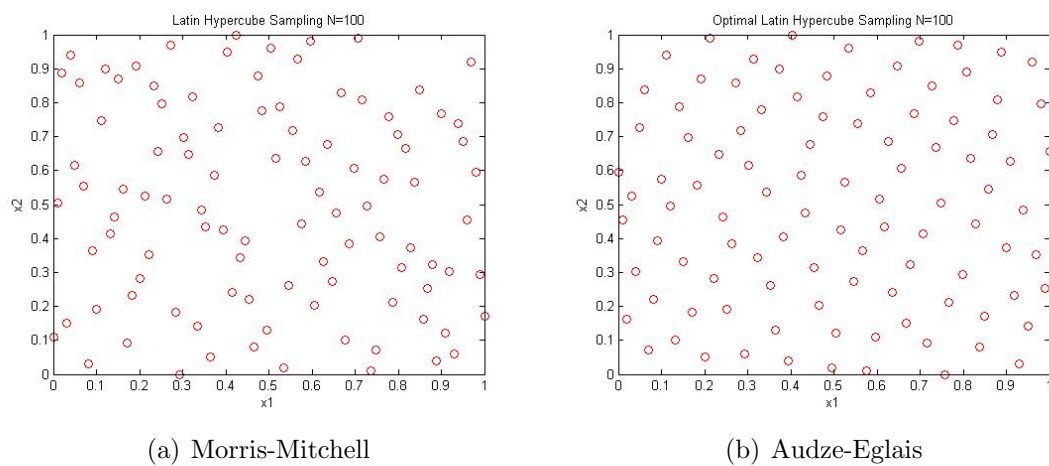
Figure 4.22: $k = 2, N = 100$ [Loweth et al., 2010]

vantageous for problems with a large design space or with time consuming sample evaluations because a good cross-section of designs located within the design space are represented using a minimal number of sample evaluations. Building the model is directly coupled with the Design of Experiments discussed previously because the selection of points and their evaluation determines the metamodel created. This section will now outline some of the most common metamodel methods.

Artificial Neural Networks (ANN)

Artificial Neural Networks (ANN) are information processing systems inspired by biological neural networks. These metamodels use a supervised learning paradigm to train the connections between neurons to minimise a cost function which measures the quality of fit for the DOE. These techniques are more suited towards machine learning rather than metamodelling [Cavazzuti, 2013].

Kriging Method

The Kriging method is a popular metamodelling technique for approximating system behaviour based on a discrete set of sample point evaluations. The fundamental idea of Kriging is to predict system responses at any given point based on a weighted average of known system responses in the neighbourhood of the location being evaluated. This technique is similar to the Moving Least Squares Method (MLSM), which will be discussed later, in that it also uses weight functions to control the amount of influence a sample point has on the interpolation point. However, the significant difference between Kriging and MLSM is that metamodel created will always intersect the data points used to create it, which is not the case for MLSM [Cavazzuti, 2013, Kim et al., 2009].

Radial Basis Functions(RBF)

A Radial basis function is a metamodelling technique which is a real-valued function whose value depends on its distance from a centre point c.

$$\psi(x, c) = \psi(\|x - c\|) \tag{4.4}$$

Given the output of a DoE (x_i, f_i), where $x_i = (x_{1,i}, ..., x_{ndv,i})$ are the design variables at the ith DOE point and f_i is the corresponding response at design x_i. A RBF metamodel takes the form:

$$\hat{f}(x) = \sum_{i=1}^{N} \lambda_i \psi(\|x - x_i\|) \tag{4.5}$$

The weights λ_i where $i = 1, ..., N$ are computed by solving the interpolation condition:

$$\mathbf{Wf} = \mathbf{y}$$

where λ is the weights vector, $\mathbf{f}$ is the vector of DOE responses and W is the Gram matrix given by:

$$W_{ij} = \psi(\|x - x_i\|)$$

The choice of basis function is particularly important to the performance to the RBF. Some common choices of basis function include linear, cubic, thin plate spline and Gaussian which are expressed as:

$$\psi(r) = r \tag{4.6}$$

$$\psi(r) = r^3 \tag{4.7}$$

$$\psi(r) = r^2 ln(r) \tag{4.8}$$

$$\psi(r) = exp(-\frac{r^2}{2\sigma^2}) \tag{4.9}$$

respectively, where r is the Euclidean distance between points. Radial Basis functions have been shown to produce accurate approximations when handling both noisy and smooth data [Forrester et al., 2008].

4.6.4 Least Squares

The Least Squares (LS) method is process of approximating the solution of an over determined system of equations. Given a DOE of n designs and their response f which are a function of ndv design variables $x_1, x_2, ..., x_{ndv}$, the least squares method aims for a polynomial fit of the data.

For example, a linear fit for three design variables, (x_1, x_2, x_3), would fit the data to a hyper-plane of the form $f = c_1 + c_2 x_1 + c_3 x_2 + c_4 x_3$. The goal is then to find the 4 regression coefficients c_1, c_2, c_3 and c_4. Standard regression analysis seeks to minimise the sum of the squares of the differences (Squares Errors, SE) between the data points and the fitted curve. For this example it is given by:

$$SE = \sum_{i=1}^{N} (f_i - c_1 - c_2 x_{1,1} - c_3 x_{2,i} - c_3 x_{2,i} - c_4 x_{3,i})^2 \qquad (4.10)$$

where f_i is the response at the ith sampling point $(x_{1,i}, x_{2,i}, x_{3,i})$. To find the regression coefficients c_i which minimise the SE the following needs to be satisfied:

$$\frac{\partial SE}{\partial c_1} = -2 \sum_{i=1}^{n} (f_i - c_1 - c_2 x_{1,i} - c_3 x_{2,i} - c_3 x_{2,i} - c_4 x_{3,i}) = 0$$

$$\frac{\partial SE}{\partial c_2} = -2 \sum_{i=1}^{n} (f_i - c_1 - c_2 x_{1,i} - c_3 x_{2,i} - c_3 x_{2,i} - c_4 x_{3,i}) x_{1,i} = 0$$

$$\frac{\partial SE}{\partial c_3} = -2 \sum_{i=1}^{n} (f_i - c_1 - c_2 x_{1,i} - c_3 x_{2,i} - c_3 x_{2,i} - c_4 x_{3,i}) x_{2,i} = 0$$

$$\frac{\partial SE}{\partial c_4} = -2 \sum_{i=1}^{n} (f_i - c_1 - c_2 x_{1,i} - c_3 x_{2,i} - c_3 x_{2,i} - c_4 x_{3,i}) x_{3,i} = 0$$

This leads to a linear system of four regression equations:

$$xc_1 + c_2 \sum_{i=1}^{n} +x_{1,i} + c_3 \sum_{i=1}^{n} +x_{2,i} + c_4 \sum_{i=1}^{n} +x_{3,i} = \sum_{i=1}^{n} f_i$$

$$c_1 \sum_{i=1}^{n} x_{1,i} + c_2 \sum_{i=1}^{n} x_{1,i}^2 + c_3 \sum_{i=1}^{n} x_{1,i}x_{2,i} + c_4 \sum_{i=1}^{n} x_{1,i}x_{3,i} = \sum_{i=1}^{n} f_i x_{1,i}$$

$$c_1 \sum_{i=1}^{n} x_{2,i} + c_2 \sum_{i=1}^{n} x_{1,i}x_{2,i} + c_3 \sum_{i=1}^{n} x_{2,i}^2 + c_4 \sum_{i=1}^{n} x_{2,i}x_{3,i} = \sum_{i=1}^{n} f_i x_{2,i}$$

$$c_1 \sum_{i=1}^{n} x_{3,i} + c_2 \sum_{i=1}^{n} x_{1,i}x_{3,i} + c_3 \sum_{i=1}^{n} x_{2,i}x_{3,i} + c_4 \sum_{i=1}^{n} x_{3,i}^2 = \sum_{i=1}^{n} f_i x_{3,i}$$

These equations are then solved to obtain the regression coefficients c_1, c_2, c_3 and c_4 which lead to the metamodel:

$$f = c_1 + c_2 x_1 + c_3 x_2 + c_4 x_3 \qquad (4.11)$$

4.6.5 Moving Least Squares Method (MLSM)

The conventional least squares method outlined in the previous section can be generalised to the Moving Least Squares Method [Bates et al., 2004]. MLSM is a generalised weighted least squares method where the contribution of a point is dependent on its distance from the point being evaluated by the metamodel, this is referred to as its weight. Weights are functions of the Euclidean distance, r_k, from the kth sampling point to the point being evaluated by the metamodel.

The weight w_i associated with sample point x_i decays as the distance from this point increases. Because the weights w_i are functions of x, the polynomial basis function coefficients are also dependent on x.

$$min\ G(\mathbf{c}(\mathbf{x})) = \sum_{i=1}^{n} w_i(\mathbf{x})[f(\mathbf{x}_i - \tilde{f}(\mathbf{x}_i, \mathbf{c})]^2 \qquad (4.12)$$

This means that it is not possible to obtain an analytical form of the approximation function but its evaluation is still computationally inexpensive. Therefore we estimate a function, f, at an arbitrary point $\{x\} = \{x_1, ..., x_{ndv}\}$ based on the values at a series of sampling points $\{f_i\} = \{f_1, ...f_n\}$ at a series of design points $\{x_{1,i}, ..., x_{ndv,i}\}$. One such approach is to create an estimate using:

$$\hat{f}(x) = \sum_{i=1}^{n} w_i(\|x - x_i\|) f_i \tag{4.13}$$

where $r_i = \|x - x_i\|$ is the Euclidean norm. Therefore the estimate to the response function would take the form of:

$$\hat{y}(x) = \sum_{i=1}^{n} w_i(r_i) f_i \tag{4.14}$$

where w_i are weight decay functions of parameter r_i.

The closeness of fit parameter enables the modification of the weight decay function so that samples located far from the point being evaluated can have more or less of a contribution towards the approximated value. This feature enables handling of the issue of numerical noise by setting a tight fit for noiseless data or changing it to a loose fit when the response exhibits a considerable amount of numerical noise. The Gaussian weight decay function is a popular choice:

$$w_i = e^{-\theta r_i^2} \tag{4.15}$$

where r_i is the normalised distance from the ith sampling point to the current point being approximated and θ is the closeness of fit parameter. The effect of θ on the weight function is demonstrated in Figure 4.23. For $\theta = 0$ the method is reduced to traditional least squares method.
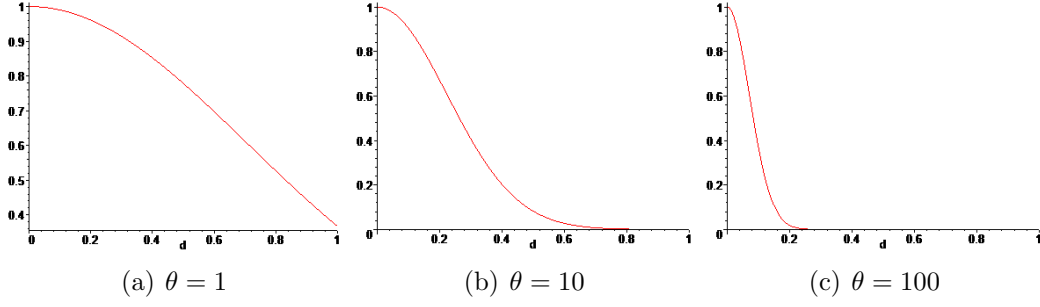
Figure 4.23: Gaussian weight decay functions [Loweth et al., 2010]

Example of MLSM with 2 design variables

For Second order regression with two variables the MLS regression coefficients c_1, c_2, c_3, c_4, c_5 and c_6 at the output point $\{x_j\} = \{x_{1,j}, x_{2,j}\}$ are obtained by minimising the sum of the least squares, SE_j, over all the sampling points $(x_{1,i}, x_{2,i})$ defined by:

$$SE = \sum_{i=1}^{N} w_{ij}(f_i - c_1 - c_2 x_{1,1} - c_3 x_{2,i} - c_4 x_{1^2,i} - c_5 x_{1,i} x_{2,i} - c_6 x_{2,i}^2)^2 \qquad (4.16)$$

Where w_{ij} is the weight decay function between output point j and sample point i. The MLS coefficients are obtained by requiring that:

$$\frac{\partial SE_j}{\partial c_1} = \frac{\partial SE_j}{\partial c_2} = \frac{\partial SE_j}{\partial c_3} = \frac{\partial SE_j}{\partial c_4} = \frac{\partial SE_j}{\partial c_5} = \frac{\partial SE_j}{\partial c_6} = 0$$

$$\frac{\partial SE}{\partial c_1} = \sum_{i=1}^{n} -2W_{ij}(f_i - c_1 - c_2 x_{1,i} - c_3 x_{2,i} - c_4 x_{1,i}^2 - c_5 x_{1,i} x_{2,i} - c_6 x_{2,i}^2) = 0$$

$$\frac{\partial SE}{\partial c_2} = \sum_{i=1}^{n} -2W_{ij} x_{1,i}(f_i - c_1 - c_2 x_{1,i} - c_3 x_{2,i} - c_4 x_{1,i}^2 - c_5 x_{1,i} x_{2,i} - c_6 x_{2,i}^2) = 0$$

$$\frac{\partial SE}{\partial c_3} = \sum_{i=1}^{n} -2W_{ij} x_{2,i}(f_i - c_1 - c_2 x_{1,i} - c_3 x_{2,i} - c_4 x_{1,i}^2 - c_5 x_{1,i} x_{2,i} - c_6 x_{2,i}^2) = 0$$

$$\frac{\partial SE}{\partial c_4} = \sum_{i=1}^{n} -2W_{ij} x_{1,i}^2(f_i - c_1 - c_2 x_{1,i} - c_3 x_{2,i} - c_4 x_{1,i}^2 - c_5 x_{1,i} x_{2,i} - c_6 x_{2,i}^2) = 0$$

$$\frac{\partial SE}{\partial c_5} = \sum_{i=1}^{n} -2W_{ij}x_{1,i}x_{2,i}(f_i - c_1 - c_2 x_{1,i} - c_3 x_{2,i} - c_4 x_{1,i}^2 - c_5 x_{1,i}x_{2,i} - c_6 x_{2,i}^2) = 0$$

$$\frac{\partial SE}{\partial c_6} = \sum_{i=1}^{n} -2W_{ij}x_{2,i}^2(f_i - c_1 - c_2 x_{1,i} - c_3 x_{2,i} - c_4 x_{1,i}^2 - c_5 x_{1,i}x_{2,i} - c_6 x_{2,i}^2) = 0$$

The equations are then solved for c_1, c_2, c_3, c_4, c_5 and c_6 and obtain the MLSM approximation for f, at point $\{x_j\} = \{x_{1,j}, x_{2,j}\}$:

$$\hat{f}(x_j) = c_1 + c_2 x_{1,j} + c_3 x_{2,j} + c_4 x_{1,j}^2 + c_5 x_{1,j}x_{2,j} + c_6 x_{2,j}^2 \tag{4.17}$$

For higher order regression the number of regression coefficients increases rapidly. For example with two design variables $\{x_j\} = \{x_1, x_2\}$ the third order MLSM builds an approximation in the form:

$$\hat{f}(x_j) = c_1 + c_2 x_{1,j} + c_3 x_{2,j} + c_4 x_{1,j}^2 + c_5 x_{1,j}x_{2,j} + c_6 x_{2,j}^2 + c_7 x_{1,j}^3 + c_8 x_{1,j}^2 x_{2,j} + c_9 x_{1,j}x_{2,j}^2 + c_{10}x_{2,j}^3$$

$$\tag{4.18}$$

at the output point $\{x_j\} = \{x_{1,j}, x_{2,j}\}$. $c_1 - c_{10}$ are determined by minimising SE, summed over all n sampling points $(x_{1,i}, x_{2,i})$ such that

$$SE_j = \sum_{i=1}^{n} w_{ij}(f_i - c_1 - c_2 x_{1,i} - c_3 x_{2,i} - c_4 x_{1,i}^2 - c_5 x_{1,i}x_{2,i} -$$

$$c_6 x_{2,i}^2 - c_7 x_{1,i}^3 - c_8 x_{1,i}^2 - c_9 x_{1,i}x_{2,i}^2 - c_{10}x_{2,i}^3)^2 \tag{4.19}$$

4.6.6 Model Tuning

In order to obtain the best fit approximation it is important to optimise the closeness of fit parameter, θ. The best value can be found my minimising the error between the metamodel prediction and the response data at the DOE points. There are many statistical measures for error such as:

- Root Mean Squared Error (RMSE):

$$RMSE = \sqrt{\frac{1}{n}\sum_{i=1}^{n}(\hat{f} - f_i)^2} \tag{4.20}$$

where n is the number of measurements, $\hat{f}_i$ is the predicted value and f_i is the actual value.

- R^2 value:

$$R^2 = 1 - \frac{\sum_{i=1}^{n}(\hat{f}_i - f_i)^2}{\sum_{i=1}^{n}(f_i - \bar{f}_i)^2} \tag{4.21}$$

where $\bar{f}$ is the mean of the observed values.

- Relative Average Absolute Error (RAAE):

$$RAAE = \frac{\sum_{i=1}^{n}|\hat{f}_i - f_i|}{n\sigma} \tag{4.22}$$

where σ is the standard deviation of the observed values.

- Relative Maximum Absolute Error (RMAE):

$$RMAE = \frac{max\{|\hat{f}_1 - f_1|, |\hat{f}_2 - f_2|, ..., |\hat{f}_n - f_n|\}}{\sigma} \tag{4.23}$$

As the accuracy of the metamodel improves, the values of RMSE, RAAE and RMAE decrease, whereas R^2 tends to 1. It is necessary to evaluate the error between the experimental response data and the approximation to optimise the closeness of fit parameter, θ. This can be achieved in a number of ways such as using a **nested DOE**, **Leave-One-Out Cross Validation** and the $K-$fold Method.

4.6.7 Nested DOEs

This approach makes use of two independent DOEs and their corresponding response data. One DOE is used for the construction of the metamodel while the second DOE is used to evaluate the performance of the metamodel for a given value of θ. This is repeated in an optimisation loop until the value of θ is found which minimises the error. After obtaining the optimal value of θ the metamodel is reconstructed using a merged DOE of the two data-sets.

4.6.8 Leave-One-Out Cross Validation

Leave-One-Out Cross Validation (LOOCV) is an iterative method which removes a single point from the sample set, builds the metamodel using the remaining sample points and then finally calculates the error between the approximated and actual response at the removed point. This process is repeated for each point in the DOE and the total value of the error is minimised to find the optimal value of θ. For LOOCV it is common to use the Predicted Residual Sum of Squares (PRESS) error between the true data and the metamodel for the optimisation. PRESS is given by:

$$PRESS = \sum_{i=1}^{n} (\hat{f} - f_i)^2 \tag{4.24}$$

4.6.9 K-Fold Cross-Validation

This approach is similar to LOOCV, which rather than remove a single point for validation, a random subset of k points are removed and the remaining points are used to construct the metamodel for a given closeness of fit value, θ.

The error is calculated between the approximate and actual values located at each of the k validation points. This method is then used within an optimisation loop to optimise the closeness of fit parameter to minimise error.

4.7 Internal Coolant Channel Metamodel

Before creating the metamodel, it is first important to identify the design variables to be modelled. As pressure drop increases linearly with tool length, the optimisation of this parameter will lead to all tools having minimal length which is not practical for most drilling situations. Rotation is also neglected from this study because it is seen to influence the performance of the cooling channel by less than 1%. Pitch and spacing are a particularly interesting pair of parameters to examine concurrently because each parameter effects the curvature, torsion and arc length, therefore these will be the parameters used for the metamodel.

An Optimum Latin Hypercube was created using the Audze-Eglais optimality criterion by implementing a permutation genetic algorithm based on the work by [Bates et al., 2004]. This technique was used to create an optimally spaced data-set of 50, 200 and 400 points. A metamodel was created using a Moving Least Squares approximation between sample points and a bisection search combined with k-fold cross validation was used to find the closeness of fit parameter which minimises root mean squared error. A value of $k = 13$ was used based on practical experience as it was suitably large enough to evaluate the model accuracy without affecting model accuracy [Loweth et al., 2010]. The surfaces generated using this approach for 50 and 400 points are presented in Figure 4.24.

The response surface created using 50 points in Figure 4.24 (Left) captures the profile generated from the finer data-set of 400 points, however it contains a local minimum which does not exist in the more detailed data-set. When validating the model in Figure 4.24 (Right) the root mean squared error is 8×10^{-2}

For large degrees of pitch an increase in radial spacing can be seen to have a signifi-

(a) 50 points   (b) 400 points

Figure 4.24: Pressure response surface as a for a constant flow rate function of pitch and helix radius for a constant drill length of 40mm and constant rotations per minute, 1,000.

cant effect on reducing pressure drop. At small values of pitch an increase of radial spacing still decreases the pressure drop although the gradient is not as significant as at large pitch angles. For small spacing, an increase in pitch results in a steep increase pressure drop, however at large spacings changing the gradient is considerably smaller. It can be seen from this surface that the designs which minimise the pressure drop are located at the edge of the design space where pitch is minimised and spacing is maximised.

Surface generation was repeated to analyse the effect of helix pitch and radius on pressure drop for a constant arc length. The response surface is shown in Figure 4.25 and it is clear for small values of pitch spacing, as the radial spacing increases the pressure drop decreases. This relationship is mirrored at large values of pitch, however the gradient of descent is much steeper. For small radial spacing an increase in pitch results in a linear increase in pressure drop, a linear relationship can also be seen at large channel spacing values, however the gradient is smaller. The global optimum of this surface resides along the extremities of the surface with minimised pitch and maximised radial spacing.
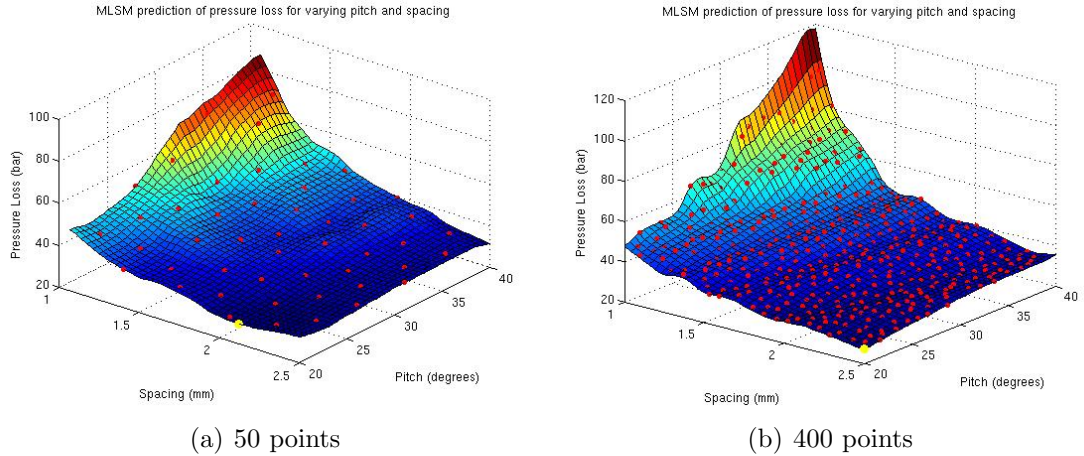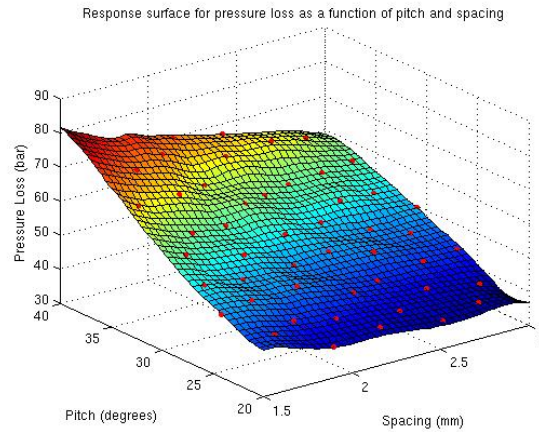
Figure 4.25: Pressure response surface as a function of pitch and helix radius for a constant drill length of 40mm

4.8 Discussion

This chapter has detailed a parametric study of internal coolant channel flow which examines the effect of tool length, speed of rotation, channel pitch and channel spacing. Tool length is shown to have a linear relationship with calculated pressure drop. An increase in pitch was found to increase pressure drop across the system quadratically, further numerical analysis for constrained channel arc length suggests the increase in pressure drop is caused by an increase in arc length and channel curvature. The study of channel pitch also observed the effects of curvature mentioned in Hüttl's work on helical channels [Hüttl and Friedrich, 2000, Hüttl and Friedrich, 2001]. It has been shown that drill coolant channel flow has a small dependence on angular velocity, which is in agreement with the Rossby number and the work of Yamamoto [Yamamoto et al., 2000]. Channel spacing for a constant distance between helical turns is found to increase the calculated pressure drop linearly mostly due to an increase in arc length and partly due to a small increase in curvature. Analysis of channel spacing with constant channel pitch found an increase in channel spacing

to reduce the calculated pressure drop. The gradient of change approaches tends toward zero as the channel spacing increases.

This chapter has included an overview of Design of Experiments methods, meta-modelling techniques and model tuning which was applied to creating a metamodel. The metamodel surfaces generated in 4.7 allow the examination of two parameters simultaneously where the resulting relationship between pitch and radial spacing would not otherwise be inferred using typical 2 dimensional analysis. Response surface analysis shows that when spacing is adequately large, in this case over 1.5mm from the centre of the drill, pitch has a considerably smaller influence on pressure drop. Finally, the analysis showed that maximising radial spacing and minimising pitch angle minimises the pressure drop for through-tool coolant flow.

Chapter 5

Coolant Exit Flow

5.1   Introduction

Section 3.2 outlined the structure of the numerical model, where the model is separated into two components as illustrated in Figure 5.1: through-tool flow and coolant exit flow. The model implemented for through-tool coolant flow examines coolant flow through the internal region of the tool and is described in Chapters 2 and 3. This through-tool flow model provides boundary conditions for the secondary model of coolant exit flow, which is the focal point of this chapter. The secondary model of
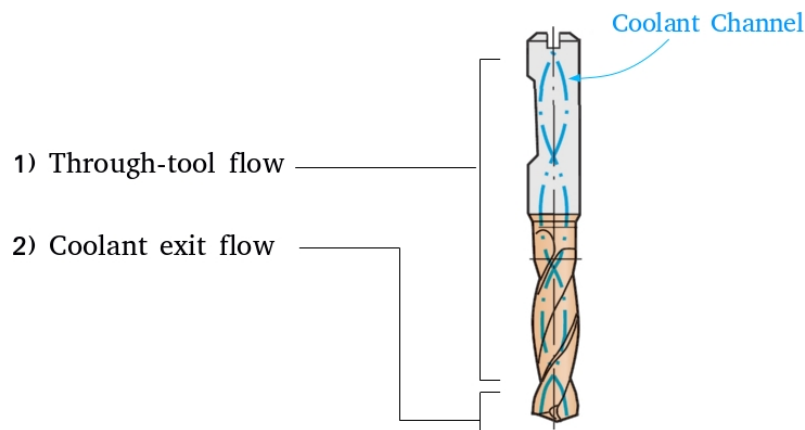

Figure 5.1: Problem domain decomposition

coolant exit flow is subject to complexities which are not encountered in the single

phase model of through-tool flow. At the point where coolant exits the tool the flow problem transforms from a single phase problem into a multiphase problem, therefore the interaction between the coolant and the air must be considered in addition to other highly complex modelling challenges localised at the cutting zone: the dynamic wetting of the tool, workpiece deformation, chip evacuation, heat transfer between the tool, coolant, workpiece and air. Before addressing some of the more complex physical phenomena encountered at the cutting zone, this work will first focus on modelling the multiphase flow of coolant. This chapter will begin with an overview of multiphase flows and appropriate modelling methodologies before providing an in-depth description of the numerical model used that includes the numerical description, solution procedure and mesh generation. This chapter will then close with the validation of the numerical model.

5.2   Multiphase flows

The term multiphase is used to refer to a fluid flow consisting of more than one phase or component [Crowe, 2005]. This term refers to a large number of different multiphase flow phenomena which encompass many different engineering applications, such as jet flow, gas bubbles, liquid droplets in a gas, solid particles in a gas or liquid etc. Figure 5.2 gives a more detailed list of different two-phase flow regimes according to [Ishii, 1975]. Each multiphase flow regime is classified into one of three general topologies: disperse, transitional (or mixed) and separated flows [Brennen, 2005, Bergles et al., 1981, Crowe, 2005, Hestroni, 1982, Ishii, 1975].

Separated flows are flows which contain continuous streams of different fluids which are separated by interfaces. These flow problems present fewer modelling challenges than disperse flows and can be modelled using single phase fluid flow equations for each stream coupled via appropriate kinematic and dynamic condi-
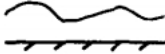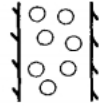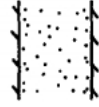
Class	Typical regimes	Geometry	Configuration	Examples
Separated flows	Film flow		Liquid film in gas Gas film in liquid	Film cooling Film boiling
	Annular flow		Liquid core and gas film Gas core and liquid film	Film boiling Condensors
	Jet flow		Liquid jet in gas Gas jet in liquid	Atomization Jet condensor
Mixed or transitional flows	Slug or plug flow		Gas pocket in liquid	Sodium boiling in forced convection
	Bubbly annular flow		Gas bubbles in liquid Film with gas core	Evaporators with wall nucleation
	Droplet annular flow		Gas core with droplets and liquid film	Steam generator
	Bubbly droplet annular flow		Gas core with droplets and liquid film with gas bubbles	Boiling nuclear reactor channel
Dispersed flows	Bubbly flow		Gas bubbles in liquid	Chemical reactors
	Droplet flow		Liquid droplets in gas	Spray cooling
	Particulate flow		Solid particles in gas or liquid	Transportation of wheat

Figure 5.2: Different two-phase flow regimes according to [Ishii, 1975]

tions specified at the interface. For further information the reader is directed towards the literature [Birkhoff and Zarantonello, 1987, Tulin, 1964] who successfully implemented these strategies.

Disperse flows consist of a finite number of particles, droplets or bubbles, which are distributed throughout a volume of a continuous phase and are common in chem-

ical reactors and spray cooling systems. In modelling disperse flows two types of model are prevalent: trajectory models and two-fluid models. This chapter will first describe preliminary experimental work before outlining disperse flows, separated flows and relevant modelling approaches [Crowe et al., 2011].

5.2.1 Trajectory Models

Trajectory models, also referred to as Euler-Lagrange models, are centred around the assumption that one phase is completely dispersed amongst another fluid phase; One phase is therefore referred to as the continuous phase and the other is the dispersed phase. The continuous phase is modelled using an Eulerian formulation and the dispersed phase uses a Lagrangian formulation. The dispersed phase is modelled by a discrete formulation, which represents each particle in the dispersed phase as an individual Disperse Phase Element (DPE). Therefore the equation of motion for a DPE is the conservation equation of momentum expressed in the Lagrangian formulation, where the dependent variables are the properties of the material particles [Rusche, 2003, Crowe et al., 2011]. For the continuous phase, the conservation equations are expressed in an Eulerian frame, where the fluid properties are represented as a continuum. An example of a trajectory based model is given in Figure 5.3
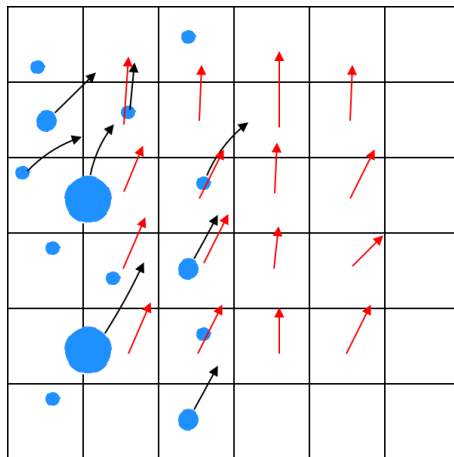
Figure 5.3: Example trajectory model

where the disperse phase particles are given in blue and the particle velocity vector is marked in black. The continuous phase is represented by the fixed grid and the velocity vectors of the continuous phase are denoted at the control volume centres in red.

An important advantage of trajectory models arises from their ability to store properties of the dispersed phase such as the size, shape and rotational speed for each individual dispersed phase element. The effects of each of these properties on fluid flow are accounted for in the equation of motion for each DPE. This arrangement makes it easier to calculate the distribution of properties throughout the system, which makes trajectory models suitable for problems which require property distributions such as droplet evaporation in combustion engines [Rusche, 2003].

For sufficiently dilute suspensions, where the particle size is small, the influence of the disperse phase on the motion of the continuous phase can be neglected because the flow is dominated by the continuous phase. This is described as one-way coupling between the phases. However, the model described encounters difficulties when the motions of the continuous and the dispersed phases are closely coupled because it can be unclear how much the disperse phase influences the motion of the continuous phase. Two-way coupling can be taken into account by accounting for the influence of the dispersed phase in the momentum equation and the turbulence model of the continuous phase [Brennen, 2005, Rusche, 2003]. Further difficulties for trajectory models emerge when the phase fraction of the dispersed phase is high. This is because the computational effort required for the dispersed phase is proportional to the number of phase elements, as each DPE requires a solution to its own equation of motion. However, in some cases this problem can be overcome by calculating the motion of a finite number of computational parcels where each parcel contains DPEs which possess the same characteristics such as size, shape, etc. It

has also been found that the number of DPEs in a parcel may have an influence on the results [Elghobashi, 1994, Kralj, 1996, Rusche, 2003]

5.2.2 The Two-Fluid Model

The two-fluid model, also known as the Euler-Euler model, represents both phases as a continuum which interpenetrate and interact with one another. In a two-fluid model averaged conservation equations are used for mass, momentum and energy to model each phase, and additional terms are included to account for the interaction between the phases. These additional terms account for the transfer of momentum and energy between phases [Rusche, 2003]. However, as a result of adopting an Eulerian structure the properties of the disperse phase are averaged over the continuum, which gives rise to the term α in the conservation equations. α defines the probability that a certain phase is present at a specific point in space or time [Hill, 1998]. Figure 5.4 illustrates the two-fluid model. This example has two phases, a
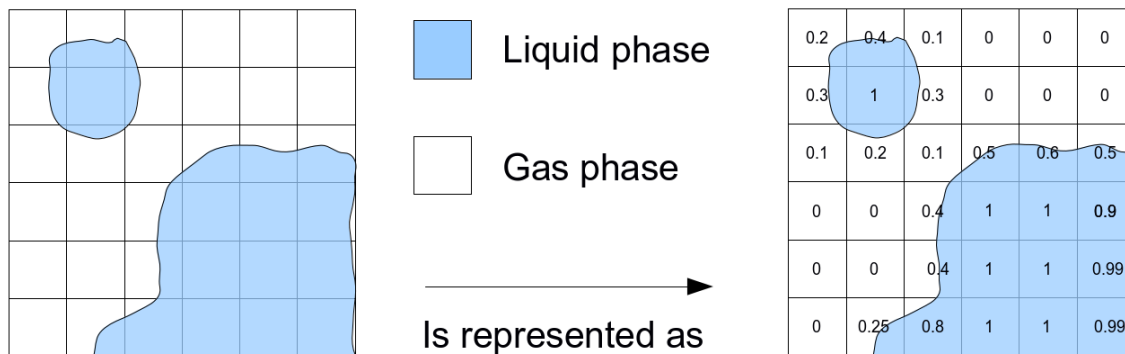
Figure 5.4: Example two-fluid model

liquid phase (in blue) and a gas phase (in white). Each control volume is annotated by its α value. Values of 1 are filled entirely by the liquid phase and 0 are filled entirely by the gas phase.

Due to the loss of information associated with the averaging process, additional terms are included in the governing equations. In order to close them, additional

terms to account for the transfer of momentum between phases are included. These are known as the averaged inter-phase momentum transfer terms and are responsible for the forces interacting at the interface between each phase. Additional challenges are also encountered when modelling additional properties of the dispersed phase, such as the size or shape and their effect on the continuous phase [Rusche, 2003].

One of the most attractive features of the two-fluid methodology is that it is applicable to all flow regimes: separated, dispersed or transitional. It is, however, highly dependent on the formulation of turbulence and the inter-phase momentum transfer term, whose treatment depends entirely on the nature of the fluid flow [Brennen, 2005, Rusche, 2003].

5.3   Experimental Analysis

A preliminary experimental study of the process was performed, which used a high speed camera to observe the exit of coolant from the cutting zone. An example is given in Figure 5.5, which records twist-drill coolant behaviour during the cutting process while cutting aluminium. Ideally it would be possible to obtain experimental measurements from various locations in the cutting zone during the cutting process, however this was not possible due to the small dimensions of the cutting zone (up to 5mm in diameter) and the large number of revolutions per minute (up to 10,000 rpm). Alternative methods such as the use of a transparent plastic workpiece and inserting colouring into the coolant were considered. This approach would allow the observation of coolant through the workpiece during the cutting process. This introduces further complications: typical operating parameters for metals are not suitable for plastics and would melt cuttings, and even at lower cutting speeds the scratches introduced by the cutting process would obstruct vision of the cutting zone. Due to these additional complexities it was not possible to observe coolant at the cutting

zone.

However, information still can be gained from observing coolant exiting the cutting hole, as can be seen from Figure 5.5. It shows that the flow appears to be multiphase because the coolant does not exit the cutting zone as a single body of fluid and is mostly exiting via the drill body clearance. This image also shows the complexity of the flow as it incorporates a wide range of scales, as shown by the large range of droplet sizes. Comparing the flow to the multiphase flow regimes characterised by [Ishii, 1975] in Figure 5.2, it is appears to be a mixture

Figure 5.5: Photograph of coolant exiting a twist drill during the cutting process [Coromant, 2013].

of jet flow and droplet flow. From this it is possible to make an informed decision on a suitable modelling methodology. It is required of the chosen methodology to be able to handle large phase fractions and many different droplet scales as well as highly complex and dynamic interfaces between coolant and air. Therefore, separated modelling techniques would not be best suited due to the complex interfaces, and trajectory based models would also not be well suited because of the large volume fractions and the large computational cost associated with it. A two-fluid model would be better suited for this modelling task because it handles large volume fractions better than trajectory models and because the topology is not specified. In order to be able to handle the complex interface structures an appropriate free-surface tracking methodology is required, which will be discussed next.

5.4   Free-Surface Tracking Methodologies

Free-surface modelling methodologies are numerical solution techniques devised for the prediction of two-phase flows where interface locations are one of the outputs of the solution. These numerical techniques are responsible for tracking and locating the interface between two fluids and are typically classified into one of two classes: surface tracking and volume tracking methods. Surface tracking methods are methods which explicitly mark and track the interface between fluids through the use of marker particles or by attaching a mesh to it. The use of the interface marker particles method is shown in Figure 5.6(a), which marks the interface between two fluids on a fixed grid using a set of massless particles. The local velocities are then used to advect the interface in a Lagrangian manner. Another example of a surface tracking method are moving mesh methods, illustrated in figure 5.6(b). These methods maintain the exact position of the interface by attaching the computational mesh to the interface. The main advantage of surface tracking methods is that the representation of interface surface is modelled independently of the flow field. Therefore the resolution of the surface and the flow can be chosen

(a) Marker particle method
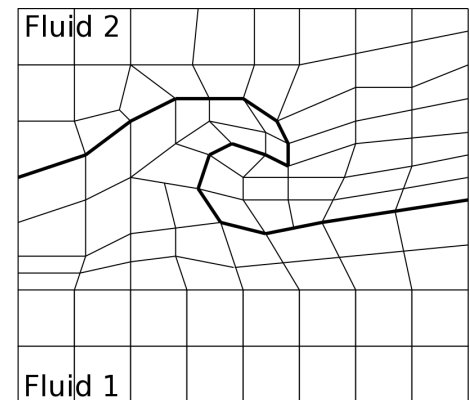
(b) Moving mesh method

Figure 5.6:   Example surface tracking methods

independently. This can be desirable when a greater level of resolution is required at the interface without needing to increase flow field resolution. Furthermore, the exact position of the interface is stored, which makes interface analysis easier.

However, difficulties are encountered when the topology of the interface changes significantly, such as the merging or rupturing of interfaces [Ubbink, 1997]. In addition to this, surface tracking methods do not strictly conserve the volume of each fluid, whereas flow quantities are conserved in volume based methods. Volume tracking methods track the interface between two fluids by marking each of the fluids using an indicator function, such as a volume fraction or level set. Where the volume fraction represents the amount of a single phase in a cell volume and level set describes the shortest distance between the point and the interface [Sussman et al., 1994]. An example volume tracking method is given in Figure 5.7 which uses volume fractions. Volume tracking methods encounter the issue of how to convect the interface
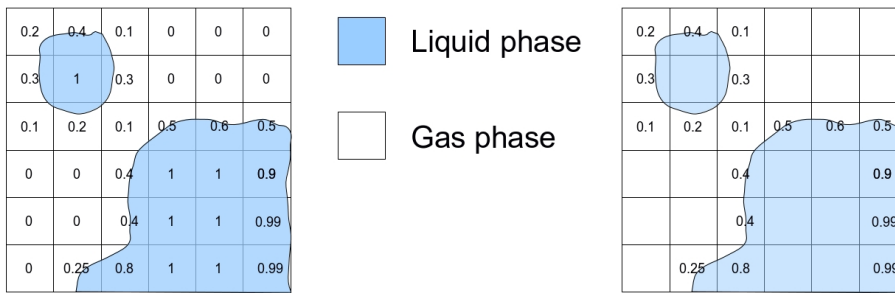
Figure 5.7: Volume tracking.

without diffusing or disperse it, which is particularly challenging when using volume fractions because the convection scheme must guarantee volume fraction boundedness (between 0 and 1). Resolving this issue has led to two different methodologies for convecting the volume fraction: high-order convection schemes and Volume Of Fluid (VOF) methods which utilise convection schemes that reconstruct the interface based on the distribution of volume fractions before advecting it [Hirt and Nichols, 1981, Ashgriz and Poo, 1991, Rider and Kothe, 1995, Rudman, 1997]. VOF is one of the most widely used methods for multiphase flows and due to its robustness is used in a number of commercial CFD codes [Ubbink, 1997]. Because of the VOF's ability to handle a wide range of multiphase scales, complex interfaces and large phase fractions, it was chosen as the free-surface modelling methodology for this model.

5.5   The Volume of Fluid Method

The classical VOF model is an Eulerian based formulation which models the behaviour of each fluid phase on a fixed mesh [Hirt and Nichols, 1981]. However, unlike the two-fluid approach, where two sets of Euler equations are solved (one for each phase), the VOF model employs a single set of equations to model both phases through the use of a mixture model. Rather than tracking particles and the interface of each fluid, the VOF method tracks the volume of each fluid within each control volume, which is represented in the form of a volume fraction, α. This volume fraction is defined for one particular fluid phase inside a cell as its material volume divided by the total cell volume. Therefore α is zero or unity in pure fluid control volumes and has a value of $0 < \alpha < 1$ in the multi-fluid interface cells. By observing the multi-fluid control volumes, a description of the interface for each fluid can be created at the current time step.

The VOF method uses a single set of equations for the entire computational domain, which consists of the continuity and momentum equations for an isothermal, Newtonian fluid. These equations are given in Chapter 2, and are given again here for convenience:

$$\boldsymbol{\nabla} \cdot \mathbf{U} = 0, \tag{5.1}$$

$$\frac{\partial(\rho\mathbf{U})}{\partial t} + \boldsymbol{\nabla} \cdot (\rho\mathbf{U}\mathbf{U}) = -\boldsymbol{\nabla}p + \boldsymbol{\nabla} \cdot \mathbf{T} + \rho\mathbf{f_b} \tag{5.2}$$

Where $\mathbf{U}$ is the velocity vector shared by the two fluids through the domain, t is the time, $\mathbf{T}$ is the deviatoric viscous stress tensor $\mathbf{T} = 2\mu\mathbf{S} - 2\mu(\boldsymbol{\nabla} \cdot \mathbf{U})\mathbf{I}/3$ with the mean rate of strain tensor $\mathbf{S} = 0.5[\boldsymbol{\nabla}\mathbf{U} + (\boldsymbol{\nabla}\mathbf{U})^T]$, p is pressure, α is the volume fraction and f_b are body forces per unit mass. The conventional VOF model also solves an additional transport equation for the volume fraction given by:

$$\frac{\partial \alpha}{\partial t} + \boldsymbol{\nabla} \cdot (\mathbf{U}\alpha) = 0 \tag{5.3}$$

This equation represents the volume fraction of a single phase and is solved simultaneously with the continuity and momentum equations. As two phases are being modelled, the density ρ and viscosity μ are defined as a weighted average:

$$\rho = \rho_l \alpha + \rho_g (1 - \alpha) \tag{5.4}$$

$$\mu = \mu_l \alpha + \mu_g (1 - \alpha) \tag{5.5}$$

Subscript l and g denote the liquid and gaseous phases, respectively. An important issue when using the VOF model for numerical simulations of free-surface flows is the conservation of the volume fraction. In the case of flows with high density ratios, small errors in the volume fraction can lead to significant errors in the calculation of physical properties. The precise calculation of the volume fraction distribution is crucial for accurate evaluation of surface curvature, because it is required for the determination of pressure gradients across the free surface caused by surface tension. The interface between two phases is typically spread across a number of control volumes and is therefore highly sensitive to grid resolution [Deshpande et al., 2012, Ubbink, 1997].

5.6 Numerical Description

In this thesis, an approach similar to one proposed by [Hirt and Nichols, 1981] is used, as implemented in the OpenFOAM CFD library [Weller et al., 1998]. MRFInterFOAM is a numerical solver for multiphase flows with multiple rotating components which is pre-packaged with OpenFOAM. This model uses a modified VOF model using the finite volume discretisation [OpenCFD, 2013]. The systematic

derivation for the model used in this project is outlined below [Deshpande et al., 2012].

The model implementation describes velocity in terms of a weighted average between the liquid and gas velocities given by:

$$\mathbf{U} = \alpha\mathbf{U_l} + (1 - \alpha)\mathbf{U}_g \tag{5.6}$$

The use of a weighted average introduces an additional convective term into the volume transport equation which provides a sharper interface. When solving the volume fraction for each phase, a segregated approach is used. The transport equations for each volume fraction are defined below as:

$$\frac{\partial\alpha}{\partial t} + \boldsymbol{\nabla} \cdot (\mathbf{U}_l\alpha) = 0 \tag{5.7}$$

$$\frac{\partial(1 - \alpha)}{\partial t} + \boldsymbol{\nabla} \cdot \left[\mathbf{U}_g(1 - \alpha)\right] = 0 \tag{5.8}$$

These equations assume that the contributions of each phase to the advance of the fluid-fluid interface are proportional to the appropriate volume fraction. Beginning with the transport equation 5.3, equation (5.7) is now rearranged as an evolution equation for the volume fraction:

$$\frac{\partial\alpha}{\partial t} + \boldsymbol{\nabla} \cdot (\mathbf{U}\alpha) = 0 \tag{5.9}$$

$\mathbf{U}$ is then replaced by its definition as a weighted average:

$$\frac{\partial\alpha}{\partial t} + \boldsymbol{\nabla} \cdot \left\{[\alpha\mathbf{U_l} + (1 - \alpha)\mathbf{U_g}]\alpha\right\} = 0 \tag{5.10}$$

Using the definition of the relative velocity $\mathbf{U_g}$ is then isolated:

$$\mathbf{U_r} = \mathbf{U_l} - \mathbf{U_g} \tag{5.11}$$

$$\mathbf{U_g} = \mathbf{U_l} - \mathbf{U_r} \tag{5.12}$$

Substituting this into the above transport equation produces the following:

$$\frac{\partial \alpha}{\partial t} + \boldsymbol{\nabla} \cdot \left\{ [\mathbf{U_l} - (1-\alpha)\mathbf{U_r}]\alpha \right\} = 0 \tag{5.13}$$

which is rearranged to:

$$\underbrace{\frac{\partial \alpha}{\partial t} + \boldsymbol{\nabla} \cdot (\mathbf{U_l}\alpha)}_{=0} - \boldsymbol{\nabla} \cdot [(1-\alpha)\alpha\mathbf{U_r}] = 0 \tag{5.14}$$

For the liquid phase, the first two terms on the left hand side are zero by definition of the transport equation. This leaves:

$$\boldsymbol{\nabla} \cdot [(1-\alpha)\alpha\mathbf{U_r}] = 0 \tag{5.15}$$

After this term is added to the volume transport equation, an evolution volume fraction equation for α is given by:

$$\frac{\partial \alpha}{\partial t} + \boldsymbol{\nabla} \cdot (\mathbf{U}\alpha) + \boldsymbol{\nabla} \cdot \left[\mathbf{U}_r\alpha(1-\alpha) \right] = 0 \tag{5.16}$$

This new term has no influence on cells with volume fractions at the upper and lower limits, because the equation reduces to the form of equation (5.3). This additional term is responsible for a sharper multi-fluid cell interface and creates a strong coupling between the transport equation (5.16) and equation (5.6).

5.6.1   Surface Tension

Surface tension is caused by the mutual attraction of water molecules and is the energy required to stretch a unit change of a surface area [Ono and Kondo, 1960]. MRFInterFOAM accounts for surface tension within the momentum equation by including it as a body force, f_{sv}. Surface tension at the liquid-gas interface generates an additional pressure gradient, which is evaluated per unit volume through the use of a Continuum Surface Force model (CSF). The equation for the evaluation of surface tension forces uses the CSF formulation of Brackbill et al. [Brackbill et al., 1992]:

$$\mathbf{f}_{sv} = \sigma \kappa \hat{\mathbf{n}} \delta_s \qquad (5.17)$$

Here σ is the surface tension, $\hat{\mathbf{n}}$ is the normal vector of the interface δ_s is the interface delta function and κ is the mean curvature of the interface, defined by:

$$\kappa = -\boldsymbol{\nabla} \cdot \left(\frac{\boldsymbol{\nabla} \alpha}{|\boldsymbol{\nabla} \alpha|} \right) \qquad (5.18)$$

The fluids in this project are considered to be Newtonian and incompressible and the rate of strain tensor is linearly related to the stress tensor. This is decomposed into a more convenient form for discretisation:

$$\boldsymbol{\nabla} \cdot T = \boldsymbol{\nabla} \cdot \mu \left[\boldsymbol{\nabla} \mathbf{U} + (\boldsymbol{\nabla} \mathbf{U})^T \right] = \boldsymbol{\nabla} \cdot (\mu \boldsymbol{\nabla} \mathbf{U}) + (\boldsymbol{\nabla} \mathbf{U}) \cdot \boldsymbol{\nabla} \mu \qquad (5.19)$$

The present VOF method considers a single pressure system where the normal component of the pressure gradient at a stationary non-vertical no-slip wall, must be different for each phase due to the hydrostatic component $\rho \mathbf{g}$ when the phases are separated at the wall, i.e., if a contact line exists. In order to simplify the definition of boundary conditions, it is common to define a modified pressure as:

$$p_d = p - \rho \mathbf{g} \cdot \mathbf{x} \qquad (5.20)$$

Here, $\mathbf{x}$ is the position vector and pressure is modified by the density gradient and the body force due to gravity. In order to satisfy the momentum equation, the pressure gradient is expressed using equation (5.20) and can be substituted into give:

$$\frac{\partial \rho \mathbf{U}}{\partial t} + \boldsymbol{\nabla} \cdot (\rho \mathbf{U}\mathbf{U}) - \boldsymbol{\nabla} \cdot (\mu \boldsymbol{\nabla} \mathbf{U}) - (\boldsymbol{\nabla}\mathbf{U}) \cdot \boldsymbol{\nabla}\mu = -\boldsymbol{\nabla}p_d - \mathbf{g} \cdot \mathbf{x}\boldsymbol{\nabla}\rho + \sigma\kappa\boldsymbol{\nabla}\alpha \quad (5.21)$$

Body forces due to pressure gradient and gravity are implicitly account for by the first two terms on the right-hand side of equation (5.21). In summary, the mathematical model implemented is given by the continuity equation (5.22), the volume fraction transport equation (5.16), and momentum equation (5.21):

$$\boldsymbol{\nabla} \cdot \mathbf{U} = 0, \tag{5.22}$$

$$\frac{\partial \alpha}{\partial t} + \boldsymbol{\nabla} \cdot (\mathbf{U}\alpha) + \boldsymbol{\nabla} \cdot \left[\mathbf{U}_r \alpha(1-\alpha) \right] = 0 \tag{5.23}$$

$$\frac{\partial \rho \mathbf{U}}{\partial t} + \boldsymbol{\nabla} \cdot (\rho \mathbf{U}\mathbf{U}) - \boldsymbol{\nabla} \cdot (\mu \boldsymbol{\nabla} \mathbf{U}) - (\boldsymbol{\nabla}\mathbf{U}) \cdot \boldsymbol{\nabla}\mu = -\boldsymbol{\nabla}p_d - \mathbf{g} \cdot \mathbf{x}\boldsymbol{\nabla}\rho + \sigma\kappa\boldsymbol{\nabla}\alpha$$

This approach has been evaluated against a range of different multiphase flow regimes, such as droplet impact and crater formation [Berberović et al., 2009], modulated jets [Srinivasan et al., 2011] film falling over turbulence wires [Raach et al., 2011] and Deshpande, [Deshpande et al., 2012], who evaluates its performance for both inertia dominated and surface tension dominated flows.

5.6.2   Modelling Flow Rotation

MRFInterFOAM accounts for rotation similarly to the approach used in Section 3.5, via source terms. This is achieved by including the Coriolis and Centrifugal terms shown in Equation 3.7 for each rotating component. The numerical model is set in the frame of reference of the tool, where the entire computational domain rotates

in the opposite direction to which the tool rotates. As a result of using the tool's frame of reference, the tool geometry is therefore specified as not rotating and the additional source terms to account for rotation do not apply to this boundary only. This approach avoids the use of a complex moving mesh approach which would be required to account for the movement of the outlet of the coolant channel.

5.6.3 Dimensional Analysis

Non dimensional analysis of the Navier Stokes equations performed in Section 2.5 analysed the Reynolds, Dean and Rossby numbers. For convenience, the Reynolds number suggests the flow is fully turbulent and the Rossby number indicated that rotation will not have a significant influence on the flow of coolant. However, the Dean number is not applicable to this numerical model because the geometry is no longer a curved channel. In addition to these dimensionless numbers, dimensionless numbers must be considered for these flows which are associated with the surface tension term: the Capillary number and the Weber number.

Capillary Number

The capillary number measures the relative importance of viscous and surface tension stresses across an interface between two phases. This is defined as:

$$Ca = \frac{\mu U}{\sigma} \tag{5.24}$$

where μ is fluid dynamic viscosity(1.002×10^{-3}Pa $\cdot$ s), U characteristic velocity (80m/s) and σ the surface tension coefficient between the two phases. The capillary number for this flow is estimated to be typically around 1.1, which suggests a balance between viscous and surface tension forces.

Weber Number

The Weber number is a dimensionless number used for multiphase flows which measures the importance of fluid inertia compared to surface tension. The Weber number is useful when analysing thin film flows as well as the formation of droplets and bubbles [Duan et al., 2003]. This is defined as:

$$We = \frac{\rho v^2 l}{\sigma} \qquad (5.25)$$

Considering the experimental measurements taken in Chapter 2, where the average velocity of coolant exiting the tool, U, is between 40 and 80m/s, the coolant channel diameter, $l = 0.001m$ and the fluid is treated as water with $\sigma = 0.07$N/m and density $\rho = 1000$kg/m^3, the Weber number for coolant exit flow is between 20,000 and 90,000. This suggests that surface tension forces will not have a significant effect of the flow of coolant and that inertia will dominate the flow.

5.7 Boundary Conditions

The purpose and application of the boundary conditions have previously been discussed in Section 3.6. The main goal of boundary conditions is to provide start and end points for the solution procedure. The specification of boundary conditions in this case is somewhat more complicated because the inlet conditions of the model are dependent on the results of the single phase model. In order for the single phase model to inform the multiphase simulation, the boundary conditions for velocity are again fixed value with values mapped from the single phase simulation.

As a result of introducing an additional transport equation to account for the transport of the phase fraction, α, boundary conditions for the scalar field α must also be specified. The boundary conditions for the volume fraction are fixed value at

the inlet, which specifies that the flow entering the domain is purely coolant. Outlet conditions are specified as a zero gradient boundary condition. The boundary conditions at the wall are specified as zero gradient for pressure and the volume fraction.

5.8   Solution Procedure

The solution procedure is responsible for gathering each component of the computational model to solve the governing equations. MRFInterFOAM uses a merged PISO-SIMPLE algorithm, known as PIMPLE. PISO is an acronym for Pressure Implicit Splitting of Operators for time dependent flows and was first proposed by [Issa, 1986]. The PISO algorithm is an efficient method of solving the Navier Stokes equations for unsteady flow problems and Each time step is solved through the following key steps.

    1 Set the boundary conditions.

    2 Solve the discretised momentum equations to compute an intermediate velocity field.

    3 Compute the mass fluxes at cell faces.

    4 Correct the mass fluxes at the cell faces.

    5 Correct the velocities on the basis of the new pressure field.

    6 Update the boundary conditions.

    7 Repeat from 3 for the prescribed number of times (for PISO correction).

    8 Increase the time step and repeat from 1.

It is also important to note that steps 4 and 5 can be repeated for to correct for non-orthogonality. SIMPLE stands for Semi-Implicit Method for Pressure Linked

Equations which was previously used in Chapter 3 for steady state flow. The PIM-PLE algorithm uses the above PISO procedure with two important additions, an outer correction loop, which iterates over the current time step using the previous iterations final values as initial conditions. The second addition is that the PIMPLE algorithm uses under-relaxation of the variables between consequent outer iterations [Ferziger and Perić, 2002].

5.8.1 Experimental Validation: Unconfined Coolant Flow

As discussed in Section 5.3, it was not possible to obtain experimental data from within the cutting zone during the cutting process, but it was possible however to record high-speed camera footage of a coolant exiting a free spinning drill. A free spinning drill is a drill which is rotating and is not positioned near a workpiece. In the experimental case examined the coolant was supplied at a pump pressure of 40 bar and the
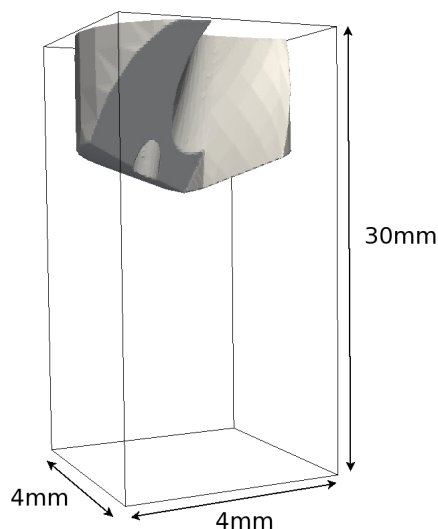
Figure 5.8: Computational domain used for validation.

tool was rotating at 10,000 rpm. The computational mesh modelled a three dimensional tool inside a cuboid of 4 rectangular faces and 2 square faces and was created using snappyHexMesh, illustrated in Figure 5.8. This simplified case was used to validate the numerical model described throughout this chapter.

The numerical results shown in Figure 5.9 and 5.10 show the tool geometry in white with coolant exiting the geometry. Coolant is visualised by taking visualising the cells with values of $\alpha > 0.5$, which are then coloured by velocity. The pale white region surrounding the coolant is a secondary threshold of which $\alpha > 0.1$ to

observe small quantities of coolant breaking away from the jet of coolant, this is made translucent to aid visualisation. Figure 5.9 (a) shows experimental observations of coolant exiting a rotating twist drill at the parameters given above. The experimental results show that as coolant exits the tool the coolant exits in an arched formation. Figure 5.9 (b) shows the predicted coolant exit behaviour and it can be seen that there is good qualitative agreement between the numerical and experimental data on the arched exit formation of coolant.

Figure 5.10 (a) shows coolant leaving the drill exit from a different relative position. These results show that the coolant is also arching in a secondary direction which is opposite to the direction of the helical channel. Figure 5.10 (b) presents the predicted coolant exit flow and shows that the secondary arch features in the experimental data is also reproduced with this model.

In summary, the experimental results show that as the coolant exits the tool the flow arches in two different directions. The numerical model implemented in this chapter qualitatively matches the limited experimental data available. This provides a degree of confidence that the numerical model can handle the complicated free surface structure, large numbers of revolutions per minute and highly turbulent flows.

(a) Experimental   (b) Numerical
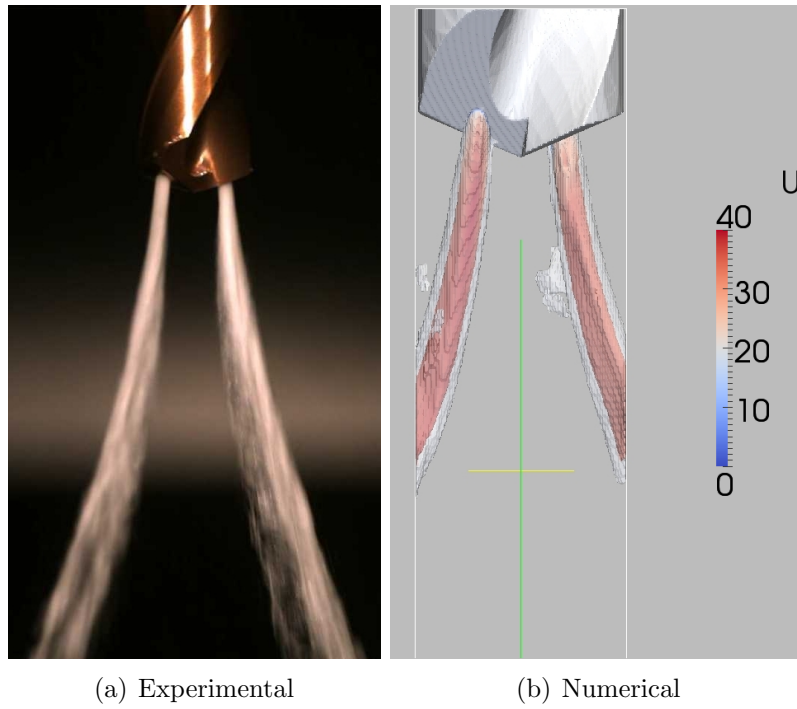
Figure 5.9: Numerical and Experimental observation of coolant exiting a free spinning twist-drill [Coromant, 2013].

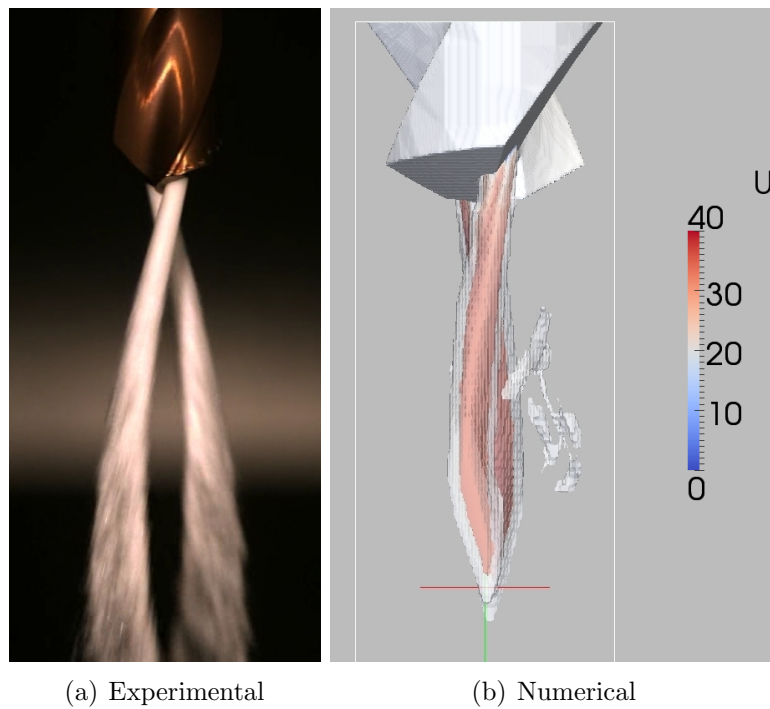

(a) Experimental   (b) Numerical

Figure 5.10: Numerical and Experimental observation of coolant exiting a free spinning twist-drill [Coromant, 2013].

5.9   Summary

This chapter has given an overview of multiphase modelling techniques and has examined experimental data to determine a suitable free-surface modelling methodology.

The validation of the multiphase model described in this chapter included a discussion used experimental observations to validate the numerical model. The numerical predictions made in this study qualitatively agreed with experimental observations for a simplified case of coolant exiting a free-spinning tool.

Until recently, few scientific studies have focused on the application of coolant in twist-drill machining. A single phase model has recently been used [Fallenstein and Aurich, 2014] to examine the flow field and to predict the transfer of heat from the tool into the coolant, but the experimental data gathered in this work suggests that the model cannot be limited to a single phase model. Multiphase modelling techniques have thus far not been applied to twist-drill coolant analysis, and so the model produced in this chapter contributes to significantly expanding this particular field of study.

Chapter 6

Coolant Exit Flow Analysis

6.1   Introduction

In the previous chapter the numerical model was described and validated against the simplified case of a free spinning drill. The primary objective of this chapter is to analyse the exit flow of coolant within a cutting hole under realistic operating conditions using the numerical model. In order to do this, first a description of the geometry variations will be given, next a more detailed description of the geometric features to be examined will be outlined before discussing the meshing techniques employed. This chapter will then go on to give a detailed analysis of the CFD results and close with further model validation.

6.2   Tool Geometry

This chapter will focus on calculating the coolant exit flow located for the Sandvik Coromant R457 twist-drill geometry, which is 8mm in diameter, 8cm in total tool length and illustrated in Figure 6.1. Due to limits on computational resources only a selection of coolant channel configurations were examined:

(a)
Tool
overview

(b) Tool tip
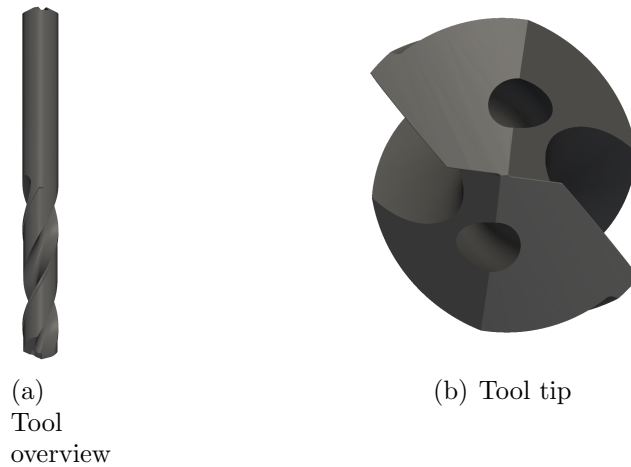
Figure 6.1: R457 tool geometry

Case A - examines the flow of coolant exiting a channel of 1mm in diameter with 3.6mm Radial Spacing (RS) and positioned on the edge between the primary and tertiary clearance.

Case B - simulates coolant flow through coolant channels positioned on the edge between the primary and tertiary clearance of 1mm in diameter and 2.3mm RS.

Case C - calculates coolant flow when exiting coolant channels of 1.2mm in diameter with 3.6mm RS located along the edge between the primary and tertiary clearance.

Case D - simulates coolant exit flow from a coolant channel of 0.5mm diameter, 3.6mm RS and are positioned in the Primary Clearance (PC) of the tool.

These configurations were selected in order to observe the behaviour of coolant when the channel size, distance from the centre of the tool, mass flow rate and exit face changes. For clarity the primary and tertiary clearance is illustrated in red for the reader in Figure 6.2(e) and 6.2(f) respectively. In addition to this the axial rake and chisel edge are referred to later in this chapter and are defined in Figure 6.2(g) and 6.2(h) for clarity. For each numerical model a fixed average inlet velocity is specified as 40m/s. Therefore, the difference in channel diameters for cases C and D results in the mass flow rate for these systems changing. The mass flow rate for the larger channel diameter, case C, is increased and the mass flow rate is decreased for the model with smaller channel diameter, case D. This specification allows the examination of coolant spreading for both an increased and decrease in mass flow rate in addition to changes in channel position.
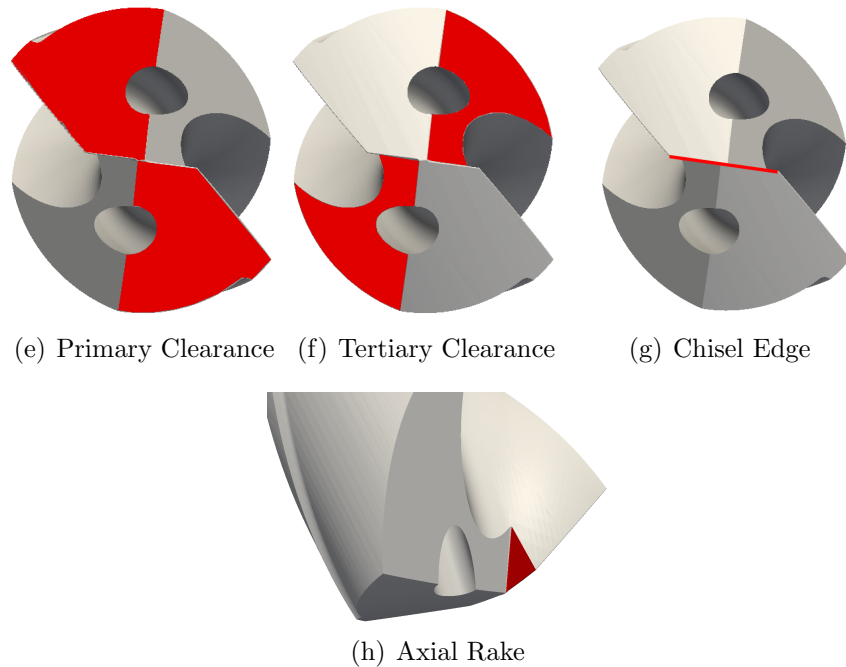

(e) Primary Clearance   (f) Tertiary Clearance   (g) Chisel Edge

(h) Axial Rake

Figure 6.2: R457 tool geometry diagram

6.3 Flow Domain Description: Confined Flow

The unconfined flow considered in Section 5.8.1 demonstrates that the numerical model is able to reproduce the flow phenomena occurring when coolant exits a free spinning drill. However, during the cutting process the tool is confined to a cutting hole and CFD of free-spinning tools does not give much insight into the distribution of coolant. Therefore, the representation of the fluid domain in computational space needs to be modified to account for cutting hole. Because heat is highly localised to the cutting zone the behaviour of coolant located outside of the cutting zone is not of significant interest because it does not aid with the removal of cuttings or thermal energy. As a result of this, only the immediate area of the cutting zone is modelled. This is illustrated in Figure 6.3, where a cutting hole (in blue) produced by the cutting tool needs to be modelled. Furthermore, because the geometry is symmetrical only a single coolant channel is modelled. This is further illustrated in Figure 6.4 which shows the fluid domain in blue to be represented in computational space.
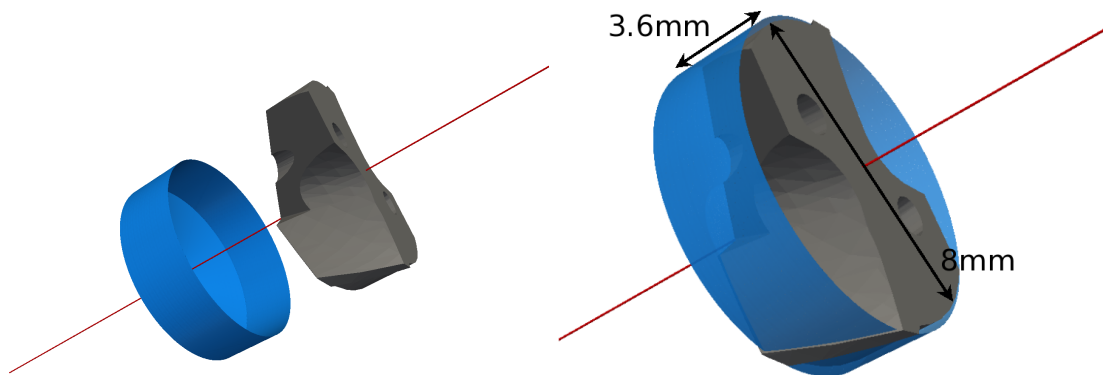

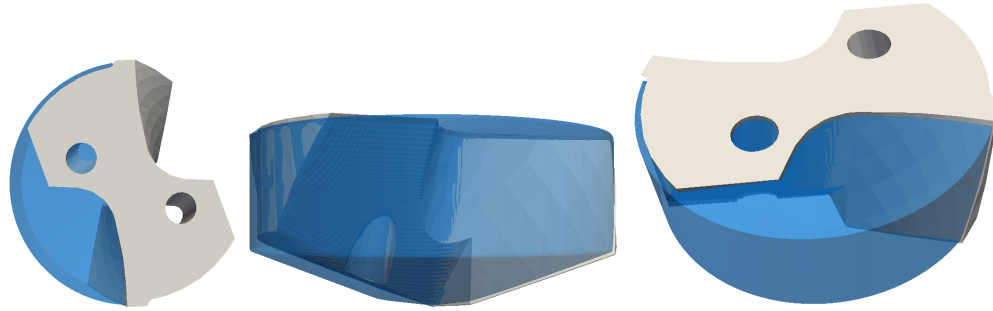Figure 6.3: R457 tool geometry diagram

Figure 6.4: Fluid domain (blue) surrounding the R457 tool geometry

6.4 Mesh Generation

Due to the highly complex structure of the tool cutting geometry combined with the cutting hole it would not be time efficient to manually create a structured mesh of the fluid domain. In order to facilitate the meshing process, mesh pre-processing tools provided by the OpenFOAM [OpenCFD, 2013] library were used to generate the mesh of the fluid domain.

This process required a geometry file, a stereolithography file (.stl), which contains the geometry of the cutting tool. This information was exported from specialist CAD software. The computational mesh of the fluid domain was created using snappyHexMesh. SnappyHexMesh operates by taking a structured mesh, which will be referred to as a base mesh, then placing the geometry stored in the geometry file inside the base mesh. Mesh cells which are positioned outside of the desired fluid domain are then removed. Once all appropriate cells are removed, the mesh is then 'snapped' to the tool geometry and refined according to user defined criteria.

A major challenge was that the topology of the workpiece is not included within the geometry file and using basic shapes for a base mesh will not include this accurately. The issues with using basic shapes as a base mesh are highlighted in Figure 6.5(a) and 6.5(b) which use a cylindrical base mesh.

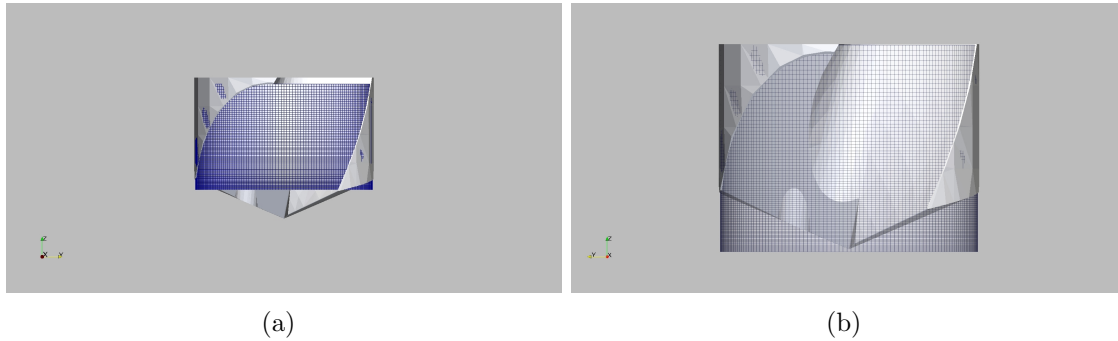(a)   (b)

Figure 6.5: Tool geometry positioned inside two meshes of a cylinder.

Figure 6.5(a) and 6.5(b) illustrates the use of a cylindrical base mesh combined with a twist-drill geometry. The base mesh shown in Figure 6.5(a) does not encapsulate the cutting edge and therefore the resulting mesh from snappyHexMesh will not model the cutting edge at all. This is because snappyHexMesh only removes and refines the base mesh which it is given and does not extend the fluid domain. Figure 6.5(b) on the other hand shows a mesh of a cylinder which fully encapsulates the cutting edge. Using this base mesh would result in a mesh which models a tool where only the tip of the tool is in contact with a flat surface and would not accurately represent a cutting hole because coolant can pass directly under each cutting edge.

Therefore the shape of the workpiece either has to be generated as an additional geometry file or defined within the base mesh. Rather than further increase the complexity of the meshing task given to snappyHexMesh by creating additional geometry files to model the workpiece, the base mesh of a cylinder is deformed to model the bottom of the cutting hole. The holes produced by the tool in this case are conical with a second change in inclination towards the centre of the tool. It is important to note that the shape of the cutting hole can change depending on the shape of the cutting geometry. The cutting edges responsible for the shape of the

cutting hole are marked in red and black in Figure 6.6 and it can be seen that this tool has two cutting edges which are in contact with the work-piece during machining. The location of the points at the limits of each of these edges, labelled R1 and R2, are used to modify the cylindrical base mesh to align with the cutting edges and create a cutting hole with the correct topology. The deformation is achieved
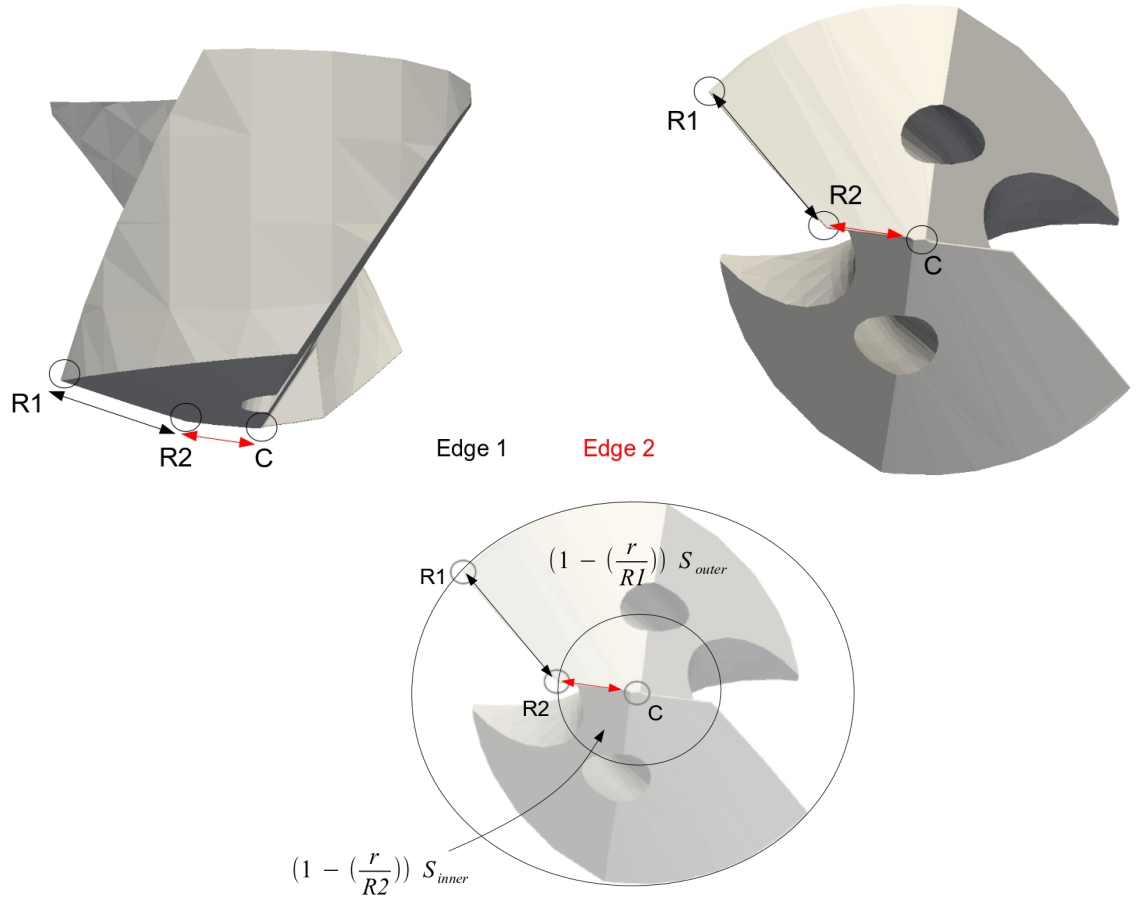

Figure 6.6: Edges R1 and R2 which intersect the bottom of the flow domain.

via the following function for cells with radial distance from the central axis of the tool greater than $R2$:

$$z_{new} = z_{old} - (1 - (\frac{r}{R1}))S_{\text{outer}} \tag{6.1}$$

And for the inner region of the mesh, which have radial distance from the central tool axis less than $R2$:

$$z_{new} = z_{old} - (1 - (\frac{r}{R2}))S_{\text{inner}} \tag{6.2}$$

This assumes that the tool is oriented parallel to the z axis and the tip of the drill points in the negative z direction. r is the radial distance from the central axis of the tool and S is a spacing function based on the cells position along the z axes before deformation (z_{old}). A 2D slice of the resulting computational mesh is given in Figure 6.7 (a). Figure 6.7 (b) shows the final 3D base mesh used with the tool geometry positioned inside it before being processed by snappyHexMesh. The pale, translucent areas of the image depict the mesh and the blue illustrates the tool and the dark blue areas are parts of the tool geometry which intersect the boundary of the mesh. The resulting fluid domain mesh after processing with snappyHexMesh is given in Figure 6.7 (c). Now that the governing equations, boundary conditions and the computational mesh have been specified, the solution procedure mentioned previous in Section 5.8 was employed to solve the governing equations for each geometry specified in Section 6.2. The computational mesh for each too geometry were made up of approximately one million cells and took a month to complete each. These simulations were particularly expensive computationally because a very small time step is necessary (1×10^{-8} seconds) to maintain a maximum Courant number between 0 and 1, which is a result of the combination of the large fluid velocity and the use of small control volumes, which are necessary to capture small quantities of coolant. The analysis carried out next is made up of several parts, domain flooding, surface wetting analysis and flow feature analysis.

(a)

(b)

(c)
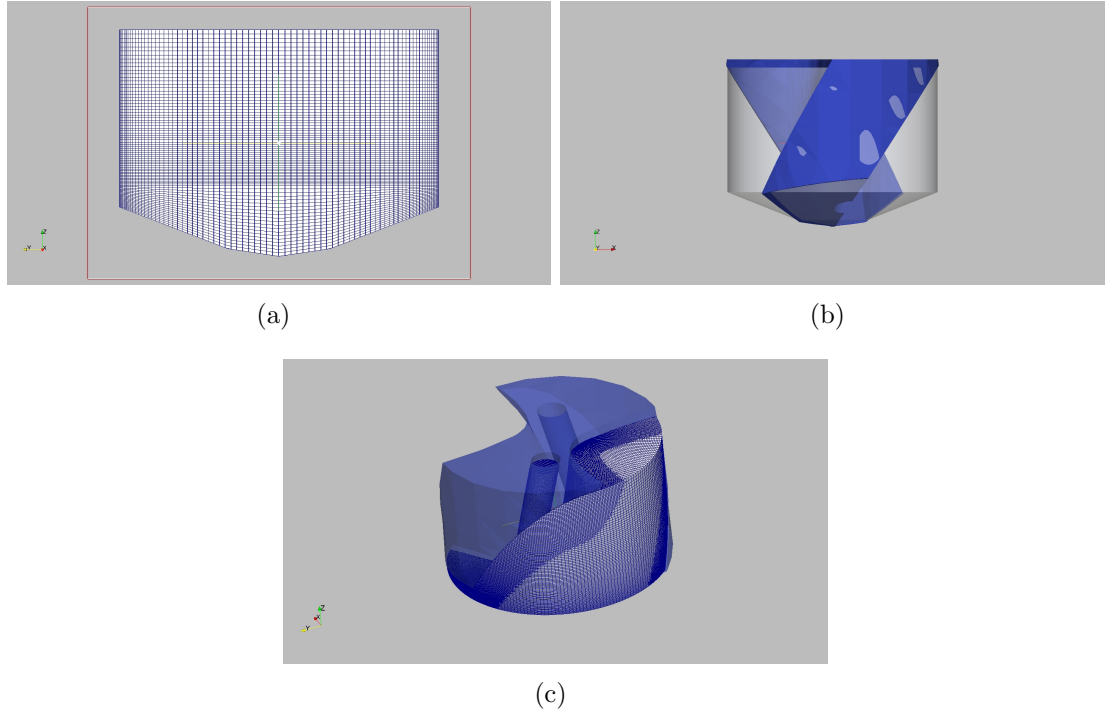
Figure 6.7: Mesh of a deformed cylinder with tool geometry positioned within it and graphical representation of fluid domain mesh produced using snappyHexMesh.

6.5 Domain Flooding Analysis

As discussed in Section 5.8.1, the flow of coolant exiting the cutting hole is a multiphase problem. The motivation behind this study is to gain insight into how much of the cutting zone is flooded or how long it takes for the cutting zone to become fully flooded. Both of which will influence drill cooling. This is achieved by calculating the volume of coolant located in the cutting zone at each time step by the following:

$$\sum_{i=1}^{N} V_i \alpha_i \tag{6.3}$$

where N is the number of control volumes, V_i the volume of control volume i and α_i is the volume fraction stored at control volume i. These calculations are performed over each case detailed in Section 6.1 for the remainder of this section and will express the calculated amount of coolant as a percentage of the total domain volume.

6.5.1 Case A: 1mm diameter, 3.6mm RS

The domain flooding analysis results for case A are given in Figure 6.8. This figure shows that the domain initially fills quickly for the first 0.0007 seconds, at which point the gradient of increase begins to steadily decrease until the domain becomes approximately 60% full at 0.004 seconds. Once the domain reaches 60% capacity it appears to reach a steady state, however it is unclear whether this is a steady state and not a pause in the filling of the domain because only a small fraction of a second has been simulated. Furthermore, this behaviour may be isolated to this tool design and coolant channel configuration. This will examined in more detail in Section 6.5.5.

6.5.2 Case B: 1mm diameter, 2.3mm RS

The results for the domain flooding analysis for case B are provided in Figure 6.9 and display a very similar profile to case A. In this Figure the fluid domain initially fills very quickly before the gradient of increase begins to decrease in the same way as case A. For case B the numerical model takes approximately 0.004 seconds before it reaches a steady state at approximately 60% capacity. The consistent filling behaviour between models here is significant because it suggests that the distance of the channel exit position from the centre of the tool does not have a significant influence on the amount of coolant which floods the cutting zone.
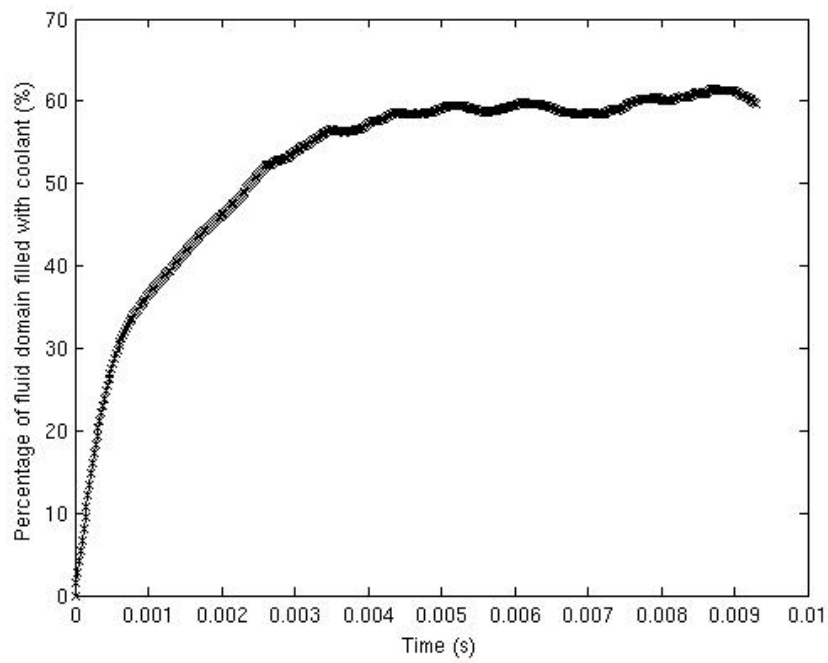
Figure 6.8: Case A. Volume of fluid domain filled with coolant as a function of time
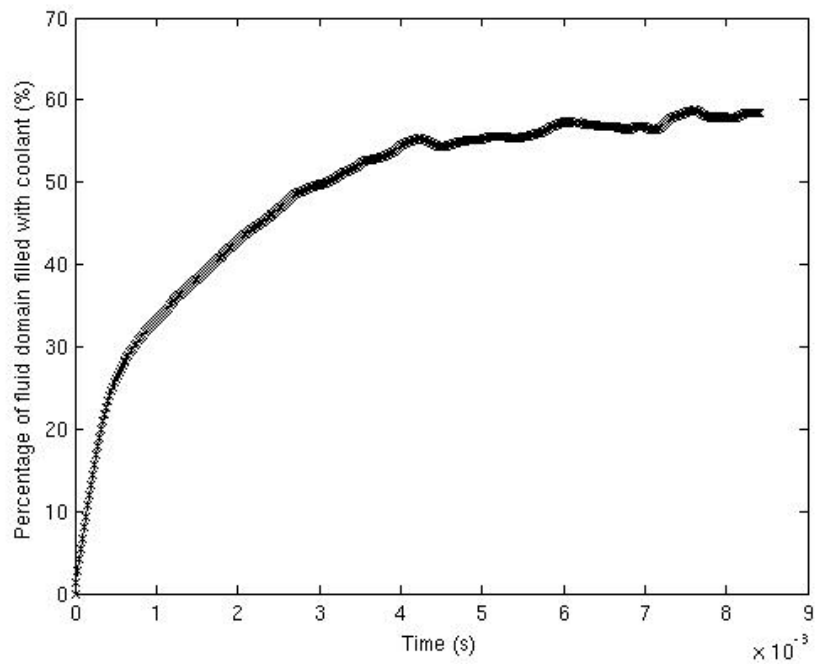

Figure 6.9: Case B. Volume of fluid domain filled with coolant as a function of time

6.5.3   Case C: 1.2mm diameter, 3.6mm RS

The results in Figure 6.10 show the domain flooding analysis for case C. These results show the domain filling at a fast rate for the first 0.0005 seconds. After 0.0005 seconds the gradient of increase then begins to decrease until a steady state is reached at 60% of the total fluid domain volume.

Although this result is very similar to cases A and B, as stated in Section 6.1, this case simulates coolant flow for an increased mass flow rate. The observation that there is not a significant change in coolant behaviour is particularly significant for this case because the diameter of the channel has increased by 20% and the domain is no more flooded than case A.

6.5.4   Case D: 1.2mm diameter, 3.6mm RS in PC

The percentage of the fluid domain composed of coolant over time for case D is given in Figure 6.11. The results show the domain filling very quickly before the gradient of increase steadily decreases at approximately 0.004 seconds. Like the previous cases examined, this model also reaches a steady state. This is particularly interesting because it suggests that the amount of coolant located in the cutting zone is not sensitive to the size or positioning of the channels.

6.5.5   Further Numerical Analysis

In order to determine whether a steady state is actually reached in these simulations, a final numerical evaluation of case C for an extended amount of time of 0.03 seconds was performed. This case was selected under the assumption that if the domain were to fully flood it would occur sooner than other cases due to the increased mass flow specified at the inlet. The results from this analysis are given in Figure 6.12. This figure also shows the amount of coolant located in the cutting zone over time as a
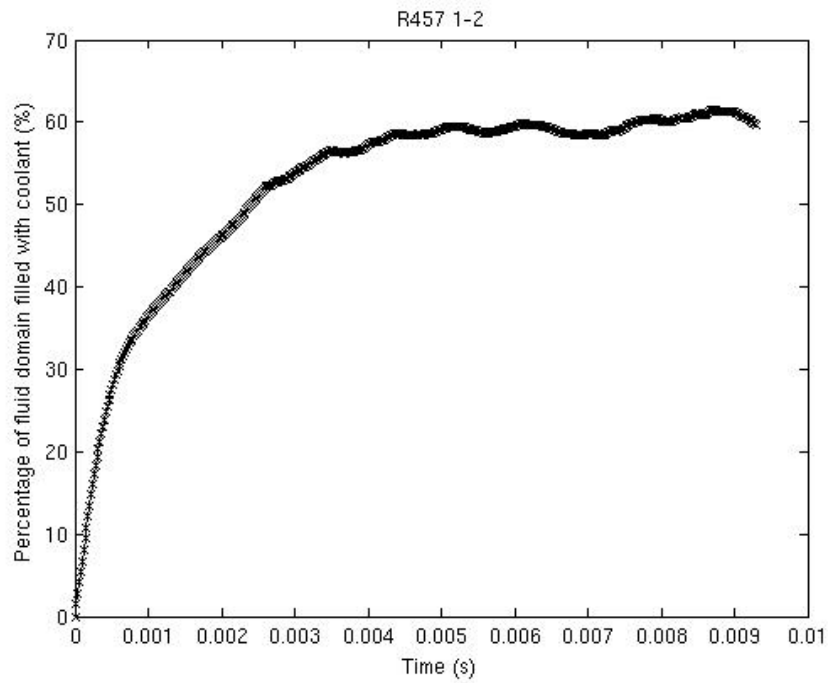
Figure 6.10: Case C. Volume of fluid domain filled with coolant over time
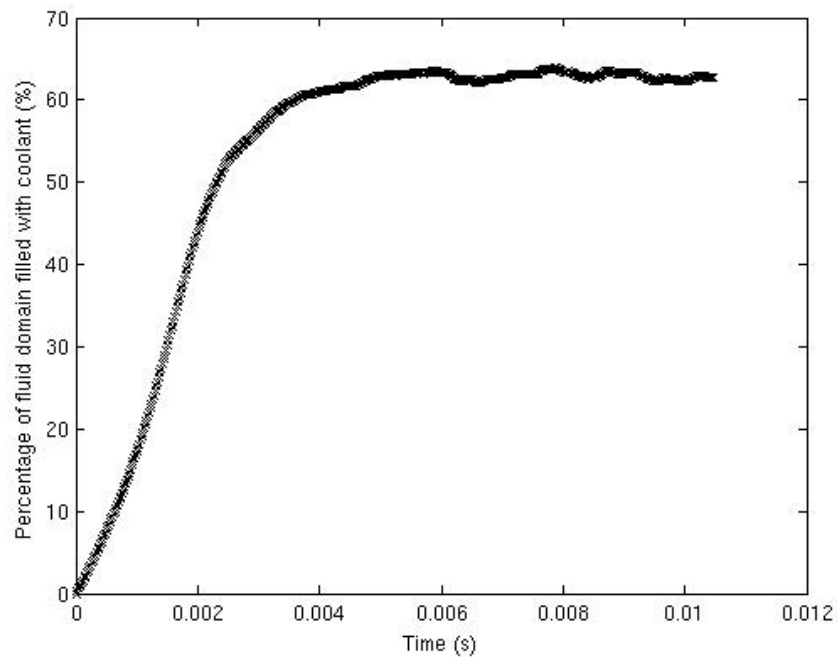
Figure 6.11: Case D. Volume of fluid domain filled with coolant as a function of time
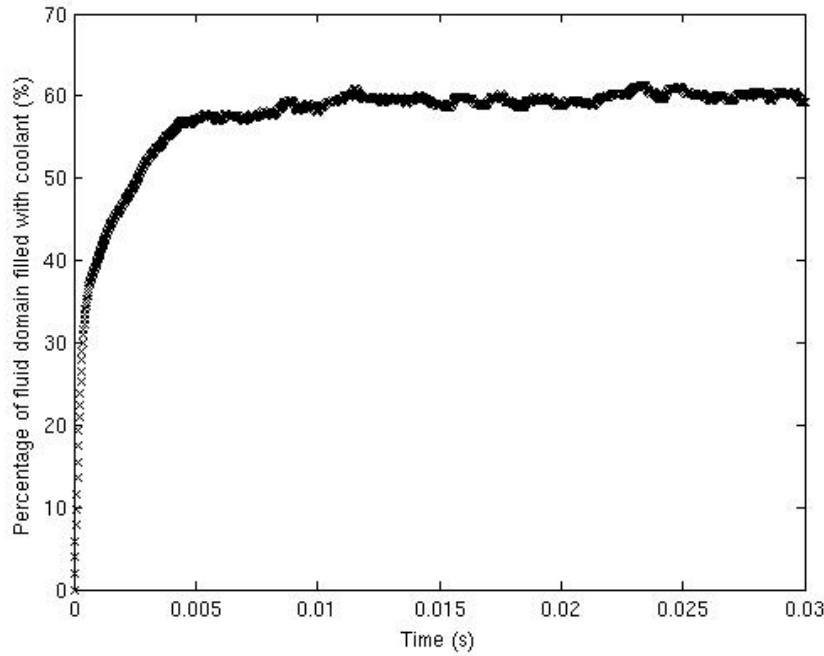
Figure 6.12: Volume of fluid domain filled with coolant as a function of time

percentage of the total volume of the cutting zone. It can be seen that after reaching 60% capacity at 0.004 seconds the amount of coolant contained in the cutting zone fluctuates about this value for the rest of the simulated time and appears to have reached an approximately steady state.

6.5.6   Summary of Domain Flooding Analysis

This study has examined the models outlined in Section 6.1 in order to examine the filling behaviour of the fluid domain for a range of different coolant channel geometries to verify whether the fluid domain becomes fully flooded and if it does, how long it takes to become fully flooded. The study found that cases all cases filled to approximately 60% capacity with coolant before reaching a steady state. This finding is interesting because the volume of coolant in the fluid domain does not appear to be very sensitive to the radial spacing, which changed by 36% between cases A and B, mass flow rate of the system, which increased by over 40% between

cases A and C and the exit face of the coolant channel (case D).

Additional time was spent determining whether the numerical solution reaches a steady state because if the domain completely fills with coolant the flow would reduce to a single phase problem and a multiphase model would not be required. This was confirmed by performing numerical calculations for an extended amount of time and found the domain flooding did reach a steady state. This behaviour of coolant at the cutting zone has not been reported previously. Clearly a more extensive study is needed to determine whether this is true for all coolant channel designs and is isolated to the R457 geometry. It has however, so far been found consistent across a number of different coolant channel configurations and mass flow rates.

6.6 Analysis of the Calculated Wetted Area

One of the most important requirements of coolant in twist-drill machining is the removal of heat via convection. This section analyses application of coolant to the surface of the tool by calculating the percentage of the surface which is coated in coolant. The wetted area of the tool surface is calculated at each time step using:

$$\sum_{i=1}^{N_f} A_{f_i} \alpha_{f_i} \tag{6.4}$$

where N_f is the number of faces which make up the tool surface, A_{f_i} is the area of face i and α_{f_i} is the value of the volume fraction at face i. This section will examine each case identified in Section 6.1 for total wetted area represented as a percentage of the total tool surface area.

6.6.1 Case A: 1mm diameter, 3.6mm RS

Wetted area analysis for case A is provided in Figure 6.13, which displays the percentage wetted surface area of the tool modelled in case A as a function of time. The results in this figure show that there is a sharp increase in wetted area for the first 0.0007 seconds, after this point the wetted area slowly increases to approximately 65% at 0.004 seconds where it effectively reaches a steady state. This result is particularly significant because it suggests that approximately 36% of the tool surface is not supplied with coolant at all.

6.6.2 Case B: 1mm diameter, 2.3mm RS

Figure 6.14 presents the wetted tool area analysis for case B. This result shows an initial sharp increase to 50% at 0.0005 seconds, after this point the wetted area increases unsteadily until 0.004 seconds where the simulation reaches a steady state of approximately 64%. These results show that despite the radial spacing decreasing by 36% between cases A and B, the wetting behaviour is very similar to case A. This suggests the wetting behaviour is not very sensitive to its distance from the centre of the tool and that the partial wetting of the tool surface calculated for case A is not isolated to that particular design.
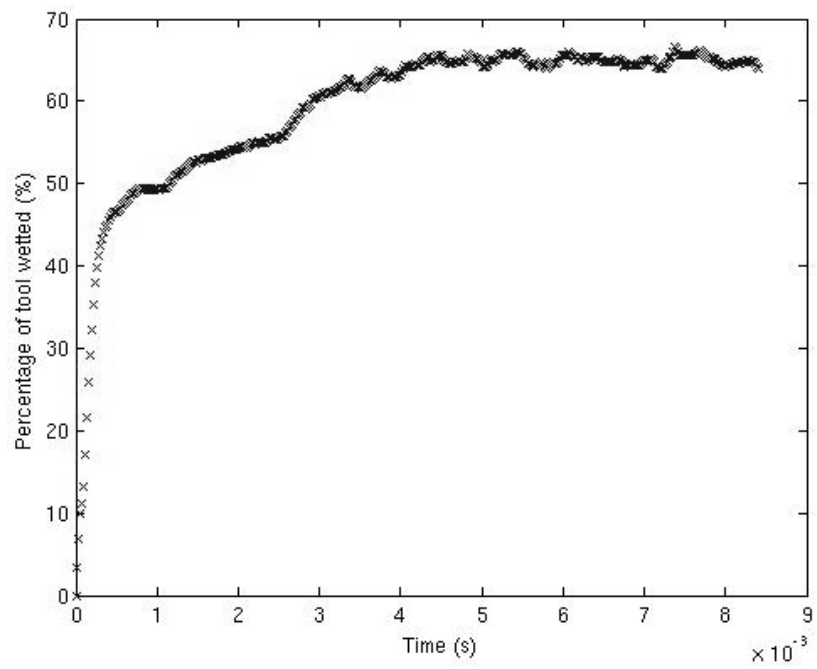
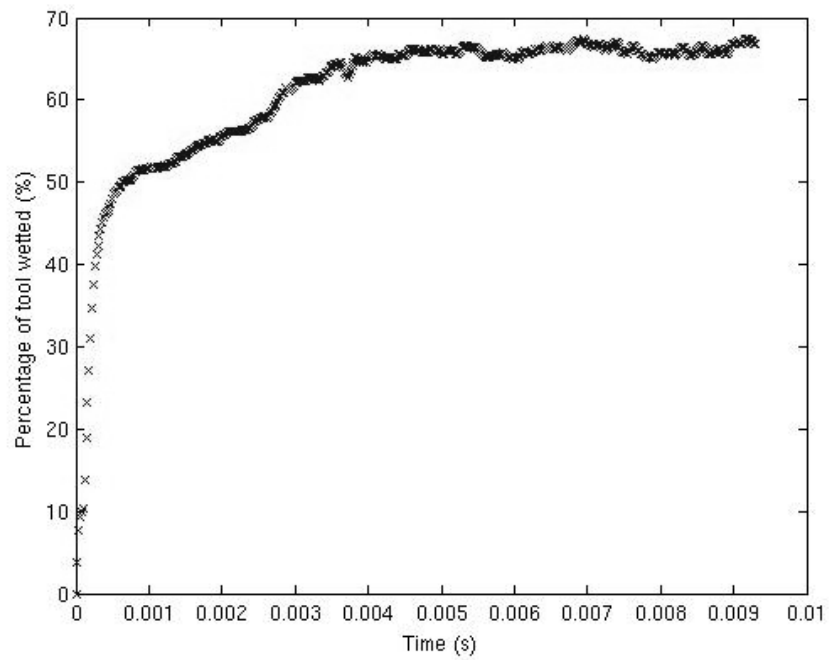Figure 6.13: Case A. Wetted tool area as a function of time.

Figure 6.14: Case B. Wetted tool area as a function of time.

6.6.3   Case C: 1.2mm diameter, 3.6mm RS

Surface wetting analysis for case C is demonstrated in Figure 6.15. Much like cases A and B, this figure shows a sharp increase in wetted tool surface for the first 0.0008 seconds of simulation time after which the wetted area increases at a much slower rate until approximately 0.005 seconds where the percentage of wetted area reaches a steady state. At this steady state, 30% of tool surface unwetted. The fact that this case behaves very similarly to case A is particularly interesting because it suggests that the change in channel diameter and mass flow rate are not having a significant influence on distribution of coolant across the tool surface.

6.6.4   Case D: 0.5mm diameter, 3.6mm RS in PC

The percentage of wetted surface area over time for the final case, case D, is given in Figure 6.16. For this case the wetted area initially increases and as simulation time increases the gradient of increase steadily decreases until a steady state is reached of 60% at 0.003 seconds. This behaviour is significant because the profile of the graph is very different to that of cases A, B and C, but still reaches a steady state. This suggests that the percentage of the surface which is coated with coolant is not significantly effected by the positioning of the coolant channels exit face or the flow rate of coolant. However, this study does not indicate which components of the tool surface are coated in coolant and it may be the case that different components of the tool geometry are supplied with coolant with each configuration.

6.6.5   Visual Surface Wetting Analysis

The wetted area analysis carried out previously gives valuable insight into how much of the tool surface is coated in coolant, however this quantitative analysis does not indicate which areas of the tool are supplied with coolant. Because a high percentage of wetted surface area cannot identify if crucial components of the tool, such as the
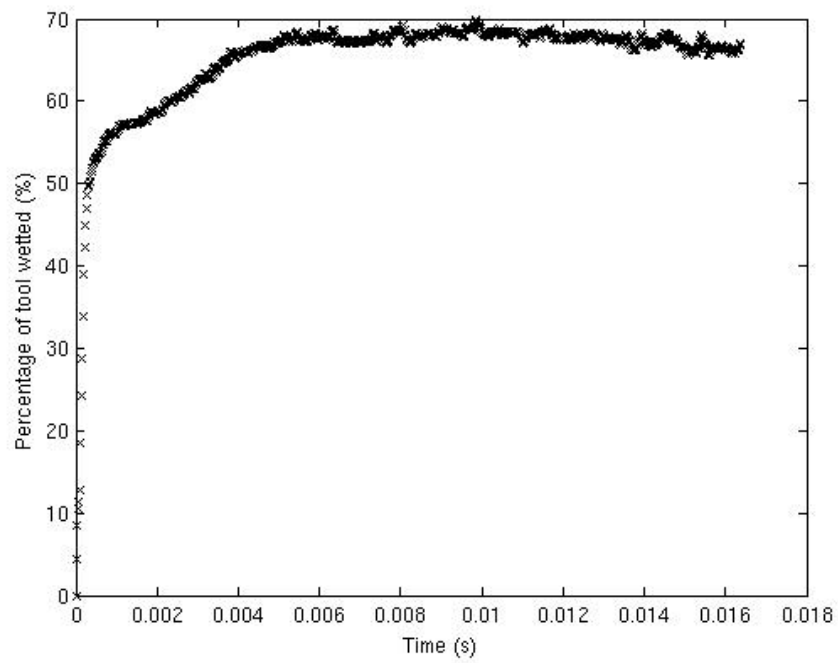
Figure 6.15: Case C. Wetted tool area as a function of time.
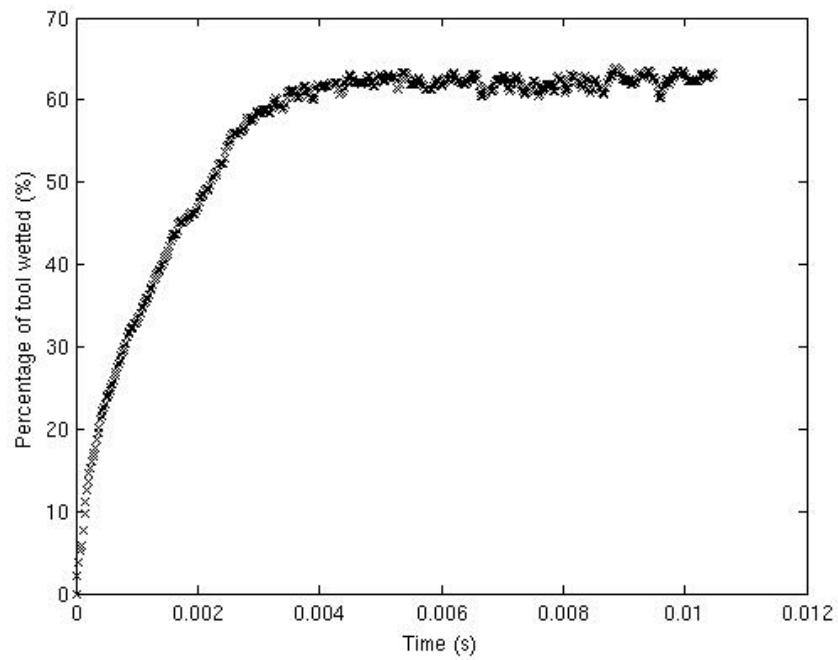
Figure 6.16: Case D. Wetted tool area as a function of time.

(a) Case A

(b) Case B
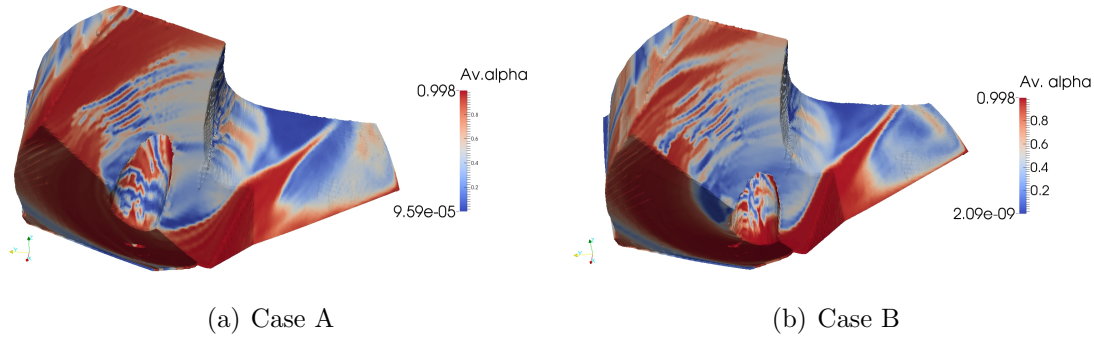
Figure 6.17: Surface of the tool geometry colour by the average value of the volume fraction.

cutting edge, are applied with coolant. This section will provide visual analysis of the coolant distribution across the tool surface. Due to the time dependent nature of the spreading of coolant, an average value for the volume fraction at each face is calculated. The figures presented throughout the remainder of this section will visualise the surface coloured by the average value of alpha. Red regions indicate well wetted regions of the tool surface, whereas blue regions indicate areas of the surface which are not well supplied with coolant.

6.6.6 Case A: 1mm diameter, 3.6mm RS

The distribution of coolant for case A is shown in Figure 6.17(a). Four key areas of wetting can be identified in this figure. The first and second areas are both well supplied with coolant, the primary clearance and second clearance. The third feature is the axial rake which is also well supplied with coolant and appears to direct the distribution of coolant up the tool flute. Finally it is important to note that the topside of the cutting edge does not appear to be very well supplied with coolant, especially the outer corner.

(a) Case C   (b) Case D
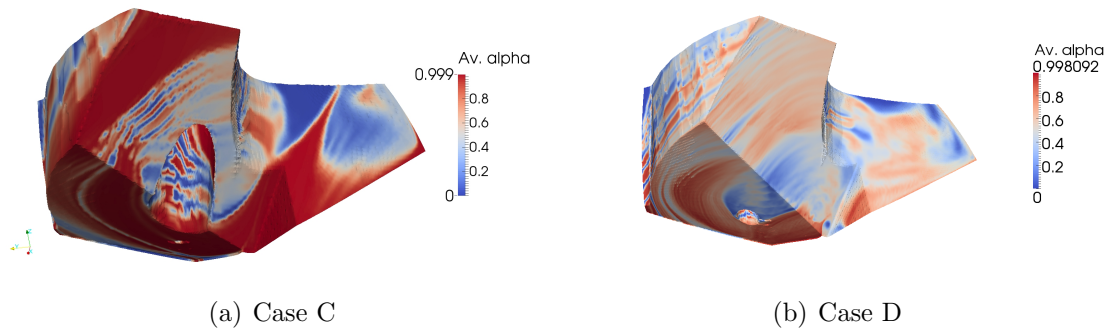
Figure 6.18: Surface of the tool geometry colour by the average value of the volume fraction.

6.6.7 Case B: 1mm diameter, 2.3mm RS

A visual analysis of the wetted area for case B is given in Figure 6.17(b). This distribution is very similar to case A, but shows small differences adjacent to the cool exit hole. This is the blue area indicating coolant has not been applied here. As in case A there are three main locations well supplied with coolant; the primary and tertiary clearance and the axial rake. This case also shares the features of directing coolant up the drill flute and small quantities of coolant directed towards the cutting edge. This is particularly interesting because even though the distance between the channel and the central axis of the tool has decreased by 36%, the distribution of coolant does not appear significantly different.

6.6.8 Case C: 1.2mm diameter, 3.6mm RS

The analysis of coolant distribution for case C is given in Figure 6.18(a). These results also show the primary clearance, tertiary clearance and chisel edge are well supplied with coolant and coolant is spreading across the axial rake and up the drill flute. However, the primary cutting edge is supplied with slightly more coolant on the outer corner than cases A and B. In conjunction with cases A and B, it can be seen that the radial position, size of the channel and flow rate does not appear to

have a significant impact on the distribution of coolant across the surface of the tool because each case exhibits the same dominant flow features.

6.6.9 Case D: 0.5mm diameter, 3.6mm RS in PC

Figure 6.18(b) shows visual wetting analysis for case D. These results show in this case that a portion of the tool located immediately behind the coolant exit is not supplied with coolant. Interestingly in this case, the coolant wets the primary and tertiary clearance and axial rake of the tool, like cases A, B and C, but does not direct coolant up the flute of the tool. The distribution is considerably different and is not as well defined as cases A, B or C. It is unclear whether this behaviour is a result of the reduction in mass flow rate, or due to the positioning of the channel. However it is strongly suggested given cases A and C, which model a change in channel diameter and mass flow rate and do not show a critical change in fluid flow behaviour, that this coolant distribution is a result of the coolant channel being positioned in the primary clearance of the twist-drill.

6.6.10 Summary of Wetted Area Analysis

In summary this section has analysed the wetted area of the tool by quantitatively examining the percentage of the tool coated in coolant over time and by visually inspecting the average distribution of coolant over the face of the tool. For the quantitative analysis, cases A, B and C each display a similar wetting behaviour where the wetted area increases sharply before unsteadily increasing to a steady state. The behaviour between cases does not appear very sensitive to mass flow rate, channel diameter or distance from the centre of tool despite large changes in channel configurations. The steady state for each case however does differ somewhat between configurations:

Case	A	B	C	D
Steady State	65%	64%	67%	62%

Visual analysis has been used to give a more general overview of coolant distribution across the tool face and to identify areas of the tool which are both supplied and not supplied with coolant. Results for cases A, B and C demonstrate a set of key features which each case share in common, where coolant is mostly supplied to the primary clearance and tertiary clearance of the cutting tool, the axial rake and a small area of the drill flute. These flow features have not been shown to be sensitive to changes in mass flow rate and radial spacing of the coolant channel.

The final case considered, case D, displayed some of the same characteristics of cases A, B and C where large amounts of coolant are supplied to the primary clearance and the axial rake of the tool, but did not direct coolant up the flute of the drill. This may be caused by the change in channel position to the primary clearance of the tool or due to the change in mass flow rate. In summary, these results not only give unique insight into which areas of the tool are wetted more than others, but also identify geometric features, such as the chisel edge or axial rake which have an important effect on directing coolant.

6.7   Flow Feature Analysis

While previous studies surrounding the volume of coolant give valuable insight into how much of the fluid domain is made up of coolant, they do not indicate in which regions coolant is located. The surface wetting analysis provided in Section 6.6 also provides important information regarding how much of the tool surface is covered in coolant. However, this analysis gives a limited view of the flow of coolant within the cutting zone because it does not take into account the flow field away from the tool surface area. The purpose of this section is to use the numerical model to examine

the global distribution of coolant throughout the fluid domain. This analysis will give additional insight into how coolant is being directed throughout the cutting zone.

This analysis is performed by visualising the volume fraction scalar field for cell volumes with values 0.5 and above. These cell volumes are then coloured by velocity and a scale is given in each Figure. The illustrative figures also include a translucent tool geometry to aid the visualisation of coolant flow about the tool geometry. For clarity Figure (a) of each case in the following study gives a graphical representation of the tool geometry being modelled with cutting edges and coolant channels marked. In addition to the figures discussed throughout this section, the reader is directed towards the attached animations for an alternative view of the exit behaviour of coolant flow.

(a) View of tool from above

(b) Coolant distribution after 0.00054 seconds

(c) Coolant distribution after 0.0074 seconds

Figure 6.19: Case A. Coolant distribution from above the tool looking down through a translucent tool.

6.7.1 Case A: 1mm Diameter, 3.6mm RS

The numerical results for case A in Figure 6.19 on the opposite page illustrate the flow of coolant at three times, $t = 0$, $t = 0.00054$ and $t = 0.0074$. As previously stated, $t = 0$ demonstrates the geometry for reader reference.

The visualised coolant distribution at 0.00054 seconds (Figure 6.19(b)) shows a large quantity of coolant passing under the primary clearance. From this location coolant is distributed in two key directions. The majority of coolant is distributed in the first direction, towards the workpiece wall. The workpiece wall then directs coolant up the body clearance and along the workpiece wall towards the trailing cutting edge. The second direction is along the axial rake and across the cutting edge. These features are also illustrated in Figure 6.19(c) which visualises coolant steady state flow: black denotes the first direction and red gives the second direction.

Steady state coolant flow given in Figure 6.19(c) illustrates the distribution at time 0.0074. These results do not show any additional flow features than those observed at time $t = 0.00054$, but show an increased volume of coolant in the fluid domain which is mostly localised around the workpiece walls. This image also shows that a small quantity of coolant is directly delivered to the cutting edge via the trajectory marked in red.

(a) View of tool from above
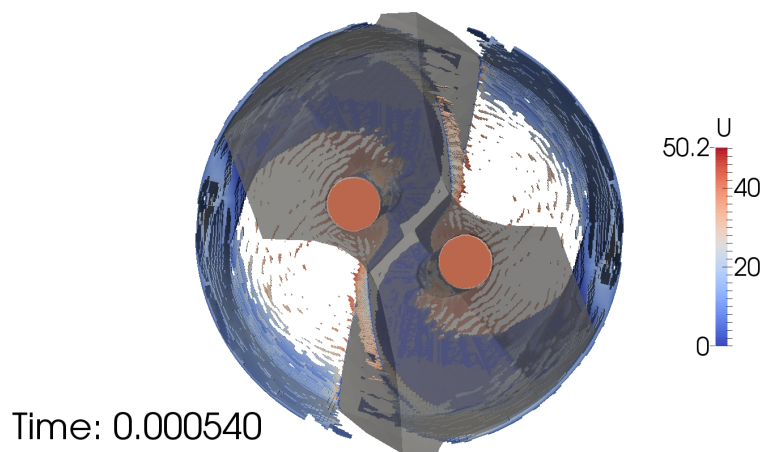
(b) Coolant distribution after 0.00054 seconds
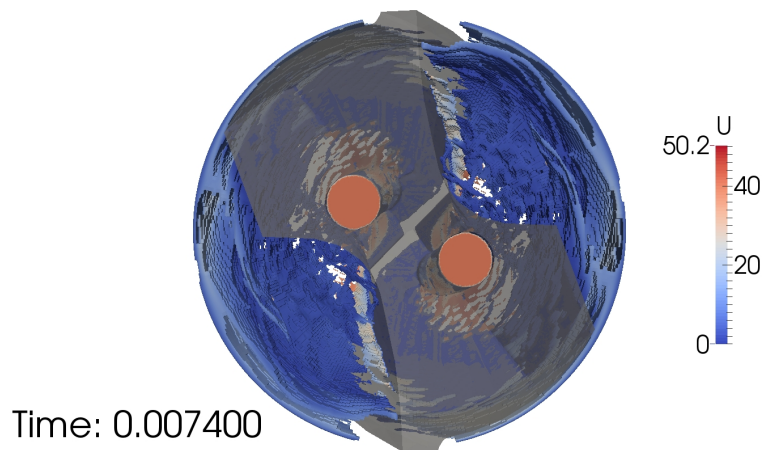
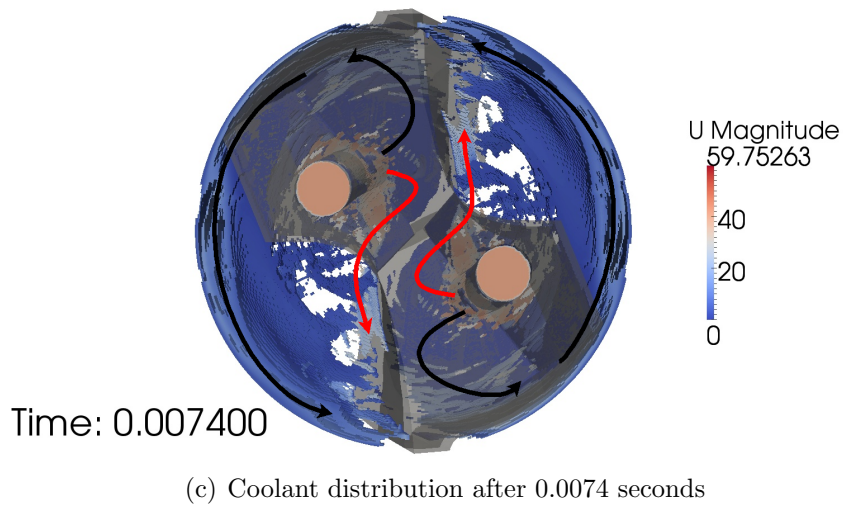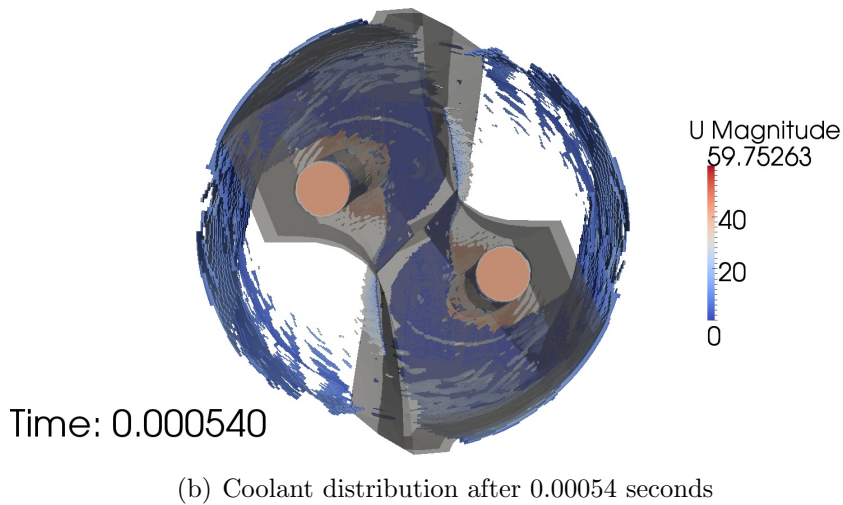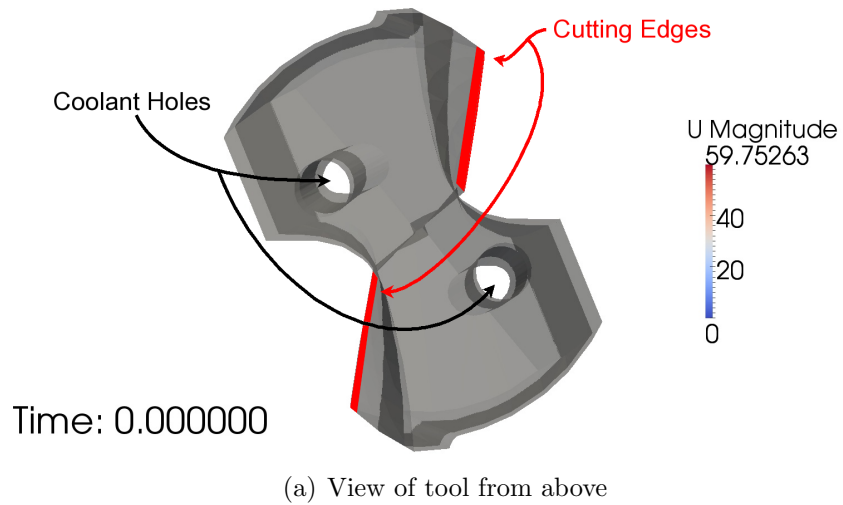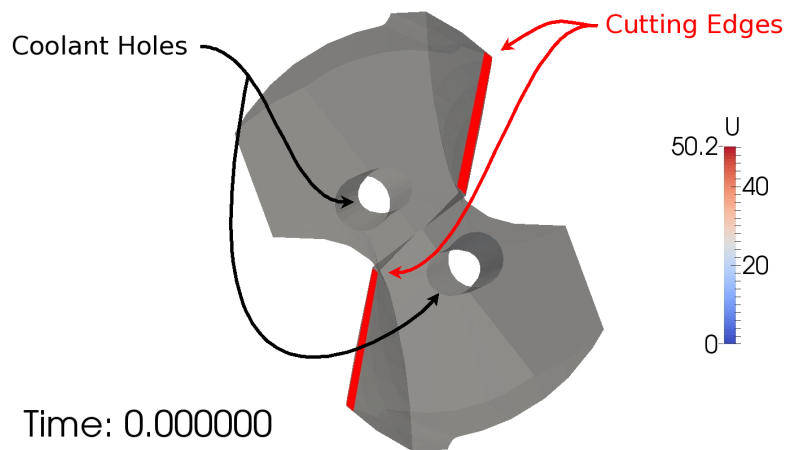(c) Coolant distribution after 0.0074 seconds

Figure 6.20: Case B. Coolant distribution from above the tool looking down through a translucent tool.

6.7.2 Case B: 1mm Diameter, 2.3mm RS

The results for case B are given in Figure 6.20. As in case A, this figure presents the tool geometry from above in (a) and visualises coolant at times $t = 0.00054$ and 0.0074 in (b) and (c) respectively.

Coolant distribution after 0.00054 seconds shows replicates the major flow features observed in case A which show coolant exiting the coolant channel and passing under the primary clearance before being directed by the workpiece walls or axial rake. The steady state distribution of coolant shown in Figure 6.20(c) clearly shows a similar flow profile to case A, where the majority of coolant is distributed around the workpiece wall and a small volume of coolant is provided to the top side of the cutting edge.

Although the same key features as 6.20 (b) and case 6.20 A are observed, it is important to note that there are smaller changes in the flow field. The most significant difference is coolant is being delivered to the centre of the fluid domain which is not supplied with coolant at this time in case A. This could be a result of influencing the amount of fluid which is directed towards the chisel edge or the workpiece wall and measuring the changes in these distributions may give additional insight.

(a) View of tool from above

(b) Coolant distribution after 0.00054 seconds
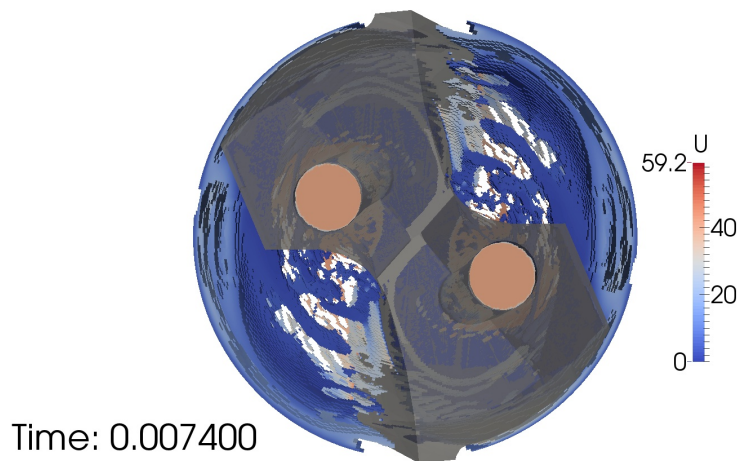
(c) Coolant distribution after 0.0074 seconds

Figure 6.21: Case C. Coolant distribution from above the tool looking down through a translucent tool.

6.7.3   Case C: 1.2mm Diameter, 3.6mm RS

The flow feature analysis for case C is presented in Figure 6.21, which graphically displays coolant distributions at times $t = 0.00054$ and 0.0074 in (b) and (c) opposite.
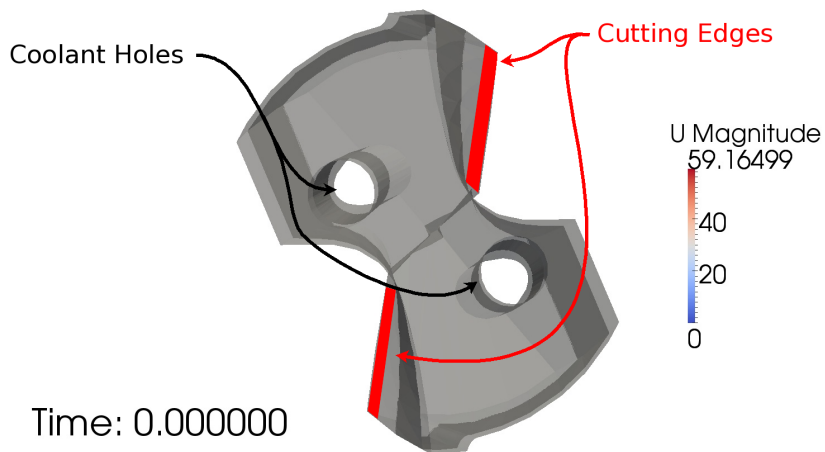
Coolant distribution after 0.00054 seconds (Figure 6.21(b)) shows that coolant distribution is producing the same flow structures recorded in cases A and B. These flow features primarily distribute coolant along the workpiece wall and small quantities of coolant are directed across the trailing cutting edge.

The steady state coolant behaviour in Figure 6.21(c) reflects the flow features observed at time 0.00054 seconds with large quantities of coolant circulating under the primary clearance and the majority of coolant being directed along the workpiece wall and does not demonstrate any significant change in flow behaviour.

The consistency between models A and C is very interesting because model C operates under the same conditions as case A, but with a larger channel diameter and mass flow rate. It can be seen that the increase in mass flow rate associated with this change in cross-section area does not significantly change the behaviour of the flow. This is clearly shown by the flow features displayed at 0.00054 and 0.0074 seconds for cases A and C which do not exhibit any obvious differences in the distribution of coolant. This observation is further reinforced by the consistency between cases seen in the flooding analysis in Section 6.5. This shows that in these two cases the increase in channel diameter and mass flow rate does not introduce any additional flow features and does not influence the amount of coolant located in the cutting zone.

(a) View of tool from above
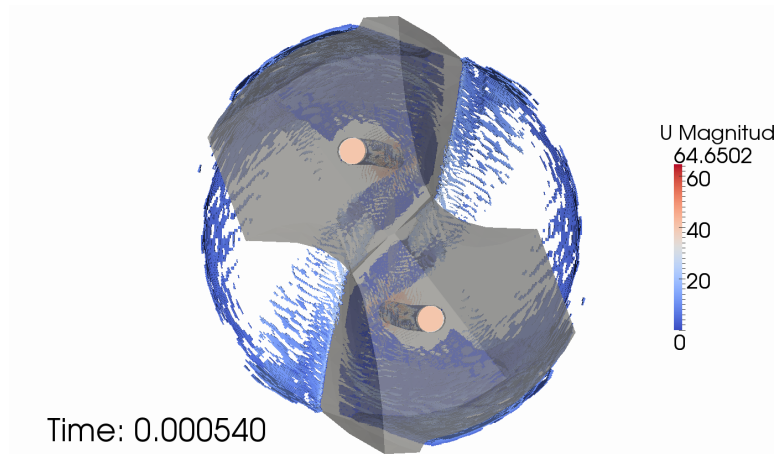
(b) Coolant distribution after 0.00054 seconds
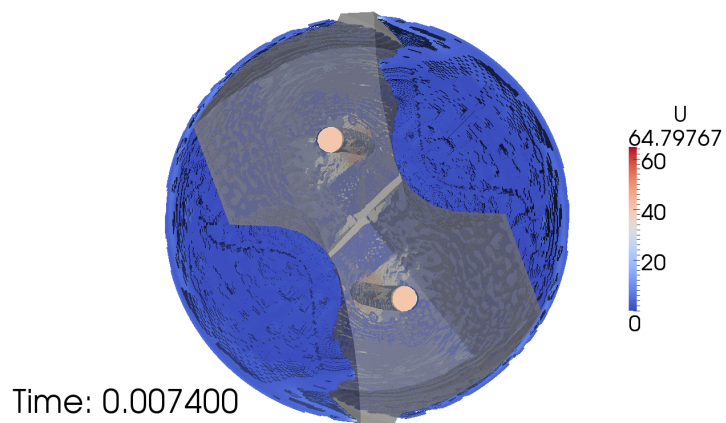
(c) Coolant distribution after 0.0074 seconds

Figure 6.22: Case D. Coolant distribution from above the tool looking down through a translucent tool.
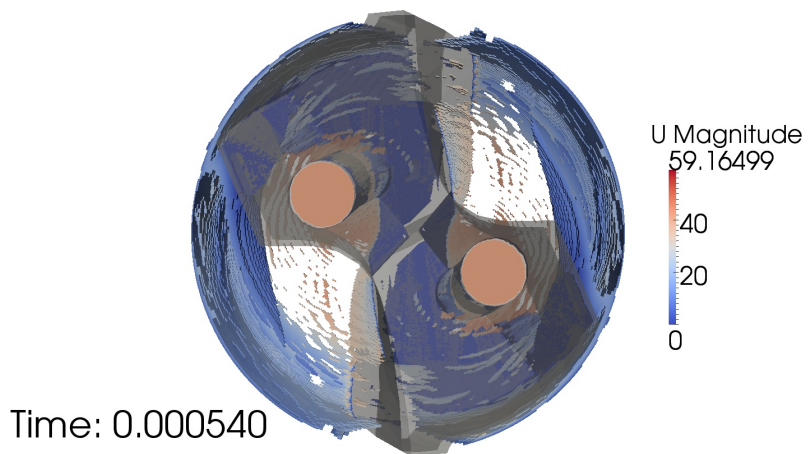
6.7.4   Case D: 0.5mm Diameter, 3.6mm RS in PC
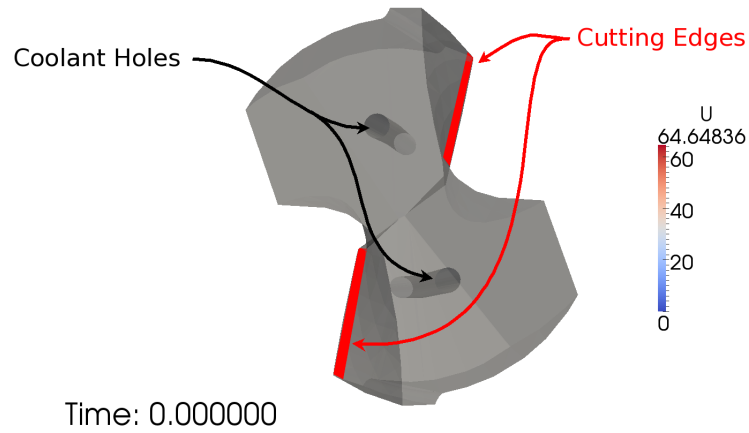
Flow feature analysis for case D is given in Figure 6.22, which also graphically displays coolant distributions at 0.00054 seconds and 0.0074 seconds.

The distribution of coolant after 0.00054 seconds displayed in Figure 6.22(b) mirrors that of cases A, B and C where a large circulation of coolant underneath the primary clearance and along the workpiece wall can be seen. However the distribution is somewhat different in this case because an increased amount of coolant along the topside of the trailing cutting edge is observed. In addition to this, it is interesting to note that there is an area immediately behind the coolant exit position which is not supplied with coolant. The only other case to produce this feature is case A.

Figure 6.22(c) presents the flow at 0.0074 seconds into the simulation. At this point the flow is yet to have reached a steady state, but it can be seen from this image that the fluid domain appears to be made up of a large number of small droplets which are distributed across the entire domain. This flow behaviour is considerably different to the flow visualised in Figure 6.22(b). The underlying flow behaviour illustrated in Figures 6.19(b) 6.20(b) and 6.21(b) are likely to still be operating in this case because the area immediately behind the exit of the coolant channel has still not been applied with coolant. This behaviour is particularly interesting because it is very different to each of the other cases examined, which all exhibit the same clear flow behaviour but with some small differences. It is unclear what causes this change in flow behaviour because there are many variables which are not included within the parameterisation. For example, by locating the coolant channel in the primary clearance of the tool may cause coolant to interact differently with particular geometric features of the tool. The comparison of cases A and C suggest that flow rate and channel size do not significantly influence the distribution of coolant. However, the lack of influence of flow rate and channel dimensions suggested by A

and C may no longer be the case when the channel exit changes position relative to other geometry features.

6.7.5 Summary of Flow Feature Analysis

In summary, the observation and analysis of coolant flow features has examined four different coolant channel configurations. Each of these configurations has shown a key coolant flow feature which all designs hold in common: coolant exits the coolant channel and passes underneath the primary clearance, after which coolant is redirected in a number of ways. The first direction is towards the chisel edge and the second is towards the workpiece wall. The work piece wall then directs coolant up the workpiece clearance as well as around the workpiece wall into the trailing cutting edge.

This behaviour is not very sensitive to the distance from the centre of the tool as small variations in coolant distribution have been observed across designs A and B. This mirrors the findings of Fallenstein & Aurich [Fallenstein and Aurich, 2014] who found that the distance of channel spacing from the central axis of the tool did not significantly effect the amount of heat removed from the tool by coolant. Consistency of flow features between cases A and C has shown in this study that an increase in channel diameter and mass flow rate do not appear to influence the global distribution of coolant significantly within the small range of cases that have been considered.

The analysis of case D, has shown that positioning the exit of the coolant channel in the primary clearance creates a significantly different flow behaviour. This observation is very significant because it demonstrates that coolant distribution can be modified to suit the machining application.

6.8 Further Validation

Validating the flow of coolant in the cutting zone is a particularly challenging task simply because it is very challenging to obtain any form of quantitative analysis of coolant flow during the cutting process. This however is one of the key motivations for using CFD as it enables detail analysis of an area which would otherwise remain unobservable. The validation for confined coolant flow in this thesis consists of two parts. Firstly this thesis will compare the experimental data from previous research against the numerical predictions. The second step of validation will compare the predicted flow behaviour of the CFD model against further experimental study carried out in this thesis.

6.8.1 Relevant Previous Research

In order to validate the behaviour of coolant predicted under the confined conditions of the cutting zone, the modelled coolant flow is compared against the experimental observations of Fallenstein and Aurich (2014). The numerical predictions of the velocity of coolant located under the primary cutting edge given in Figure 6.23(a) and the experimental measurements of velocity underneath the primary cutting

(a) Numerical Result   (b) Experimental
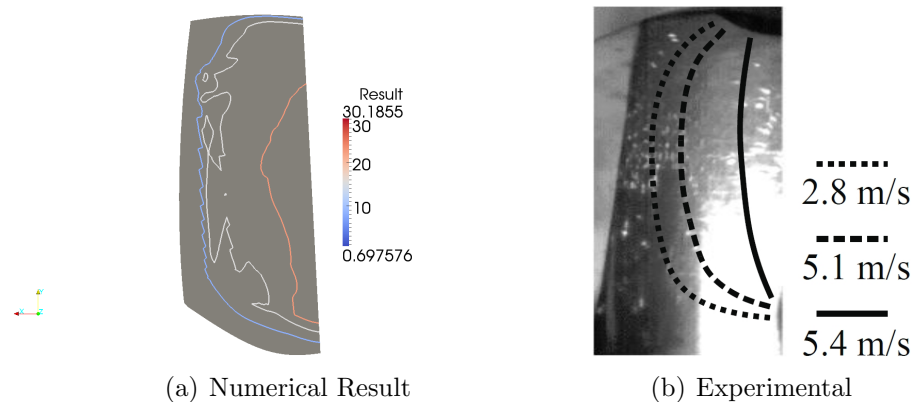
Figure 6.23: Velocity profile under the primary cutting edge. Experimental images provided by [Fallenstein and Aurich, 2014]

edge are displayed in Figure 6.23(b). The experimental work presents the velocity in the form of contour lines. These contours have been qualitatively compared to the numerical results produced by the model described in this chapter in Figure 6.23 (a). It can be seen that the model reproduces the flow structures observed in the experimental work. Although the magnitude of velocity is different between the cases, the flow structures predicted by the numerical model are still consistent with the observations of Fallenstein and Aurich, (2014).

6.8.2   Experimental Validation

As it is not possible to directly observe the behaviour of coolant located at the cutting zone under confined conditions an alternative experimental method was used for validating the predicted flow behaviour. This experimental validation used a sacrificial polymer coating on the tool, to observe geometry components supplied with coolant. The polymer used was a proprietary polymer made from Nitrocellulose and coloured to aid visual inspection. The experimental procedure is as follows:

First a hole (two times the tool diameter) was made in the workpiece using an uncoated tool. In order to create the confined space the tool did not break out the underside of the workpiece. The tool was then replaced with another tool coated in the polymer, however as it was not possible to position the tool directly in contact with the bottom of the cutting hole, the coated tool was positioned in the centre of the hole 0.5mm away from the bottom of the hole. Coolant was then supplied for 10 seconds before removing and visually inspecting the tool.

In order to prevent the coating being worn away by rubbing against the workpiece the tool remained stationary for these tests. As suggested by the analysis of the Rossby number in Section 2.5.2, Coriolis forces will not have a significant impact

on the delivery of coolant or this experiment. Results from the visual inspection

(a) Before (b) After
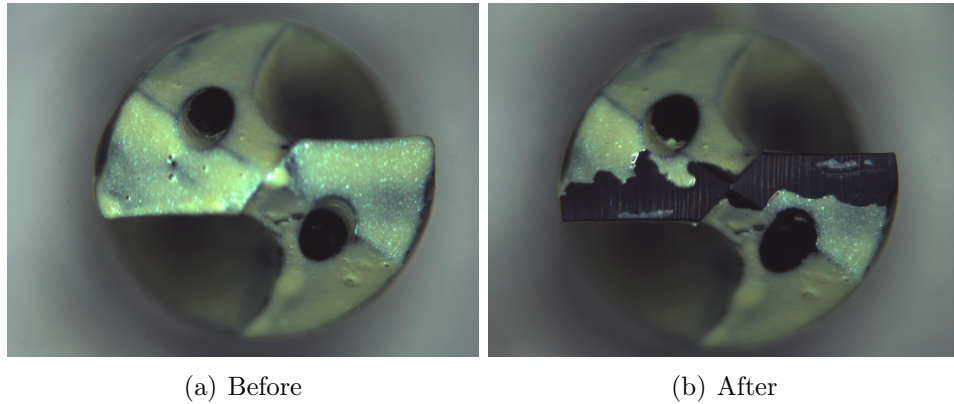
Figure 6.24: Images of polymer distribution before and after coolant supply.

are displayed in Figure 6.24. Figure 6.24(a) displays the cutting tool coated in the green polymer before the experiment was carried out, and Figure 6.24(b) shows the same tool geometry after the experiments. In these images areas which are coloured green indicate areas where the polymer has not been removed, however the dark areas show where the polymer has been removed by the action of the coolant. It can be seen in Figure 6.24(b) that some, but not all of the polymer coating, has been removed by the coolant. This strongly suggests that the polymer has only been removed in the areas where the flow is most violent, the primary clearance and the axial rake. This result is in qualitative agreement with the predictions of the wetting analysis and the flow feature analysis discussed earlier in this chapter, which predicted that coolant is directed by the primary clearance, axial rake and workpiece walls. This agreement validates the flow behaviour predicted by the numerical model.

6.9   Summary

This chapter has modelled 4 different coolant channel configurations, which are used to examine the change in coolant behaviour when the size, position and exit face

changes as well as a change in the mass flow rate of the system. The analysis for these cases has been decomposed into three main sections: volume of coolant analysis, wetted surface analysis and flow feature analysis.

The volume of coolant analysis calculated the amount of coolant contained in the cutting zone over time. This analysis found that no design fully flooded the fluid domain and each design reached a steady state at approximately 60-70% capacity. Ideally, the cutting zone would completely flood and a single phase model would be suitable, however the results from this analysis suggest that a multiphase model is most appropriate for the calculation of coolant exit flow.

The analysis of wetted area first studied the percentage of the tool face which is coated in coolant over time. This analysis has shown for cases A-C that approximately 67% of the tool surface area is wetted with coolant once the simulation reaches a steady state. For case D however the simulation does not reach a steady state for the time calculated and wets 60% of the tool surface area. This analysis however does not indicate which areas are supplied with coolant. In order to answer this question, this section included a visual analysis of the average volume fraction over the tool surface. This analysis found that each design heavily supplies coolant underneath the primary clearance and is also supplying large amounts of coolant to the axial rake and the inside corner of the cutting edge. In addition to this, calculations suggest that limited amount of coolant is supplied to the outer corner of the cutting edge for each design. This kind of analysis has not been performed previously and is therefore a significant contribution to this field.

Flow feature analysis in Section 6.7 observed the exit behaviour of coolant for cases A-D. This analysis identified a key flow feature which has been observed in all cases considered, which distributes coolant along the workpiece walls, up the drill clear-

ance and across the tool axial rake. This flow feature has not been found to be sensitive to a change in channel distance from the centre of the tool, mass flow rate, channel diameter or exit face. However the flow features observed in case D are significantly different even though displaying the same key flow feature previously mentioned.

As only a limited set of channel configurations have so far been analysed it would be unreasonable to draw conclusions encompassing all coolant channel configurations. However, this kind of analysis has not yet been performed in this field and while the analysis was unable to determine the exact cause of the change in flow behaviour due to the limited sample population, it demonstrates through the change in flow behaviour between channel configurations that there is a rich design space to be examined and further analysis using the present techniques is valuable to this field.

This chapter then closed with model validation, which was composed of two sections. The first section examined the experimental data of Fallenstein and Aurich (2014) and compared the velocity contour lines captured in their experimental study of cutting fluids. Although the operating velocities between the experiments and the problem considered are very different, the contour lines in the numerical results mirror the contour lines of Fallenstein and Aurich's experimental work. The second part of model validation was carried out using a sacrificial polymer to identify where coolant is being directed. These experiments coated a tool in a polymer which was then removed by the action of the coolant. This technique has been used to identify components of the tool which are supplied with coolant, the primary clearance and axial rake. These experiments have not been used in the application of twist drill machining and give a unique insight into coolant supply which has not been previously observed. Finally, these experimental results have been used to validate the numerical results contained within this chapter which are in qualitative agreement.

Chapter 7

Conclusions and Future Work

7.1 Conclusions

This thesis has been carried out in collaboration with Sandvik Coromant and presents research focused on analysing the application of coolant within twist-drill machining - a manufacturing process which is central to many industries such as electrical engineering and the manufacture of cars, railways, aircraft and ships.

Very little is known about the supply of coolant to the cutting zone during the drilling process because it is a particularly challenging problem to observe experimentally. For this reason the work contained in this thesis used numerical methods to calculate the delivery of coolant and gain insight into an otherwise unknown area. The implementation of the numerical method is constructed from two models: the internal, through-tool coolant flow model coupled with the coolant exit flow model.

7.1.1 Through-Tool Coolant Flow

The use of CFD for this analysis is particularly advantageous because it removes the need to manufacture and experimentally measure each channel configuration which

is costly in both time and materials. A numerical approach, following successful implementation and validation, allows the evaluation of any coolant channel configuration without the costly manufacturing and experimental processes.

The model described in Chapter 3 is responsible for modelling the through-tool delivery of coolant and employs a single phase formulation which assumes the coolant is incompressible, isothermal and isoviscous. The effects of rotation are accounted for by constructing the model in the rotating frame of reference of the tool, and the presence of turbulence is accounted for using the $k - \epsilon$ turbulence model. Pressure drop calculations for this model were validated against the friction factor correlation obtained by [Guo et al., 2001] and found calculations to be in reasonable agreement with experimental data. Furthermore, the single phase model also reproduced the effects of curvature and rotation described by [Hüttl and Friedrich, 2000, Hüttl and Friedrich, 2001] and [Yamamoto et al., 2000]. Following this, the model was used to perform a parametric study which identified the effects of each design parameter on the calculated pressure drop. The main conclusions of this study are as follows:

Effect of Length - Calculated pressure drop increases linearly with tool length.

Effect of Rotation - Found to have an insignificant influence on the calculated pressure drop. When changing speed of rotation from 0rpm to 10,000rpm the calculated pressure drop changes by less than 1%.

Effect of Pitch - The calculated pressure drop increases quadratically as pitch increases.

Effect of Spacing (Constant Helical Turn Spacing) - Calculated pressure drop increases linearly with channel spacing.

Effect of Spacing (Constant Helical Pitch Angle) - Calculated pressure drop decreases with channel spacing.

Helical flows have been the subject of a wealth of research, as shown in the Preliminary research. However this study examines rotating helical flows in the context of drill design, which operate at a large Reynolds and Dean numbers and large numbers of revolutions per minute and has not been examined previously in scientific literature. In addition to these conclusions, metamodelling techniques have also used in this analysis to give a global overview of the effect of tool design on calculated pressure drop calculations while simultaneously changing channel spacing and pitch. This method of analysis is particularly useful to aid the design of coolant channels as it has identified that designs which minimise pitch and maximise spacing are the most optimal designs. The final purpose of this model was used to inform the inlet conditions of the second model which models coolant exiting the twist-drill.

7.1.2   Coolant Exit Flow Modelling

The aim of this study was to gain a better understanding of the distribution of coolant located in the cutting zone to aid future tool designs. However, this is a particularly difficult problem to measure experimentally due to challenges arising from the confined space in the cutting zone combined with the large number of rotations per minute. This is complicated further by cuttings evacuating the cutting hole which prevent any obvious use of invasive experimental equipment because they may prevent chip evacuation and influence the flow of coolant or result in tool damage.

The problem of coolant exit flow was investigated numerically using a modified Vol-

ume of Fluid method outlined in Section 5.6 and is the first model of drill coolant flow to employ multiphase CFD techniques. However, due to the large computational requirements for numerical evaluations only 4 coolant channel configurations are considered in this thesis. The results for each of these numerical evaluations are analysed in Chapter 6 for domain flooding, wetted area and flow features.

Domain Flooding Analysis

Domain Flooding analysis is centred around examining how much of the fluid domain consists of coolant. The purpose of this study is to identify how much of the volume around the tool in the cutting zone is made up of air to identify any pockets of air in the domain. In an ideal situation the domain will become fully flooded, which suggests that coolant is only supplied to 60% of the tool cutting zone. However this study found designs A, B and C, which positioned coolant channel exits along the edge between the primary and tertiary clearance, to reach a steady state at 60% of the fluid domain filled with coolant.

Surface Wetting Analysis

The surface wetting analysis firstly calculated the percentage of the tool surface in contact with coolant. This analysis found that for designs A, B and C the surface would reach a steady state between 60% and 70% (depending on channel configuration), which suggests that up to approximately 40% of the tool is not supplied with coolant.

Further visual analysis was performed to identify tool components which are supplied with coolant and found that for all configurations the primary clearance and axial rake are well supplied with coolant, but the primary cutting edge is not very

well supplied with coolant. However, for cases A, B and C it is observed that coolant is directed up the tool flute by the axial rake. These results suggest there is much scope for design optimisation.

Flow Feature Analysis

This final portion of analysis examined coolant distribution across the entire fluid domain and identified key features which direct coolant within the cutting zone across all designs tested. These features showed following the exit of the tool and colliding with the bottom of the cutting hole, coolant is directed underneath the primary clearance. At this point coolant is directed in two main directions:

The first direction is towards the workpiece wall, which then directs the coolant either up the drill body clearance or into the trailing cutting edge. The second direction delivers coolant to the axial rake, which directs coolant across the cutting edge and for some designs up the flute of the tool. In addition to this it was found that coolant distribution for channels positioned along the edge between the primary and tertiary clearance are not very sensitive to the radial spacing, flow rate or size of the cross sectional area of the coolant channel.

The most significant finding is the substantial change in flow behaviour when positioning the coolant channel exit in the drill primary clearance. When located in the primary clearance, the flow comprised of many small droplets which were distributed throughout the entire domain. However, for the 3 designs which positioned the coolant channel exit along the edge between the primary and tertiary clearance the coolant is mostly distributed along the workpiece wall and shows an area in the centre of the domain which is not well supplied with coolant.

This analysis has given high resolution data on the flow of coolant contained within the cutting hole which could not be obtained through experimental methods or through a single phase formulation. This level of detail has led to the identification of key coolant distribution behaviours which have been found consistent across the four different channel configurations and have not been previously recorded in the scientific literature. Furthermore, this analysis has shown that the supply of coolant to the cutting zone can be changed significantly by changing the coolant channel positioning and that further research is required in this area and that there is great scope for design optimisation in this area.

7.2   Future Work

The application of coolant during the drilling process has only recently become subjected to systematic analysis using CFD and therefore there are many areas which this research could easily be extended towards. The suggestions contained in this section are not an exhaustive list and are mainly centred around the numerical modelling of coolant application in twist-drill machining. The tasks which are of the greatest priority to this field are as follows:

- The most urgent future work encompasses experimental measurement of coolant exit flow. These measurements are fundamental to gaining a better understanding of coolant exit flow as well as the accuracy of CFD modelling.

- Additional numerical evaluations of coolant exit flow from channels of circular cross-section in additional locations in the primary clearance are of particular interest to examine the effect of radial positioning of coolant channels which exit in the primary clearance of the tool.

- The multiphase model of coolant exit flow can also be applied to further study the influence of tool design features. For example, the effect of coolant dis-

tribution across the cutting edge in response to a change in chisel edge angle, axial rake angle or primary clearance angle. A significantly more detailed study of the effect of coolant channel position relative to each design feature of the tool and the influence on the coolant distribution will also be of significant industrial interest.

- The single phase through-tool flow analysis focuses on examining channels with circular cross section, but could be expanded upon to study different helical cross sections or within a shape optimisation study. This study would also be of significant interest to other industrial applications such as heat exchangers.

- The removal of heat from the tool from the application of coolant is the next logical feature to include in the present model to examine the removal of heat from the tool surface. This could be implemented in a number of ways, such as using a conjugate heat transfer model or secondly by a one-way formulation which does not model the solid domain and specifies a flux of energy into the fluid domain through the domain boundaries.

- The present model does not currently account for chip formation which can significantly influence the distribution of the flow of coolant within the cutting zone. The process of chip formation is a highly complex problem which is which is closely coupled with the distribution of coolant by the workpiece temperature [Kalhori, 2001].

The present study is an important step towards accurate calculation of coolant delivery during the cutting process. The application of single and multiphase models here has given an in-depth analysis of how coolant is transported to and distributed throughout the cutting zone. It does not, however, address some important phenomena such as heat transfer, phase compressibility, phase change and chip formation and evacuation. While these are not unknown fields and many researchers have

contributed towards them, significant further work is required to include them into the framework of the two-fluid model. It is the hope of the author that this study gives an increased level of insight into the delivery of coolant during the cutting process and provides a stepping stone towards a more accurate model for twist-drill coolant application modelling.

Bibliography

[Abele and Fujara, 2010] Abele, E. and Fujara, M. (2010). Simulation-based twist drill design and geometry optimization. *CIRP Annals-Manufacturing Technology*, 59(1):145–150.

[Alam et al., 2007] Alam, M., Ota, M., Ferdows, M., Islamv, M., Wahiduzzaman, M., and Yamamoto, K. (2007). Flow through a rotating helical pipe with a wide range of the dean number. *Archives of Mechanics*, 59(6):501–517.

[Ali et al., 2011] Ali, S., Dhar, N., and Dey, S. (2011). Effect of minimum quantity lubrication (mql) on cutting performance in turning medium carbon steel by uncoated carbide insert at different speed-feed combinations. *Advances in Production Engineering & Management*, 6(3).

[Arefi et al., 2005] Arefi, B., Settari, A., and Angman, P. (2005). Analysis and simulation of erosion in drilling tools. *Wear*, 259(1):263–270.

[Aris, 1990] Aris, R. (1990). *Vectors, tensors and the basic equations of fluid mechanics*. Courier Dover Publications.

[Ashgriz and Poo, 1991] Ashgriz, N. and Poo, J. (1991). Flair: Flux line-segment model for advection and interface reconstruction. *Journal of Computational Physics*, 93(2):449–468.

[Avila and Abrao, 2001] Avila, R. and Abrao, A. (2001). The effect of cutting fluids on the machining of hardened aisi 4340 steel. *Journal of Materials Processing Technology*, 119(1):21–26.

[Bates et al., 2004] Bates, S. J., Sienz, J., and Toropov, V. V. (2004). Formulation of the optimal latin hypercube design of experiments using a permutation genetic algorithm. *AIAA*, 2011:1–7.

[Benhamadouche and Laurence, 2003] Benhamadouche, S. and Laurence, D. (2003). Les, coarse les, and transient rans comparisons on the flow across a tube bundle. *International Journal of Heat and Fluid Flow*, 24(4):470–479.

[Berberović et al., 2009] Berberović, E., van Hinsberg, N. P., Jakirlić, S., Roisman, I. V., and Tropea, C. (2009). Drop impact onto a liquid layer of finite thickness: Dynamics of the cavity evolution. *Physical Review E*, 79(3):036306.

[Bergles et al., 1981] Bergles, A. E., Collier, J. G., Delhaye, J.-M., Hewitt, G. F., and Mayinger, F. (1981). *Two-phase flow and heat transfer in the power and process industries*. Hemisphere publishing corporation Washington.

[Birkhoff and Zarantonello, 1987] Birkhoff, G. and Zarantonello, E. (1987). Jets, wakes, and cavities.

[Bono and Ni, 2001] Bono, M. and Ni, J. (2001). The effects of thermal distortions on the diameter and cylindricity of dry drilled holes. *International Journal of Machine Tools and Manufacture*, 41(15):2261–2270.

[Bono and Ni, 2002] Bono, M. and Ni, J. (2002). A method for measuring the temperature distribution along the cutting edges of a drill. *Journal of Manufacturing Science and Engineering*, 124(4):921–923.

[Bono and Ni, 2006] Bono, M. and Ni, J. (2006). The location of the maximum temperature on the cutting edges of a drill. *International Journal of Machine Tools and Manufacture*, 46(7):901–907.

[Box and Wilson, 1951] Box, G. E. and Wilson, K. (1951). On the experimental attainment of optimum conditions. *Journal of the Royal Statistical Society. Series B (Methodological)*, 13(1):1–45.

[Brackbill et al., 1992] Brackbill, J., Kothe, D. B., and Zemach, C. (1992). A continuum method for modeling surface tension. *Journal of computational physics*, 100(2):335–354.

[Braga et al., 2002] Braga, D. U., Diniz, A. E., Miranda, G., and Coppini, N. (2002). Using a minimum quantity of lubricant (mql) and a diamond coated tool in the drilling of aluminum–silicon alloys. *Journal of Materials Processing Technology*, 122(1):127–138.

[Brennen, 2005] Brennen, C. E. (2005). *Fundamentals of multiphase flow*. Cambridge University Press.

[Cavazzuti, 2013] Cavazzuti, M. (2013). General guidelines: How to proceed in an optimization exercise. In *Optimization Methods*, pages 147–152. Springer Berlin Heidelberg.

[Chen and Zhang, 2003] Chen, H. and Zhang, B. (2003). Fluid flow and mixed convection heat transfer in a rotating curved pipe. *International journal of thermal sciences*, 42(11):1047–1059.

[Chowdhury et al., 2014] Chowdhury, S., Islam, M., and Boswell, B. (2014). Effectiveness of using cfd for comparing tool cooling methods. In *Proceedings of the World Congress on Engineering*, volume 2.

[Cimbala and Çengel, 2008] Cimbala, J. M. and Çengel, Y. A. (2008). *Essentials of fluid mechanics: fundamentals and applications*. McGraw-Hill Higher Education.

[Coromant, 2013] Coromant, S. (2013). Coolant knowledge base. `http://www.sandvik.coromant.com`.

[Costa et al., 2009] Costa, E. S., Silva, M. B. d., and Machado, A. R. (2009). Burr produced on the drilling process as a function of tool wear and lubricant-coolant conditions. *Journal of the Brazilian Society of Mechanical Sciences and Engineering*, 31:57 – 63.

[Crowe, 2005] Crowe, C. T. (2005). *Multiphase flow handbook*. CRC Press.

[Crowe et al., 2011] Crowe, C. T., Schwarzkopf, J. D., Sommerfeld, M., and Tsuji, Y. (2011). *Multiphase flows with droplets and particles*. CRC press.

[Dean, 1927] Dean, W. (1927). Note on the motion of fluid in a curved pipe. *The London, Edinburgh, and Dublin Philosophical Magazine and Journal of Science*, 4(20):208–223.

[Deshpande et al., 2012] Deshpande, S. S., Anumolu, L., and Trujillo, M. F. (2012). Evaluating the performance of the two-phase flow solver interfoam. *Computational Science & Discovery*, 5(1):014016.

[DeVries et al., 1968] DeVries, M., Saxena, U., and Wu, S. (1968). Temperature distributions in drilling. *Journal of Manufacturing Science and Engineering*, 90(2):231–238.

[Dhar et al., 2006] Dhar, N., Kamruzzaman, M., and Ahmed, M. (2006). Effect of minimum quantity lubrication (mql) on tool wear and surface roughness in turning aisi-4340 steel. *Journal of materials processing technology*, 172(2):299–304.

[Dörr and Sahm, 2000] Dörr, J. and Sahm, A. (2000). A mínima quantidade de lubrificante avaliada pelos usuários. *Máquinas e Metais*, 418:20–39.

[Duan et al., 2003] Duan, R.-Q., Koshizuka, S., and Oka, Y. (2003). Two-dimensional simulation of drop deformation and breakup at around the critical weber number. *Nuclear Engineering and Design*, 225(1):37 – 48.

[Elghobashi, 1994] Elghobashi, S. (1994). On predicting particle-laden turbulent flows. *Applied Scientific Research*, 52(4):309–329.

[Eustice, 1910] Eustice, J. (1910). Flow of water in curved pipes. *Proceedings of the Royal Society of London. Series A, Containing Papers of a Mathematical and Physical Character*, 84(568):pp. 107–118.

[Eustice, 1911] Eustice, J. (1911). Experiments on stream-line motion in curved pipes. *Proceedings of the Royal Society of London. Series A*, 85(576):119–131.

[Fallenstein and Aurich, 2014] Fallenstein, F. and Aurich, J. (2014). Cfd based investigation on internal cooling of twist drills. *Procedia CIRP*, 14(0):293 – 298. 6th CIRP International Conference on High Performance Cutting, HPC2014.

[Favre, 1965] Favre, A. (1965). Equations des gaz turbulents compressibles. *Journal de mecanique*, 4(4):391.

[Ferziger and Perić, 2002] Ferziger, J. H. and Perić, M. (2002). *Computational methods for fluid dynamics*, volume 3. Springer Berlin.

[Forrester et al., 2008] Forrester, A., Sobester, A., and Keane, A. (2008). *Engineering design via surrogate modelling: a practical guide*. John Wiley & Sons.

[Fuh et al., 1994] Fuh, K.-H., Chen, W.-C., and Liang, P.-W. (1994). Temperature rise in twist drills with a finite element approach. *International communications in heat and mass transfer*, 21(3):345–358.

[Gammack and Hydon, 2001] Gammack, D. and Hydon, P. E. (2001). Flow in pipes with non-uniform curvature and torsion. *Journal of Fluid Mechanics*, 433(1):357–382.

[Germano, 1982] Germano, M. (1982). On the effect of torsion on a helical pipe flow. *Journal of Fluid Mechanics*, 125(1):1–8.

[Gosman et al., 1983] Gosman, A., Ideriah, F., and Arnal, M. P. (1983). *TEACH-2E, a General Computer Program for Two-dimensional, Turbulent, Recirculating Flows*. Department of Mechanical Engineering, Imperial College.

[Guo et al., 2001] Guo, L., Feng, Z., and Chen, X. (2001). An experimental investigation of the frictional pressure drop of steam–water two-phase flow in helical coils. *International journal of heat and mass transfer*, 44(14):2601–2610.

[Haan et al., 1997] Haan, D., Batzer, S., Olson, W., and Sutherland, J. (1997). An experimental study of cutting fluid effects in drilling. *Journal of Materials Processing Technology*, 71(2):305–313.

[Hänle and Schwenck, 2005] Hänle, P. and Schwenck, M. (2005). Optimization of cutting tools using ca-technologies. In *8th CIRP International Workshop on Modeling of Machining Operations*, pages 463–468.

[Hestroni, 1982] Hestroni, G. (1982). *Handbook of multiphase systems*. McGraw-Hill.

[Hill, 1998] Hill, D. P. (1998). *The computer simulation of dispersed two-phase flow*. PhD thesis, University of London.

[Hinze, 1959] Hinze, J. (1959). Turbulence, 1975. *New York*.

[Hirsch, 2007] Hirsch, C. (2007). *Numerical computation of internal and external flows: the fundamentals of computational fluid dynamics*, volume 1. Butterworth-Heinemann.

[Hirt and Nichols, 1981] Hirt, C. W. and Nichols, B. D. (1981). Volume of fluid (vof) method for the dynamics of free boundaries. *Journal of computational physics*, 39(1):201–225.

[Hirt and Kopp, 2009] Hirt, G. and Kopp, R. (2009). *Thixoforming.* John Wiley & Sons.

[Hüttl and Friedrich, 2000] Hüttl, T. and Friedrich, R. (2000). Influence of curvature and torsion on turbulent flow in helically coiled pipes. *International Journal of Heat and Fluid Flow*, 21(3):345–353.

[Hüttl and Friedrich, 2001] Hüttl, T. and Friedrich, R. (2001). Direct numerical simulation of turbulent flows in curved and helically coiled pipes. *Computers & fluids*, 30(5):591–605.

[Ishigaki, 1996] Ishigaki, H. (1996). Laminar flow in rotating curved pipes. *Journal of Fluid Mechanics*, 329:373–388.

[Ishii, 1975] Ishii, M. (1975). Thermo-fluid dynamic theory of two-phase flow. *NASA STI/Recon Technical Report A*, 75:29657.

[Issa, 1986] Issa, R. I. (1986). Solution of the implicitly discretised fluid flow equations by operator-splitting. *Journal of computational physics*, 62(1):40–65.

[Ito, 1959] Ito, H. (1959). Frictional factors for turbulent flow in curved pipes. *Journal of Engineering*, 81:123–134.

[Ito, 1969] Ito, H. (1969). Laminar flow in curved pipes. *ZAMM-Journal of Applied Mathematics and Mechanics/Zeitschrift für Angewandte Mathematik und Mechanik*, 49(11):653–663.

[Jasak, 1996] Jasak, H. (1996). *Error analysis and estimation for the finite volume method with applications to fluid flows.* PhD thesis, Imperial College London (University of London).

[Jen et al., 2002] Jen, T., Gutierrez, G., Eapen, S., Barber, G., Zhao, H., Szuba, P., Labataille, J., and Manjunathaiah, J. (2002). Investigation of heat pipe cooling

in drilling applications.: part i: preliminary numerical analysis and verification. *International Journal of Machine Tools and Manufacture*, 42(5):643 – 652.

[Johns et al., 2014] Johns, A., Thompson, H., Summers, J., Hewson, R., and Merson, E. (2014). Internal twist drill coolant channel modelling using computational fluid dynamics. In *ECCOMAS 2014-WCCM XI*.

[Jonas Bolinder and Sunden, 1995] Jonas Bolinder, C. and Sunden, B. (1995). Flow visualization and ldv measurements of laminar flow in a helical square duct with finite pitch. *Experimental thermal and fluid science*, 11(4):348–363.

[Kalhori, 2001] Kalhori, V. (2001). *Modelling and simulation of mechanical cutting.* PhD thesis, Luleå University of Technology.

[Kim et al., 2009] Kim, B.-S., Lee, Y.-B., and Choi, D.-H. (2009). Comparison study on the accuracy of metamodeling technique for non-convex functions. *Journal of Mechanical Science and Technology*, 23(4):1175–1181.

[Kralj, 1996] Kralj, C. (1996). *Numerical simulation of Diesel spray processes.* PhD thesis, University of London.

[Landahl and Mollo-Christensen, 1992] Landahl, M. T. and Mollo-Christensen, E. (1992). *Turbulence and random processes in fluid mechanics.* Cambridge University Press.

[Landau and Lifshits, 1975] Landau, L. D. and Lifshits, E. M. (1975). *The classical theory of fields*, volume 2. Butterworth-Heinemann.

[Launder et al., 1975] Launder, B., Reece, G. J., and Rodi, W. (1975). Progress in the development of a reynolds-stress turbulence closure. *Journal of fluid mechanics*, 68(03):537–566.

[Launder and Spalding, 1974] Launder, B. E. and Spalding, D. (1974). The numerical computation of turbulent flows. *Computer methods in applied mechanics and engineering*, 3(2):269–289.

[Li and Shih, 2007] Li, R. and Shih, A. (2007). Tool temperature in titanium drilling. *Ann Arbor*, 1001:48109–2125.

[Loewen and Shaw, 1954] Loewen, E. and Shaw, M. (1954). On the analysis of cutting tool temperatures. *Trans. ASME*, 76(2):217–225.

[Loweth et al., 2010] Loweth, E., De Boer, G., and Toropov, V. (2010). Practical recommendations on the use of moving least squares metamodel building. In *Proceedings of the 13th International Conference on Civil, Structural and Environmental Engineering Computing, 96, Civil-Comp Press, Stirlingshire*.

[Machado and Diniz, 2000] Machado, A. and Diniz, A. (2000). Corte a seco, com mínima quantidade de fluido e com fluido em abundância: usos, aplicações, vantagens e desvantagens. In *Congresso Usinagem*.

[McConalogue and Srivastava, 1968] McConalogue, D. and Srivastava, R. (1968). Motion of a fluid in a curved tube. *Proceedings of the Royal Society of London. Series A. Mathematical and Physical Sciences*, 307(1488):37–53.

[Menter, 1992] Menter, F. R. (1992). Performance of popular turbulence model for attached and separated adverse pressure gradient flows. *AIAA journal*, 30(8):2066–2072.

[Menter, 1994] Menter, F. R. (1994). Two-equation eddy-viscosity turbulence models for engineering applications. *AIAA journal*, 32(8):1598–1605.

[Mitsubishi, 2013] Mitsubishi (2013). Drill features and specification. `http://www.mitsubishicarbide.net/`.

[Montgomery, 2008] Montgomery, D. C. (2008). *Design and analysis of experiments.* John Wiley & Sons.

[Murata and Miyake, 1981] Murata, S. and Miyake, Y. (1981). lnaba, t., and ogawa, h. 1981. laminar flow in a helically coiled pipe. *Bull. Jpn. Soc. ME*, 24:355–362.

[Muzaferija, 1994] Muzaferija, S. (1994). *Adaptive finite volume method for flow prediction using unstructured meshes and multigrid approach.* PhD thesis, University of London UK.

[Naphon and Wongwises, 2006] Naphon, P. and Wongwises, S. (2006). A review of flow and heat transfer characteristics in curved tubes. *Renewable and Sustainable Energy Reviews*, 10(5):463–490.

[Nilsson, 2014] Nilsson, H. (2014). Turbomachinery training at ofw9.

[Ono and Kondo, 1960] Ono, S. and Kondo, S. (1960). Molecular theory of surface tension in liquids. In *Structure of Liquids/Struktur der Flüssigkeiten*, pages 134–280. Springer.

[OpenCFD, 2013] OpenCFD (2013). Openfoam.

[Patankar et al., 1974] Patankar, S., Pratap, V., and Spalding, D. (1974). Prediction of laminar flow and heat transfer in helically coiled pipes. *Journal of Fluid Mechanics*, 62(03):539–551.

[Patankar and Spalding, 1972] Patankar, S. and Spalding, D. (1972). A calculation procedure for heat, mass and momentum transfer in three-dimensional parabolic flows. *International Journal of Heat and Mass Transfer*, 15(10):1787 – 1806.

[Patankar et al., 1975] Patankar, S. V., Pratap, V., and Spalding, D. (1975). Prediction of turbulent flow in curved pipes. *Journal of Fluid Mechanics*, 67(3):583–595.

[Peric, 1985] Peric, M. (1985). *A finite volume method for the prediction of three-dimensional fluid flow in complex ducts.* PhD thesis, Imperial College London (University of London).

[Pope, 2000] Pope, S. B. (2000). *Turbulent flows.* Cambridge university press.

[Raach et al., 2011] Raach, H., Somasundaram, S., and Mitrovic, J. (2011). Optimisation of turbulence wire spacing in falling films performed with openfoam. *Desalination*, 267(1):118–119.

[Rider and Kothe, 1995] Rider, W. J. and Kothe, D. B. (1995). Stretching and tearing interface tracking methods. *AIAA paper*, 95:17.

[Rudman, 1997] Rudman, M. (1997). Volume-tracking methods for interfacial flow calculations. *International journal for numerical methods in fluids*, 24(7):671–691.

[Rusche, 2003] Rusche, H. (2003). *Computational fluid dynamics of dispersed two-phase flows at high phase fractions.* PhD thesis, Imperial College London (University of London).

[Schlichting and Gersten, 2000] Schlichting, H. and Gersten, K. (2000). *Boundary-layer theory.* Springer.

[Shaw, 2005] Shaw, M. (2005). *Metal cutting principles*, volume 19. Oxford University Press Oxford.

[Shih et al., 1995] Shih, T.-H., Liou, W. W., Shabbir, A., Yang, Z., and Zhu, J. (1995). A new k- eddy viscosity model for high reynolds number turbulent flows. *Computers & Fluids*, 24(3):227–238.

[Spalart, 2000] Spalart, P. (2000). Strategies for turbulence modelling and simulations. *International Journal of Heat and Fluid Flow*, 21(3):252–263.

[Srinivas et al., 1968] Srinivas, P., Nandapur, S., and Holland, F. (1968). Pressure drop and heat transfer in coils. *Transactions of the Institution of Chemical Engineers and the Chemical Engineer*, 46(4):C113.

[Srinivasan et al., 1968] Srinivasan, P., Nandapurkar, S., and Holland, F. (1968). Pressure drop and heat transfer in coils. *Chem. Eng*, 218:113–119.

[Srinivasan et al., 2011] Srinivasan, V., Salazar, A. J., and Saito, K. (2011). Modeling the disintegration of modulated liquid jets using volume-of-fluid (vof) methodology. *Applied Mathematical Modelling*, 35(8):3710–3730.

[Stephenson et al., 1997] Stephenson, D., Jen, T.-C., and Lavine, A. (1997). Cutting tool temperatures in contour turning: transient analysis and experimental verification. *Journal of manufacturing science and engineering*, 119(4A):494–501.

[Sussman et al., 1994] Sussman, M., Smereka, P., and Osher, S. (1994). A level set approach for computing solutions to incompressible two-phase flow. *Journal of Computational physics*, 114(1):146–159.

[Taherkhani, 2014] Taherkhani, A. R. (2014). *Computational Fluid Dynamics Based Optimization of Emergency Response Vehicles*. PhD thesis, University of Leeds, School of Mechanical Engineering.

[Taylor, 1929] Taylor, G. I. (1929). The criterion for turbulence in curved pipes. *Proceedings of the Royal Society of London. Series A, Containing Papers of a Mathematical and Physical Character*, 124(794):pp. 243–249.

[Tennekes and Lumley, 1972] Tennekes, H. and Lumley, J. L. (1972). *A first course in turbulence*. MIT press.

[Treurnicht et al., 2010] Treurnicht, N., Joubert, H., Oosthuizen, G., and Akdogan, G. (2010). Investigating of eco-and energy-efficient lubrication strategies for the

drilling of light metal alloys: general article. *South African Journal of Industrial Engineering*, 21(2):25–38.

[Truesdell and Adler, 1970] Truesdell, L. and Adler, R. (1970). Numerical treatment of fully developed laminar flow in helically coiled tubes. *AIChE Journal*, 16(6):1010–1015.

[Tulin, 1964] Tulin, M. P. (1964). Supercavitating propellers history, operating characteristics, mechanism of operation. Technical report, DTIC Document.

[Ubbink, 1997] Ubbink, O. (1997). *Numerical prediction of two fluid systems with sharp interfaces.* PhD thesis, University of London UK.

[Ujhidy et al., 2003] Ujhidy, A., Nmeth, J., and Szpvlgyi, J. (2003). Fluid flow in tubes with helical elements. *Chemical Engineering and Processing: Process Intensification*, 42(1):1 – 7.

[Van Dyke, 1982] Van Dyke, M. (1982). An album of fluid motion.

[Vaz Jr et al., 2007] Vaz Jr, M., Owen, D., Kalhori, V., Lundblad, M., and Lindgren, L.-E. (2007). Modelling and simulation of machining processes. *Archives of computational methods in engineering*, 14(2):173–204.

[Versteeg and Malalasekera, 2007] Versteeg, H. K. and Malalasekera, W. (2007). *An introduction to computational fluid dynamics: the finite volume method.* Pearson Education.

[Wang, 1981] Wang, C. (1981). On the low-reynolds-number flow in a helical pipe. *Journal of Fluid Mechanics*, 108:185–94.

[Watanabe et al., 1977] Watanabe, K., Yokoyama, K., and Ichimiya, R. (1977). Thermal analyses of the drilling process. *Bull. Jpn. Soc. Precis. Eng.*, 11(2):71–77.

[Weinert and Loichinger, 2001] Weinert, K. and Loichinger, A. (2001). Strömungstechnische optimierung von bohrwerkzeugen. *VDI-Z*, 143(AOU):58–61.

[Weller et al., 1998] Weller, H. G., Tabor, G., Jasak, H., and Fureby, C. (1998). A tensorial approach to computational continuum mechanics using object-oriented techniques. *Computers in physics*, 12(6):620–631.

[Wilcox, 1988] Wilcox, D. C. (1988). Reassessment of the scale-determining equation for advanced turbulence models. *AIAA journal*, 26(11):1299–1310.

[Wu and Di Han, 2009] Wu, J. and Di Han, R. (2009). A new approach to predicting the maximum temperature in dry drilling based on a finite element model. *Journal of Manufacturing Processes*, 11(1):19–30.

[Yakhot et al., 1992] Yakhot, V., Orszag, S., Thangam, S., Gatski, T., and Speziale, C. (1992). Development of turbulence models for shear flows by a double expansion technique. *Physics of Fluids A: Fluid Dynamics (1989-1993)*, 4(7):1510–1520.

[Yakhot and Smith, 1992] Yakhot, V. and Smith, L. M. (1992). The renormalization group, the -expansion and derivation of turbulence models. *Journal of Scientific Computing*, 7(1):35–61.

[Yamamoto et al., 1995] Yamamoto, K., Akita, T., Ikeuchi, H., and Kita, Y. (1995). Experimental study of the flow in a helical circular tube. *Fluid Dynamics Research*, 16(4):237–249.

[Yamamoto et al., 2000] Yamamoto, K., Alam, M., Yasuhara, J., and Aribowo, A. (2000). Flow through a rotating helical pipe with circular cross-section. *International Journal of Heat and Fluid Flow*, 21(2):213 – 220.

[Yamamoto et al., 2002] Yamamoto, K., Aribowo, A., Hayamizu, Y., Hirose, T., and Kawahara, K. (2002). Visualization of the flow in a helical pipe. *Fluid Dynamics Research*, 30(4):251–267.

[Yamamoto et al., 1998] Yamamoto, K., Yanase, S., and Jiang, R. (1998). Stability of the flow in a helical tube. *Fluid Dynamics Research*, 22(3):153 – 170.

[Yamamoto et al., 1994] Yamamoto, K., Yanase, S., and Yoshida, T. (1994). Torsion effect on the flow in a helical pipe. *Fluid Dynamics Research*, 14(5):259 – 273.

[Zhang and Zhang, 2003] Zhang, J. and Zhang, B. (2003). Dean equations extended to a rotating helical pipe flow. *Journal of engineering mechanics*, 129(7):823–829.

[Zhang et al., 2008] Zhang, P., Churi, N., Pei, Z. J., and Treadwell, C. (2008). Mechanical drilling processes for titanium alloys: a literature review. *Machining Science and Technology*, 12(4):417–444.